



NTNU – Trondheim
Norwegian University of
Science and Technology

Numerical modeling of turbulence above helidecks

Fredrik Mentzoni

Master of Science in Mechanical Engineering

Submission date: June 2014

Supervisor: Ivar Ståle Ertesvåg, EPT

Co-supervisor: Kjell Erik Rian, ComputIT
Rune N. Kleiveland, ComputIT

Norwegian University of Science and Technology
Department of Energy and Process Engineering

EPT-M-2014-70

MASTEROPPGÅVE

for

Student Fredrik Mentzoni

Våren 2014

Numerisk modellering av turbulens over helikopterdekk

*Numerical modeling of turbulence above helicopter decks***Bakgrunn og føremål**

For å sikre tryggleiken for helikoptertransport til og frå olje-/gass-installasjonar er det innført standardar som regulerer tilhøve som tillet flyging. Det har kome ein ny Norsok standard C-004 om helikopterdekk (2. utg. 2013), som stiller strengare krav til kor mykje turbulens ein kan tillate over helikopterdekk. Standarden stiller krav til kunnskapen, som gjer at vindfeltet må simulerast med numeriske verkty og avanserte modellar.

Føremålet med oppgåva er å finne ut kor nøyaktige modellar ein må bruke for å tilfredstille krava i Norsok-standard. Oppgåva er i samarbeid med Computit AS i Trondheim.

I oppgåva skal studenten

- Setje seg inn i dei krava Norsok standard C-004 set opp for turbulens og vind.
- Gjere seg godt kjend med den aktuelle litteraturen om turbulensmodellering og simulering.
- Saman med rettleiarane finne fram til og gjere seg kjend med eigna simuleringsverkty.
- Velje modellar som kan vere eigna til operasjonelle undersøkingar og modellar til meir nøyaktige samanlikningar. Dersom det ikkje er gjort og dokumentert frå før, må modellane, slik dei er lagde inn i programmet, verifiserast mot måledata.
- Definere aktuelle tilfelle med vind over helikopterdekk og undersøkje kor gode resultat dei ulike modellane gjev i høve til krava i standarden.
- Drøfte resultatata.

Senest 14 dager etter utlevering av oppgaven skal kandidaten levere/sende instituttet en detaljert fremdrift- og eventuelt forsøksplan for oppgaven til evaluering og eventuelt diskusjon med faglig ansvarlig/veiledere. Detaljer ved eventuell utførelse av dataprogrammer skal avtales nærmere i samråd med faglig ansvarlig.

Besvarelsen redigeres mest mulig som en forskningsrapport med et sammendrag både på norsk og engelsk, konklusjon, litteraturliste, innholdsfortegnelse etc. Ved utarbeidelsen av teksten skal kandidaten legge vekt på å gjøre teksten oversiktlig og velskrevet. Med henblikk på lesning av besvarelsen er det viktig at de nødvendige henvisninger for korresponderende steder i tekst, tabeller og figurer anføres på begge steder. Ved bedømmelsen legges det stor vekt på at resultatene er grundig bearbeidet, at de oppstilles tabellarisk og/eller grafisk på en oversiktlig måte, og at de er diskutert utførlig.

Alle benyttede kilder, også muntlige opplysninger, skal oppgis på fullstendig måte. For tidsskrifter og bøker oppgis forfatter, tittel, årgang, sidetall og eventuelt figurnummer.

Det forutsettes at kandidaten tar initiativ til og holder nødvendig kontakt med faglærer og veileder(e). Kandidaten skal rette seg etter de reglementer og retningslinjer som gjelder ved alle (andre) fagmiljøer som kandidaten har kontakt med gjennom sin utførelse av oppgaven, samt etter eventuelle pålegg fra Institutt for energi- og prosesssteknikk.

Risikovurdering av kandidatens arbeid skal gjennomføres i henhold til instituttets prosedyrer. Risikovurderingen skal dokumenteres og inngå som del av besvarelsen. Hendelser relatert til kandidatens arbeid med uheldig innvirkning på helse, miljø eller sikkerhet, skal dokumenteres og inngå som en del av besvarelsen. Hvis dokumentasjonen på risikovurderingen utgjør veldig mange sider, leveres den fulle versjonen elektronisk til veileder og et utdrag inkluderes i besvarelsen.

I henhold til "Utfyllende regler til studieforskriften for teknologistudiet/sivilingeniørstudiet" ved NTNU § 20, forbeholder instituttet seg retten til å benytte alle resultater og data til undervisnings- og forskningsformål, samt til fremtidige publikasjoner.


Besvarelsen leveres digitalt i DAIM. Et faglig sammendrag med oppgavens tittel, kandidatens navn, veileders navn, årstall, institutt navn, og NTNUs logo og navn, leveres til instituttet som en separat pdf-fil. Etter avtale leveres besvarelse og evt. annet materiale til veileder i digitalt format.

- Arbeid i laboratorium (vannkraftlaboratoriet, strømningsteknisk, varmeteknisk)
- Feltarbeid

NTNU, Institutt for energi- og prosesssteknikk, 14. januar 2014



Olav Bolland
Instituttleder



Ivar S. Ertesvåg
Faglig ansvarleg/rettleiar

Medrettleiarar:
Dr. Kjell Erik Rian, Computit AS
Dr. Rune N. Kleiveland, Computit AS

Abstract

New regulations in the second edition of NORSOK Standard C-004, released in May 2013, require the use of a Reynolds stress transport model for numerical simulations of turbulence above helidecks on the Norwegian continental shelf. To ensure safe flying conditions, maximum bounds are given on the standard deviation of the vertical velocity component above the helideck. Two Reynolds stress transport models, as well as simpler models based on the turbulence energy, are compared in numerical simulations of structure induced turbulence on a simplified offshore rig with a helideck, using the computational fluid dynamics package STAR-CCM+. In addition to helideck simulations, three test cases are simulated for validation and verification with experimental measurements, DNS, and simulations by others.

The Reynolds stress transport models do not outperform the turbulence energy transport models in the validation and verification simulations. The vertical Reynolds stress component is typically underestimated compared to experimental measurements, while the turbulence energy transport models typically overestimate the vertical Reynolds stress component. The same tendencies are found in the helideck simulations, the predicted magnitude of the vertical Reynolds stress component is smaller with the Reynolds stress transport models.

The turbulence criteria in NORSOK Standard C-004 could have been based on the turbulence energy instead of the standard deviation of the vertical velocity component. The turbulence energy is half the sum of the velocity variances, hence it includes turbulence in all directions. Calculations of the turbulence energy are less sensitive to the modeling of redistribution in Reynolds stress transport models and the constitutive relation in turbulence energy transport models. Using turbulence energy to assess structure induced turbulence above offshore helidecks, may therefore reduce differences between different turbulence models, thus increase confidence in simulation results.

Sammendrag

Den andre utgaven av NORSOK Standard C-004, utgitt i mai 2013, krever bruk av en reynoldsspenningstransportmodell ved numeriske simuleringer av turbulens over helikopterdekk på norsk kontinentalsokkel. For å sikre forsvarlige flyforhold er det gitt krav til maksimalt tillatt standardavvik av vertikalhastighetskomponenten over helikopterdekket. To reynoldsspenningstransportmodeller, i tillegg til enklere modeller basert på turbulensenergi, er sammenlignet i numeriske simuleringer av strukturindusert turbulens på en forenklet offshorerigg, med det numeriske strømningsverktøyet STAR-CCM+. I tillegg til helikopterdekkssimuleringene, er tre testcase simulert for å validere og verifisere modellene med eksperimentaldata, DNS og simuleringer gjort av andre.

Reynoldsspenningstransportmodellene gir ikke betydelige bedre resultat enn turbulensenergitransportmodeller i validerings- og verifiseringssimuleringene. Den vertikale reynoldsspenningskomponenten er typisk beregnet mindre enn hva eksperimentaldatene tilsier. Turbulensenergitransportmodellene beregner typisk for stor vertikalkomponent. De samme tendensene er synlige i helikopterdekkssimuleringene, reynoldsspenningstransportmodellene beregner mindre standardavvik av vertikalhastighetskomponenten.

Turbulenskriteriene i NORSOK Standard C-004 kunne vært basert på turbulensenergi i stedet for standardavviket av vertikalhastighetskomponenten. Turbulensenergi er halve summen av hastighetsvariansene og inkluderer derfor turbulens i alle retninger. Beregning av turbulensenergi er mindre sensitiv til modellering av omfordelingsleddet i reynoldsspenningstransportmodeller og spennings-tøyingsrelasjonen i turbulensenergitransportmodeller. Bruk av turbulensenergi for evaluering av strukturindusert turbulens over offshore helikopterdekk kan derfor redusere forskjellene mellom ulike turbulensmodeller, noe som vil øke tilliten til simuleringresultatene.


Preface

The topic of this thesis was determined by the Department of Energy and Process Engineering, at the Norwegian University of Science and Technology, in cooperation with Computational Industry Technologies AS.

I will always be grateful to Trond Evanger and Bjørn F. Magnussen for giving me the opportunity to learn from the best. For teaching me how to deal with STAR-CCM+, thank you Tim Mak and Ivar Jarle Øye. Most of all, I thank my supervisors, Ivar Ståle Ertesvåg, Rune N. Kleiveland, and Kjell Erik Rian, for leading me through the land and helping me understand the best I can. Your advice and dedication have been much appreciated.

Any fool knows a dog needs a home. So when I come home cold and tired, thank you Ina and Anna Maria, for the warmth beside the fire. And if the dam breaks open many years too soon, I see you, Odd-Arne, on the dark side of the moon.

Trondheim, June 2014



Fredrik Mentzoni

Contents

Abstract	v
Sammendrag	vii
Preface	ix
Table of contents	xi
Nomenclature	xiii
1 Introduction	1
2 Helideck requirements	3
2.1 NORSOK Standard C-004	3
2.2 Background	4
2.3 Proposed turbulence energy criteria	7
3 Turbulent flows	11
3.1 Governing equations	11
3.2 Reynolds decomposition and averaging	12
3.3 Transport equations for turbulence quantities	13
4 Turbulence models	17
4.1 Reynolds stress transport models	18
4.2 Linear pressure-strain (LPS)	20
4.3 Quadratic pressure-strain (QPS)	21
4.4 Turbulence energy transport models	22
4.5 Standard k - ε (SKE)	23
4.6 Realizable k - ε (RKE)	26
4.7 Shear stress transport (SST)	28
4.8 Cubic k - ε (CKE)	30
5 Numerical approach	33
5.1 Finite volume method	33
5.2 Mesh tools	36
5.3 Segregated flow solver	37
5.4 Boundary conditions	37

6	Validation and verification simulations	43
6.1	Fully developed channel flow	44
6.2	Backward-facing step	52
6.3	Surface-mounted cube	62
7	Helideck simulation setup	73
7.1	Atmospheric boundary layer conditions	73
7.2	Rig model and simulation domain	76
7.3	Mesh generation	79
7.4	STAR-CCM+ field functions	81
8	Helideck simulation results	85
8.1	Initial sensitivity tests	85
8.2	Helideck analysis	92
9	Discussion	103
10	Conclusion	109
	References	111
A	Backward-facing step figures	117
B	Surface-mounted cube figures	123

Nomenclature

Roman letters

A	Area	(m ²)
\mathbf{a}	Face area vector	(m ²)
a_{ij}	Dimensionless anisotropy tensor	()
C_{kw}	Proposed scaling coefficient	()
C_T	Realizability coefficient in turbulence timescale expression	()
C_μ	Turbulence model coefficient	()
c	Speed of sound	(m s ⁻¹)
D_{ij}	Diffusion tensor	(m ² s ⁻³)
D_ω	Cross-diffusion in SST model	(s ⁻²)
d	Normal distance to nearest wall	(m)
\mathbf{ds}	Vector between cell centroids	(m)
f_i	Body force acceleration in x_i direction	(m s ⁻²)
g	Gravity acceleration	(m s ⁻²)
H	Step height in backward-facing step case	(m)
h	Height of channel	(m)
h_{ref}	Reference height	(m)
I	Turbulence intensity	()
k	Turbulence energy	(m ² s ⁻²)
k_0	Source term that counteracts turbulence decay	(m ² s ⁻²)

L	Length scale	(m)
l	Cube length in surface-mounted cube case	(m)
M	Molar mass	(kg mol ⁻¹)
\dot{m}	Mass flow rate	(kg s ⁻¹)
n_k	x_k component of the wall normal unit vector	()
P_{ij}	Production rate of Reynolds stress	(m ² s ⁻³)
P_k	Production rate of turbulence energy	(m ² s ⁻³)
P_ω	Production rate of specific dissipation rate	(s ⁻²)
p	Pressure	(kg m ⁻¹ s ⁻²)
R	Gas constant	(kg m ² s ⁻² K ⁻¹ mol ⁻¹)
Re_b	Reynolds number based on bulk velocity	()
Re_H	Reynolds number based on step height	()
Re_l	Reynolds number based on cube length	()
Re_*	Reynolds number based on friction velocity	()
Re_θ	Reynolds number based on momentum thickness	()
r_0	Equivalent sand-grain roughness length	(m)
S	Modulus of mean rate of strain	(s ⁻¹)
S_{ij}	Rate of strain	(s ⁻¹)
S_ϕ	Source term in a general transport equation	
\mathbf{s}	Vector between cell face and cell centroid	(m)
T	Turbulence timescale	(s)
t	Time	(s)
U	Velocity magnitude, $\sqrt{\overline{u}^2 + \overline{v}^2 + \overline{w}^2}$	(m s ⁻¹)
u	Velocity component in x -direction, u_1	(m s ⁻¹)
\mathbf{u}	Velocity vector	(m s ⁻¹)

u_b	Bulk velocity	(m s ⁻¹)
u_h	Velocity at reference height	(m s ⁻¹)
u_r	Reference velocity in backward-facing step case	(m s ⁻¹)
u^+	Dimensionless streamwise velocity component, \bar{u}/u_*	()
u_*	Friction velocity, $\sqrt{\tau_{wall}/\rho}$	(m s ⁻¹)
V	Volume	(m ³)
v	Velocity component in y -direction, u_2	(m s ⁻¹)
w	Velocity component in z -direction, u_3	(m s ⁻¹)
w_{rms}	Standard deviation (root-mean-square) of w	(m s ⁻¹)
x	Streamwise coordinate, x_1	(m)
\mathbf{x}	Position vector	(m)
x_l	Streamwise coordinate downstream of cube, $x - l$	(m)
x_r	Reattachment length in backward-facing step case	(m)
x'	Streamwise coordinate, origin at helideck	(m)
y	Lateral coordinate, x_2	(m)
y'	Lateral coordinate, origin at helideck	(m)
z	Vertical coordinate, x_3	(m)
z_0	Physical roughness length	(m)
z'	Vertical coordinate above helideck, $z - 48.1$ m	(m)
z^+	Dimensionless wall-normal coordinate, zu_*/ν	()
z_{wall}^+	Dimensionless distance from wall to first cell node	()

Greek letters

α	Face metric quantity	(m ⁻¹)
β^*	SST model coefficient	
Γ	Effective diffusion coefficient	(kg m ⁻¹ s ⁻¹)

Δ	Cell base size	(m)
δ_{99}	Boundary layer thickness	(m)
δ_{ij}	The Kronecker delta	()
ε	Dissipation rate	(m ² s ⁻³)
ε_0	Source term that counteracts turbulence decay	(m ² s ⁻³)
θ	Boundary layer momentum thickness	(m)
κ	The von Kármán constant, 0.41	()
λ_α	Eigenvalues of diagonalized mean rate of strain	(s ⁻¹)
μ	Dynamic molecular viscosity	(kg m ⁻¹ s ⁻¹)
μ_t	Dynamic turbulence viscosity	(kg m ⁻¹ s ⁻¹)
ν	Kinematic molecular viscosity	(m ² s ⁻¹)
ν_t	Kinematic turbulence viscosity	(m ² s ⁻¹)
ρ	Density	(kg m ⁻³)
τ	Shear stress	(kg m ⁻¹ s ⁻²)
τ_{wall}	Shear stress at wall	(kg m ⁻¹ s ⁻²)
Υ	Dilatation dissipation	(m ² s ⁻³)
Φ_{ij}	Pressure-strain tensor	(m ² s ⁻³)
ϕ	A general quantity	
Ω	Modulus of mean rate of rotation	(s ⁻¹)
Ω_{ij}	Rate of rotation	(s ⁻¹)
ω	Specific dissipation rate	(s ⁻¹)
ω_0	Source term that counteracts turbulence decay	(s ⁻¹)

Abbreviations

CFD	Computational fluid dynamics
CKE	Cubic k - ε model

CPU	Central processing unit
DNS	Direct numerical simulation
HQR	Cooper–Harper handling qualities rating scale
KFX	Kameleon FireEx
LPS	RSTM with a linear pressure-strain model
OpenFOAM	Open source field operation and manipulation
QPS	RSTM with a quadratic pressure-strain model
RKE	Realizable k - ε model
RSTM	Reynolds stress transport model
SIMPLE	Semi-implicit method for pressure-linked equations
SKE	Standard k - ε model
SKE-A	Standard k - ε model with atmospheric coefficients
SKE-D	Standard k - ε model with Durbin’s constraint
SKE-P	Standard k - ε model with Park’s constraint
SST	Shear stress transport model
STAR-CCM+	Simulation of turbulent flow in arbitrary regions – computational continuum mechanics in C++

1 Introduction

The preferred method for transportation of personnel on the Norwegian continental shelf is by use of helicopter. Helicopter transportation is inevitable onshore as well, for emergency transportation and when time is scarce. With a skilled pilot, helicopters can land almost everywhere, but the flexibility and comfort comes at a price. Turbulence may make the helicopter uncontrollable and could cause massive destruction and danger to life and environment.

To avoid possible catastrophes, related to helicopter landings and takeoffs on offshore installations on the Norwegian continental shelf, a set of requirements regarding design, arrangement, and engineering of helidecks is issued by the Norwegian petroleum industry. These requirements are given in NORSOK Standard C-004 [44]. The second edition of this standard, released in May 2013, contains new requirements regarding numerical simulations of turbulence above helidecks.

The aim of this thesis work is to evaluate the new requirements in NORSOK Standard C-004 related to numerical simulations of turbulence above helidecks. The most important part is an assessment of the “*differential turbulence model*” [44] requirement, which states that CFD analyses of helidecks should be performed using a Reynolds stress transport model. The working hypothesis is that Reynolds stress transport models provide more accurate and unambiguous results for the turbulence quantities in question, compared to simpler turbulence energy transport models. To evaluate the hypothesis, different turbulence models are tested and compared in simulations of structure induced turbulence above a helideck in a simplified offshore rig setup. The models are also tested in validation and verification simulations, and compared with experimental measurements and DNS, in order to develop confidence in assessing the general behavior of the different models.

In addition to the “*differential turbulence model*” requirement, criteria on the “*vertical velocity fluctuations*” are given in NORSOK Standard C-004 [44]. These criteria are formulated as bounds on the maximum allowed standard deviation of the vertical velocity component above the helideck of 1.75 m s^{-1} and 2.4 m s^{-1} . Violations of the criteria indicate “*noticeable turbulence*” and “*flight limitations*”, respectively. An alternative could be to limit the maximum allowed turbulence energy above the helideck. In addition to assessing and comparing both quantities in the helideck simulations, the origin of the “*vertical velocity fluctuations*” criteria is investigated.

The structure of the thesis is as follows: A review of the requirements in NORSOK Standard C-004, regarding numerical simulations of structure induced turbulence, is given in Section 2. Section 3 presents the governing equations of turbulent flows that are used in the simulations of this thesis. The different turbulence models are presented in Section 4, with a summary in Table 4.1. A brief introduction to some of the numerical aspects of the used CFD package, STAR-CCM+ v.8.06, is given in Section 5. Boundary types and conditions, with wall functions for the turbulence models, are also presented in this section. The three test cases that have been simulated, are presented in Section 6. Both case descriptions and results are given in this section, as well as some words on the necessity of simulating test cases. The setup and case description for the helideck simulations are given in Section 7. Results from the helideck simulations are then given in Section 8, followed by discussion in Section 9 and conclusion in Section 10.

2 Helideck requirements

2.1 NORSOK Standard C-004

NORSOK Standard C-004 [44] defines requirements for helidecks on offshore installations on the Norwegian continental shelf. The standard was first released in September 2004 [43], and updated with a second edition in May 2013 [44]. The second edition includes new regulations regarding wind analysis and turbulence above helidecks. There are at least three new requirements that are important for this thesis: 1. CFD analyses should comprise a given volume of air space surrounding the helideck, and a presentation of different quantities above the helideck should be given. 2. The vertical velocity fluctuations above the helideck should not exceed certain values. 3. A differential turbulence model should be used in CFD analyses of helidecks.

The first requirement is a simulation domain and measurement region constraint. NORSOK Standard C-004 states that the immediate air space surrounding the offshore installation that may induce unfavorable operational conditions at the helideck, and in the helicopter approach and departure sector, should be included in a simulation. The helicopter landing and committal points are deemed to be up to 20 m above the helideck. According to NORSOK Standard C-004, plots of the velocity magnitude, the vertical velocity component, and the vertical velocity fluctuations above the helideck should be provided. These plots are therefore given for 0 – 20 m above the helideck in the present simulations, where the values are taken from the node points of the cells above the center of the helideck.

The vertical velocity fluctuations requirement is quantified as 1.75 m s^{-1} and 2.4 m s^{-1} . This regulation is based on operational experience that have indicated that velocity fluctuations of 1.75 m s^{-1} will generate noticeable turbulence [44]. NORSOK Standard C-004 states that “*this criterion should therefore normally not be exceeded. Flight limitations are likely at values exceeding 2.4 m s^{-1} ”*. As will be explained in Section 2.2, these criteria are meant to be on the standard deviation of the vertical velocity component. The criteria may therefore be interpreted as follows.

$$w_{rms,NT} = 1.75 \text{ m s}^{-1} \tag{2.1a}$$

$$w_{rms,FL} = 2.4 \text{ m s}^{-1} \tag{2.1b}$$

Where w_{rms} is the standard deviation of the vertical velocity component, w , and NT and FL are short for noticeable turbulence and flight limitations, respectively. The standard deviation is the square root of the variance. The variance of a velocity component may be recognized as the corresponding normal component of the positive kinematic Reynolds stress tensor. The quantity is the mean of the velocity fluctuation squared, hence the subscript *rms*, is short for root-mean-square.

The third requirement is stated as follows in NORSOK Standard C-004 [44, p. 7]: “*A differential turbulence model shall be used for the simulations to provide a physical representation of the anisotropy of the turbulence field close to the helideck.*” The term *differential* turbulence model may be interpreted in various ways, which makes the term unsuited in a standard. Some refer to a differential turbulence model to be a turbulence model that solves differential equations for all components of the Reynolds stress tensor [9, p. 61]. Others use the term for a turbulence model that solves differential equations for quantities that are used in a constitutive relation to express the Reynolds stress tensor [24, 56]. The use of the word anisotropy suggests that a model which solves transport equations for all components of the Reynolds stress tensor is required. This was confirmed by one of the contributors to NORSOK Standard C-004 in a personal communication. Nevertheless, a periphrasis of the sentence, that would clarify the need for a Reynolds stress transport model, would be favorable.

2.2 Background

To understand the development of the wind analysis requirements in NORSOK Standard C-004, a look at previous reports and standards is needed. Citations to CAP 437 7th [70] and 5th [67] editions is noted explicitly in NORSOK Standard C-004 [44], hence these standards are a natural starting point.

CAP 437 is the standard for offshore helicopter landing areas for helicopters registered in the UK. It is edited by the UK Civil Aviation Authority, CAA, and its first edition was released in September 1981. The current edition is the 7th, amendment 01/2013, released in February 2013 [70].

The simulation domain and measurement region constraint is stated somewhat different than in NORSOK Standard C-004, but is found in CAP 437 as well. The volume of airspace to consider should include a height above the helideck up to the helicopter landing and take-off decision points or committal points. This is deemed to be up to 9.1 m (30 ft) plus wheels-to-rotor height as well as one rotor diameter, above the helideck. For a Sikorsky S-92, one of the more common helicopters on the Norwegian continental shelf, this would equal a height above the helideck of 31 m (9.1 m + 4.7 m + 17.1 m) [58], hence the criterion can be more restrictive in CAP 437 than in NORSOK Standard C-004.

The vertical velocity fluctuation requirement is also found in CAP 437, but the formulation is different from the one in NORSOK Standard C-004. According

to CAP 437, the standard deviation of the vertical airflow velocity should not exceed 1.75 m s^{-1} . Since the value is the same as the noticeable turbulence criterion in NORSOK Standard C-004, it is assumed that the Norwegian standard is also referring to the standard deviation of the vertical airflow velocity. As will be explained in Section 3.2, velocity components are decomposed into a mean and a fluctuating part, hence the fluctuation of the vertical velocity component, w , is given as follows.

$$w' = w - \bar{w} \quad (2.2)$$

The computational cost of calculating the vertical velocity fluctuations is likely to be too big for helideck analyses since this would require the use of detached or large eddy simulations. The standard deviation of the vertical velocity component is possible to calculate with a statistical differential turbulence model. The two quantities are, in other words, not equal, and a correction in NORSOK Standard C-004 would be favorable.

$$w_{rms} = \sqrt{(w - \bar{w})^2} = \sqrt{w'w'} \neq w' \quad (2.3)$$

The 1.75 m s^{-1} criterion was originally set to 2.4 m s^{-1} , first mentioned in CAP 437 5th edition, but was lowered in the 6th edition following completion of a validation exercise [68]. The validation exercise is reported in CAA Paper 2008/02 [69]. According to this report, the requirement was originally set to 2.4 m s^{-1} , which corresponds to the limit between safe and unsafe flying conditions, 6.5 on the Cooper–Harper handling qualities rating scale, HQR [10]. However, the relation between the standard deviation of the vertical velocity component and HQR was based on piloted simulations with three experienced pilots in ideal visual cueing conditions. The criterion was therefore lowered to 1.75 m s^{-1} , HQR = 5.5, to allow for flights in reduced cueing conditions, and for the less able or experienced pilot [69]. Another result of the validation process was withdrawal of a mean vertical wind speed criterion. This criterion was removed *“As it has not been possible to link the criterion to any helicopter performance (i.e. torque related) or handling (pilot work related) hazard“*.

CAA Paper 2008/02 [69] reveals more of the background for the 1.75 m s^{-1} criterion. Following the trails backwards in time, it seems that the criterion originates from a heavy landing incident on the Claymore accommodation platform in August 1995. No people were injured, but the Sikorsky S61N Sea King helicopter that suddenly lost its lift, as it was about to land on the platform’s helideck, was substantially damaged. The Air Accidents Investigation Branch, AAIB, concluded that the loss of lift was most likely related to heated air above the helideck, due to a gas turbine exhaust pipe situated near the helideck [64].

Turbulence around platforms was ranked as being the greatest contributor to workload and safety hazards of the fifteen factors considered, in a questionnaire survey of offshore helicopter pilots in 1997. At that time, CAP 437 contained the mentioned mean vertical wind speed criterion, but no criterion regarding turbulence. The sur-

vey highlighted the need for a turbulence criterion, which was further supported in the final report related to the heavy landing incident. This report, published in CAA Paper 99004 [65], recommended the establishment of a provisional limit for the maximum permitted level of turbulence. The limit should compare pilot experience with data obtained from corresponding wind flow studies.

In 2000, the CAA commissioned a programme of work with the primary objective of developing *"an easy-to-use maximum safe turbulence criterion for all helicopter operations to offshore helidecks"* [66]. Four years later, the research was presented in CAA Paper 2004/03 [66]. The turbulence criterion was based on an assumption that margin of safety was inversely proportional to the pilot workload. The end result was the following relation between HQR and the standard deviation of the vertical velocity component.

$$\text{HQR} = 2.77 + 1.571w_{rms} \quad (2.4)$$

Equation (2.4) was used to develop the criteria on the standard deviation of the vertical velocity component, which brings us back to the present situation. A summary of the mentioned incidents, leading to the turbulence requirements in NORSOK Standard C-004, is given in Table 2.1.

Table 2.1: Incidents leading to the turbulence requirements in NORSOK Standard C-004 [44].

Year	Incident
1995	Heavy landing at Claymore Accommodation Platform. [64]
1997	Questionnaire survey of pilots: Turbulence represents greatest workload and safety hazard. [26]
2000	Final report of heavy landing incident recommends the establishment of a turbulence criterion. [65]
2004	Following wind tunnel measurements and piloted simulations: 2.4 m s^{-1} criterion as limit between safe and unsafe flying conditions. [66]
2005	2.4 m s^{-1} criterion mentioned in CAP 437 5th edition. [67]
2008	1.75 m s^{-1} criterion established in CAP 437 6th edition. [68]
2009	Validation report suggests lowering of turbulence criterion and withdrawal of vertical mean wind speed criterion. [69]
2013	1.75 m s^{-1} and 2.4 m s^{-1} , as well as the need for a differential turbulence model, in NORSOK Standard C-004. [44]

2.3 Proposed turbulence energy criteria

The standard deviation of the vertical airflow velocity was chosen to be the turbulence criterion “*on the basis that it most closely relates to the others measurements.*” [66, App. T, p. 2]. Initially, four different platform models were tested, at different wind speeds and headings, in a wind tunnel, but only the Brae A model was reused to validate the measurements. For economic reasons, only one platform model was considered. In addition, “*the different turbulence conditions experienced for the different wind conditions for Brae A adequately encompassed all conditions experienced for the other three simulations*” [66, Section 3, p. 5]. The term *others measurements* may therefore be interpreted as measurements of the other platform models, that were considered good enough documented by the different wind conditions for Brae A.

The wind tunnel measurements for Brae A can be found in CAA Paper 2004/03 [66, App. T]. Based on data for the highest wind speed, 60 kt (31 m s^{-1}), variances of the velocity components are calculated and presented in Table 2.2. Included is also the relative difference between the different wind headings, with reference to the average of the four wind headings, as well as the turbulence energy, k , which is calculated as follows.

$$k = \frac{1}{2} \left(\overline{u'_i u'_i} \right) = \frac{1}{2} \left(\overline{u' u'} + \overline{v' v'} + \overline{w' w'} \right) \quad (2.5)$$

Table 2.2: Variances of velocity components at different wind headings with 60 kt wind speed for Brae A [66]. Brackets: Relative difference compared to the mean of the four wind headings.

	001°	050°	272°	088°
$\overline{u' u'} \text{ [m}^2 \text{ s}^{-2}\text{]}$	15.82 (27 %)	8.72 (−30 %)	8.58 (−31 %)	16.87 (35 %)
$\overline{v' v'} \text{ [m}^2 \text{ s}^{-2}\text{]}$	9.00 (0 %)	13.26 (48 %)	6.61 (−26 %)	6.98 (−22 %)
$\overline{w' w'} \text{ [m}^2 \text{ s}^{-2}\text{]}$	7.81 (24 %)	5.58 (−12 %)	6.18 (−2 %)	5.67 (−10 %)
$k \text{ [m}^2 \text{ s}^{-2}\text{]}$	16.32 (18 %)	13.78 (−1 %)	10.69 (−23 %)	14.76 (6 %)

As can be seen in Table 2.2, the relative difference of the variance of the vertical velocity component is indeed the least varying of the three components. However, half the sum of the three components, the turbulence energy, k , varies with the same magnitude. Since the turbulence criterion was chosen to be based on the standard deviation of the vertical velocity component, because it was the least varying component, the turbulence criterion may be based on the turbulence energy instead.

Notice that the requirements in NORSOK Standard C-004 are on the standard deviation of the vertical velocity component, not the variance. However, to make a sensible comparison with the turbulence energy, the variance is used since these quantities have the same units. Alternatively, the square root of the turbulence

energy could have been compared with the standard deviations. This end result using this approach is the same, \sqrt{k} and w_{rms} vary with the same magnitude.

NORSOK Standard C-004 seems to have followed CAP 437, but the *differential* turbulence model criterion has not been found in any of the mentioned CAA and CAP reports. Since the meaning of a differential turbulence model was a Reynolds stress transport model, the requirement may be due to the need for an accurate measure of the standard deviation of the vertical airflow velocity. The standard deviation may be estimated by simpler models as well, by use of a constitutive relation that expresses the Reynolds stress tensor. However, such constitutive relations may have shortcomings for flows with strong anisotropy [50, p. 458].

One of the main aspects of this thesis is to evaluate the need for Reynolds stress transport models in helideck simulations. Since these models require seven additional transport equations in order to close the Reynolds-averaged momentum equation, they are likely to be more computational expensive than turbulence energy transport models which typically use two additional transport equations. The additional transport equations in a Reynolds stress transport model may also give rise to problems regarding boundary conditions, as well as stability issues and numerical stiffness. Using Reynolds stress transport models are therefore likely to demand both more knowledge and time from the user, compared to simpler turbulence energy transport models. The turbulence criterion was intended to be "easy-to-use" [66], but using a Reynolds stress transport model may not be trivial.

The wind tunnel measurements at 60 kt (31 m s^{-1}) for all wind headings were presented in Table 2.2. Table 2.3 presents the relative difference for all velocities at each wind heading compared to the mean of all wind headings.

Table 2.3: Relative difference of the velocity variances for all wind speeds (15 kt, 25 kt, 35 kt, 50 kt, 60 kt) at each wind heading, compared to the mean of all wind headings.

Relative difference	001°	050°	272°	088°
$\overline{u'u'}$	29 %	-29 %	-38 %	38 %
$\overline{v'v'}$	-11 %	49 %	-17 %	-22 %
$\overline{w'w'}$	18 %	-14 %	6 %	-10 %
k	13 %	1 %	-21 %	7 %

Table 2.3 confirms the data from Table 2.2, the variations in k are of the same magnitude as the variations in $\overline{w'w'}$, both considerably smaller than the variations in $\overline{u'u'}$ and $\overline{v'v'}$. If k is accepted as a turbulence criterion, one could scale k with $\overline{w'w'}$ in order to get values for the turbulence energy corresponding to standard deviations of the vertical airflow velocity of 1.75 m s^{-1} and 2.4 m s^{-1} .

$$k = C_{kw} \overline{w'w'} \quad (2.6)$$

Based on the sample of 20 wind conditions, five wind speeds at four headings

[66, App. T], an average value for C_{kw} is calculated to be 2.22. The consistency between the values for $\overline{w'w'}$ and k are, in most cases, good, but wind heading 272° has significantly smaller C_{kw} -values than the other three wind headings. If the criterion were to be based on this wind heading alone, C_{kw} would have to be 1.63. However, since the total amount of turbulence is important, and the standard deviation of the vertical velocity component was chosen based on being the least varying component only, $C_{kw} = 1.63$ would be too conservative. If $C_{kw} = 2.22$ is accepted, the following expressions for k is achieved.

$$k = 2.22\overline{w'w'} \longrightarrow \overline{w'w'} = 0.45k \quad (2.7)$$

Notice that a simple isotropic assumption, $\overline{w'w'} = \frac{2}{3}k$, is a 48 % increase of the expression in Eq. (2.7). Silva et al. [59] used turbulence energy transport models in helideck simulations, and assumed $\overline{w'w'} = \frac{2}{3}k$. They suggested that Reynolds stress transport models should be tested in helideck simulations due to strong anisotropy. This may be an explanation for the *differential* turbulence model requirement in NORSOK Standard C-004. Even though the formulation for the variance of the vertical velocity component with a turbulence energy transport model is more sophisticated than $\overline{w'w'} = \frac{2}{3}k$, the expression is likely to be incapable of returning the correct anisotropy.

Two values for the standard deviation of the vertical velocity component are used in NORSOK Standard C-004. Corresponding values may be calculated for the turbulence energy by use of Eq. (2.7). The "noticeable turbulence" criterion, $w_{rms} = 1.75 \text{ m s}^{-1}$, corresponds to $k = 6.8 \text{ m}^2 \text{ s}^{-2}$, while the "flight limitations" criterion, $w_{rms} = 2.4 \text{ m s}^{-1}$, corresponds to $k = 12.8 \text{ m}^2 \text{ s}^{-2}$. By use of two significant figures, the proposed criteria for k are given as follows.

$$k_{NT} = 6.8 \text{ m}^2 \text{ s}^{-2} \quad (2.8a)$$

$$k_{FL} = 13 \text{ m}^2 \text{ s}^{-2} \quad (2.8b)$$

The values for the standard deviation criteria, 1.75 m s^{-1} and 2.4 m s^{-1} , were chosen because they represented $\text{HQR} = 5.5$ and $\text{HQR} = 6.5$, respectively, limits between safe and unsafe flight conditions [66]. With the proposed relation for the turbulence energy, Eq. (2.7), HQR -values from Eq. (2.4), can be calculated.

$$\text{HQR} = 2.77 + 1.571\sqrt{\frac{k}{C_{kw}}} = 2.77 + 1.054\sqrt{k} \quad (2.9)$$

HQR -values have been calculated from the wind tunnel measurements of Brae A [66] based on the measured standard deviation of the vertical velocity component and Eq. (2.4), and by use of the turbulence energy and Eq. (2.9). The results are listed in Table 2.4. Blue text color represents the wind conditions that would exceed the $\text{HQR} = 5.5$ criterion, while red text color is used for wind conditions that exceeds the $\text{HQR} = 6.5$ criterion.

Table 2.4: HQR-values when calculated according to the original criterion for w_{rms} (left), and from the proposed criteria on k (right).

kt	001°		050°		272°		088°	
15	3.82	3.77	3.60	3.62	3.78	3.62	3.70	3.69
25	4.59	4.59	4.32	4.49	4.50	4.25	4.23	4.43
35	5.15	5.08	4.97	5.18	5.13	4.78	5.06	5.43
50	6.36	6.19	5.86	6.13	6.17	5.67	5.89	6.01
60	7.16	7.03	6.48	6.68	6.68	6.22	6.51	6.82

The criterion for k is sufficient for all wind headings except 272°. However, a criterion on k would also indicate flight limitations on the 050° 60 kt case, due to a large $\overline{v'v'}$ (see Table 2.2), a scenario that would not be limited by the criterion on w_{rms} .

A turbulence criterion based on the turbulence energy would make turbulence energy transport models better suited for helideck simulations. As opposed to a criterion on the standard deviation of the vertical velocity component, it would detect dangerous flying conditions for wind conditions with high degree of turbulence in the horizontal plane, but with a minor standard deviation of the vertical velocity component. According to personal communications with offshore helicopter pilots, turbulence in the horizontal plane may be just as dangerous as turbulence in the vertical direction. This is also pointed out by Silva et al. [59], who question a turbulence criterion that does not take into account turbulence in the horizontal plane. A solution could be to have individual criteria on all three normal components, but a criterion on the total amount of turbulence energy would be easier to use, which was highlighted in the initial development of the turbulence criterion [66].

3 Turbulent flows

3.1 Governing equations

All flows in this thesis are considered to be incompressible and isothermal. The flow field may therefore be described with the continuity and momentum equations, without solving the energy equation. For the case of Newtonian fluids with negligible bulk viscosity, the equations take the following form [18, p. 24].

$$\frac{\partial \rho}{\partial t} + \frac{\partial}{\partial x_j}(\rho u_j) = 0 \quad (3.1)$$

$$\frac{\partial}{\partial t}(\rho u_i) + \frac{\partial}{\partial x_j}(\rho u_i u_j) = \frac{\partial}{\partial x_j} \left(-p \delta_{ij} + 2\mu S_{ij} - \frac{2}{3}\mu \frac{\partial u_l}{\partial x_l} \delta_{ij} \right) + \rho f_i \quad (3.2)$$

The rate of strain, S_{ij} , is defined as follows.

$$S_{ij} = \frac{1}{2} \left(\frac{\partial u_i}{\partial x_j} + \frac{\partial u_j}{\partial x_i} \right) \quad (3.3)$$

The continuity equation, Eq. (3.1), is the simple differential form for conservation of mass in single-phase flows [72, p. 229]. The momentum equation, Eq. (3.2), may be interpreted as Newton's second law of motion for a fluid particle in the three coordinate directions. The acceleration of a fluid particle, on the left hand side, is equal to the surface and body forces, on the right hand side, experienced by the fluid particle [50, p. 16]. Surface forces, hydrostatic pressure and viscous stress, work on the surfaces of the fluid particle, while body forces work on the entire mass of the fluid particle [72, p. 235].

Air is the flowing fluid in all simulations in this thesis. In STAR-CCM+, the ideal gas law is used to provide an expression for density [7, p. 2981]. Since the flows are assumed isothermal, and the composition of air is assumed constant, density becomes a function of the pressure only.

$$\rho = \frac{pM}{RT} = \text{const} \times p \quad (3.4)$$

Even though there are pressure variations in the simulations, these variations are

negligible compared to the reference atmospheric pressure. The density may therefore be treated as constant. The ideal gas model is used together with an isothermal temperature specification in the helideck simulations, presented in Section 7, while the validation and verification simulations of Section 6, use a constant density model in order to specify the density explicitly for a given Reynolds number.

With constant or almost constant density and no temperature variations, the effect of gravity on the flow is negligible. The body force term in Eq. (3.2) is therefore neglected in the present simulations.

3.2 Reynolds decomposition and averaging

Turbulence is a chaotic phenomena characterized by rapid fluctuations of the flow variables. Solving the governing equations directly is resource demanding and not an option for industrial problems. Instead, averaged equations are solved for averaged flow variables. With the assumption of constant density, Reynolds decomposition is well suited, and the mass-weighted Favre decomposition is not needed. A quantity, ϕ , is decomposed into a mean, $\bar{\phi}$, which may be thought of as a time average of ϕ , and a fluctuation, ϕ' [18, p. 35].

$$\phi = \bar{\phi} + \phi' \quad (3.5)$$

The viscosity of air at atmospheric conditions depends mostly on temperature [72, p. 29]. Since the simulations are isothermal, the viscosity is assumed to be constant. The quantities that are Reynolds decomposed from Eqs. (3.1) and (3.2), are therefore the velocity components and the pressure.

$$u_i = \bar{u}_i + u'_i \quad (3.6)$$

$$p = \bar{p} + p' \quad (3.7)$$

Reynolds-averaged equations for continuity and momentum are found by inserting the Reynolds decomposed quantities, Eqs. (3.6) and (3.7), in the continuity and momentum equations, Eqs. (3.1) and (3.2). The equations are then averaged, and terms equal to zero are removed. With the above assumption, the Reynolds-averaged continuity and momentum equations may be written as follows.

$$\frac{\partial \bar{u}_j}{\partial x_j} = 0 \quad (3.8)$$

$$\frac{\partial}{\partial t}(\rho \bar{u}_i) + \frac{\partial}{\partial x_j}(\rho \bar{u}_i \bar{u}_j) = \frac{\partial}{\partial x_j} \left(-\bar{p} \delta_{ij} + 2\mu \bar{S}_{ij} - \frac{2}{3} \mu \frac{\partial \bar{u}_l}{\partial x_l} \delta_{ij} - \overline{\rho u'_i u'_j} \right) \quad (3.9)$$

The transient term in the Reynolds-averaged continuity equation is neglected since the derivation of the equations assume constant density. The new term in the Reynolds-averaged momentum equation, $-\overline{\rho u'_i u'_j}$, is the Reynolds stress tensor

which represents the net transfer of momentum by turbulence fluctuations [50, p. 87]. It is symmetric and consists of six unknowns. Together with the velocity components and pressure, there are ten unknowns in Eqs. (3.8) and (3.9), but only four equations. This closure problem is solved by models for the Reynolds stress tensor, that is, turbulence models.

3.3 Transport equations for turbulence quantities

3.3.1 Reynolds stress transport equations

Two of the turbulence models that are used in this thesis solve transport equations for the components of the Reynolds stress tensor¹. A transport equation for the Reynolds stress tensor may be derived from the continuity and momentum equations. The end result for constant density flows is presented below [18, p. 95].

$$\begin{aligned} \frac{\partial}{\partial t} \left(\overline{\rho u'_i u'_j} \right) + \frac{\partial}{\partial x_k} \left(\overline{\rho u'_i u'_j \bar{u}_k} \right) = & - \left(\overline{\rho u'_i u'_k} \frac{\partial \bar{u}_j}{\partial x_k} + \overline{\rho u'_j u'_k} \frac{\partial \bar{u}_i}{\partial x_k} \right) + \frac{\partial}{\partial x_k} \left(\mu \frac{\partial \overline{u'_i u'_j}}{\partial x_k} \right) \\ & + \frac{\partial}{\partial x_k} \left(-\overline{\rho u'_i u'_j u'_k} - \left(\overline{p' u'_i \delta_{jk}} + \overline{p' u'_j \delta_{ik}} \right) \right) \\ & + p' \left(\frac{\partial \overline{u'_i}}{\partial x_j} + \frac{\partial \overline{u'_j}}{\partial x_i} \right) - 2\mu \frac{\partial \overline{u'_i}}{\partial x_k} \frac{\partial \overline{u'_j}}{\partial x_k} \end{aligned} \quad (3.10)$$

The five terms on the right hand side of Eq. (3.10) may be interpreted, from left to right, as production, viscous and turbulence diffusion, pressure-strain, and dissipation [7, p. 3429]. The main difference between the two Reynolds stress transport models that are tested in this thesis, is the modeling of the pressure-strain term. The modeled transport equations for the Reynolds stress components that are used in the simulations of this thesis, are presented in Section 4.1.

3.3.2 Turbulence energy transport equation

Simpler turbulence models may solve a transport equation for the turbulence energy, defined in Eq. (2.5), instead of transport equations for the components of the Reynolds stress tensor, hence they may be called turbulence energy transport models. Since these turbulence models tend to use two transport equations, they are often called two-equation models. The linkage to the Reynolds stress tensor is by use of a constitutive relation that contains a turbulence/eddy viscosity, explained in Section 4.4, hence these models are also referred to as turbulence/eddy

¹Strictly speaking, $-\overline{\rho u'_i u'_j}$ is the Reynolds stress tensor, but the kinematic Reynolds stress tensor without the negative sign, $\overline{u'_i u'_j}$, is also referred to as the Reynolds stress tensor in this thesis. This is convenient and consistent with the literature [50, p. 86].

viscosity models. The terms turbulence energy transport models and turbulence viscosity are used in this thesis.

Like the transport equation for the Reynolds stress tensor, the equation for the turbulence energy may be derived from the continuity and momentum equations. For constant density flows, the equation is given as follows [18, p. 49].

$$\begin{aligned} \frac{\partial}{\partial t}(\rho k) + \frac{\partial}{\partial x_j}(\rho k \bar{u}_j) = & - \overline{\rho u'_i u'_j} \frac{\partial \bar{u}_i}{\partial x_j} + \frac{\partial}{\partial x_j} \left(\mu \frac{\partial k}{\partial x_j} \right) \\ & \frac{\partial}{\partial x_j} \left(-\frac{1}{2} \overline{\rho u'_i u'_i u'_j} - \overline{p' u'_j} \right) - \mu \frac{\partial u'_i}{\partial x_j} \frac{\partial u'_i}{\partial x_j} \end{aligned} \quad (3.11)$$

The terms on the right hand side are similar to the right hand side terms of Eq. (3.10), but there is no pressure-strain term. The turbulence energy is half the sum of the normal Reynolds stress components, and the sum of the normal components of the strain fluctuations are zero for constant density flows, found by subtracting the continuity equation, Eq. (3.1), from the Reynolds-averaged continuity equation, Eq. (3.8), with the assumptions of constant density. Due to the absence of the pressure-strain term, the transport equation for turbulence energy is considered easier to model than the transport equation for the Reynolds stress tensor [50, p. 459]. The modeled transport equation for turbulence energy used in this thesis, is given in Section 4.5.

3.3.3 Dissipation rate transport equation

The dissipation rate is found in both the Reynolds stress transport equation, Eq. (3.10), and in the turbulence energy transport equation, Eq. (3.11). A simple isotropic model that relates the two expressions is used in STAR-CCM+, in order to use the same dissipation rate transport equation for Reynolds stress transport models as for the standard k - ε model [7, p. 3300].

$$\rho \varepsilon_{ij} = \frac{2}{3} \rho \varepsilon \delta_{ij} = \frac{2}{3} \left(\mu \frac{\partial u'_i}{\partial x_j} \frac{\partial u'_i}{\partial x_j} \right) \delta_{ij} \quad (3.12)$$

All turbulence models used in this thesis solve a transport equation for a dissipation quantity, in addition to the transport equations for the Reynolds stress components or the transport equation for the turbulence energy. Most common are models based on the dissipation rate, ε , but a model based on the specific dissipation rate, ω , is also tested in this thesis. The specific dissipation rate is related to the dissipation rate in the following manner.

$$\omega = \frac{\varepsilon}{k \beta^*} \quad (3.13)$$

Where k is the turbulence energy and β^* is a turbulence model coefficient.

Like the transport equations for the Reynolds stress tensor and the turbulence energy, an exact equation for the dissipation rate may be derived from the continuity and momentum equations [73, p. 88].

$$\begin{aligned}
 \frac{\partial}{\partial t}(\rho\varepsilon) + \frac{\partial}{\partial x_j}(\rho\varepsilon\bar{u}_j) = & -2\mu \left(\overline{\frac{\partial u'_i}{\partial x_k} \frac{\partial u'_j}{\partial x_k}} + \overline{\frac{\partial u'_k}{\partial x_i} \frac{\partial u'_k}{\partial x_j}} \right) \frac{\partial \bar{u}_i}{\partial x_j} - 2\mu \overline{u'_k \frac{\partial u'_i}{\partial x_j} \frac{\partial^2 \bar{u}_i}{\partial x_k \partial x_j}} \\
 & - 2\mu \overline{\frac{u'_i}{x_k} \frac{u'_i}{x_m} \frac{u'_k}{x_m}} - 2\mu\nu \overline{\left(\frac{\partial^2 \bar{u}'_i}{\partial x_k \partial x_m} \right)^2} \\
 & + \frac{\partial}{\partial x_j} \left(\mu \frac{\partial \varepsilon}{\partial x_j} - \overline{\mu u'_j \frac{\partial u'_i}{\partial x_m} \frac{\partial u'_i}{\partial x_m}} - 2\nu \overline{\frac{\partial p'}{\partial x_m} \frac{\partial u'_j}{\partial x_m}} \right)
 \end{aligned} \tag{3.14}$$

Compared to the transport equation for turbulence energy, the dissipation rate equation is far more complex and contains nontrivial terms that are hard to measure in experiments [73, p. 88]. In some models, like the standard k - ε model, the right hand side terms of Eq. (3.14), which may be recognized as production, diffusion, and dissipation terms, are modeled similarly to the terms of the modeled transport equation for turbulence energy. This traditional approach is considered one of the weaknesses with the standard k - ε model, and the reason for the jet anomaly [49, p. 116]. An alternative formulation for the dissipation rate equation is used in the realizable k - ε model. These models are further explained in Sections 4.

4 Turbulence models

Different turbulence models are used in the simulations of this thesis. All of them are presented in this section. A brief summary is given in Table 4.1. NORSOK Standard C-004 [44] requires the use of a Reynolds stress transport model for helideck simulations. Two Reynolds stress transport models are therefore tested in the simulations. Turbulence models may also be based on a transport equation for the turbulence energy. This approach is in general faster and easier to use, and has been tested and compared to the Reynolds stress transport models to evaluate the need for a Reynolds stress transport model in helideck simulations. For modeling of atmospheric boundary layer flows, STAR-CCM+ recommends to use a turbulence model with wall functions [7, p. 6319]. Consequently, all models are used with wall functions to specify boundary conditions close to walls, further explained in Section 5.4.4.

Table 4.1: Turbulence models used in this thesis.

Model	Section	Description
LPS	4.2	Reynolds stress transport model with a linear pressure-strain model by Gibson and Launder [21]
QPS	4.3	Reynolds stress transport model with a quadratic pressure-strain model by Speziale, Sarkar, and Gatski [61]
SKE	4.5	Standard k - ε model by Jones and Launder [27] with coefficients by Launder and Sharma [31]
SKE-A	4.5.1	Modified standard k - ε model with atmospheric coefficients by Duynkerke [16]
SKE-D	4.5.2	Modified standard k - ε model with turbulence timescale constraint by Durbin [15] [39]
SKE-P	4.5.2	Modified standard k - ε model with turbulence timescale constraint by Park and Park [48]
RKE	4.6	Realizable k - ε model by Shih et al. [57]
SST	4.7	Shear stress transport model by Menter [40]
CKE	4.8	Standard k - ε model with a cubic constitutive relation by Lien, Chen, and Leschziner [35]

4.1 Reynolds stress transport models

There are two Reynolds stress transport models implemented in STAR-CCM+. The first use a linear model for the pressure-strain term of Eq. (3.10), while the second use a quadratic model for this term. The two Reynolds stress transport models solve the same transport equations, that is, one equation for each Reynolds stress component and one equation for the dissipation rate. The transport equation for the Reynolds stress tensor is given as follows in STAR-CCM+ [7, p. 3429].

$$\frac{\partial}{\partial t} \left(\overline{\rho u'_i u'_j} \right) + \frac{\partial}{\partial x_k} \left(\overline{\rho u'_i u'_j \bar{u}_k} \right) = \rho P_{ij} + \rho D_{ij} - \frac{2}{3} \rho (\varepsilon + \Upsilon) \delta_{ij} + \rho \Phi_{ij} \quad (4.1)$$

The right hand side terms correspond to production, diffusion, dissipation, and pressure-strain, that were found in the derived equation for the Reynolds stress tensor, Eq. (3.10). The production rate of Reynolds stress is obtained without modeling.

$$P_{ij} = - \left(\overline{u'_i u'_k} \frac{\partial \bar{u}_j}{\partial x_k} + \overline{u'_j u'_k} \frac{\partial \bar{u}_i}{\partial x_k} \right) \quad (4.2)$$

The diffusion tensor consists of molecular diffusion, which does not need further modeling, and turbulence diffusion that can be modeled by two different approaches in STAR-CCM+ [7, p. 3429]. The turbulence diffusion term is modeled with the isotropic formulation by Lien and Leschziner [34] by default, which gives the following total diffusion.

$$D_{ij} = \frac{\partial}{\partial x_k} \left(\left(\nu + \frac{\nu_t}{\sigma_k} \right) \frac{\partial \overline{u'_i u'_j}}{\partial x_k} \right) \quad (4.3)$$

Where $\sigma_k = 0.82$ [7, p. 3429].

As an alternative to the isotropic formulation, the Reynolds stress diffusion may be modeled by the generalized gradient diffusion model by Daly and Harlow [11], but this approach can result in numerical instabilities [34]. The standard turbulence gradient diffusion model, Eq. (4.3), is therefore used in this thesis.

The turbulence viscosity in Eq. (4.3), is computed as follows.

$$\nu_t = C_\mu \frac{k^2}{\varepsilon} \quad (4.4)$$

C_μ is a constant with the value $C_\mu = 0.065536$ in the linear pressure-strain model and $C_\mu = 0.098596$ in the quadratic pressure-strain model. These values are not explained in the documentation, but are, according to the STAR-CCM+ support service, based on the relation between the kinematic Reynolds shear stress and the

turbulence energy in the log-law region.

$$C_\mu = \left(\frac{\overline{u'w'}}{k} \right)^2 \quad (4.5)$$

This gives the following values for the Reynolds stress transport models.

$$C_{\mu,LPS} = (0.256)^2 = 0.065536 \quad (4.6a)$$

$$C_{\mu,QPS} = (0.314)^2 = 0.098596 \quad (4.6b)$$

In addition to the dissipation rate, ε , a dilatation dissipation term, Υ , that accounts for compressibility effects, is added as standard in STAR-CCM+.

$$\Upsilon = \frac{C_M k \varepsilon}{c^2} \quad (4.7)$$

Where $C_M = 2$ is a constant and c is the speed of sound. The dilatation dissipation term is treated the same way for the k - ε models that will be presented in later sections. The formulation contains the dissipation rate, ε , which makes it easy to compare the two terms.

$$\varepsilon + \Upsilon = \varepsilon \left(1 + \frac{C_M k}{c^2} \right) \quad (4.8)$$

With $c \approx 340 \text{ ms}^{-1}$ and $C_M = 2$, the dilatation dissipation term becomes negligible compared to the dissipation rate for all simulations in this thesis. Even for turbulence energy levels of $k = 50 \text{ m}^2 \text{ s}^{-2}$, which is more than what is typically found in the present simulations, the term is less than 0.1 % of the dissipation rate.

The dissipation rate is given as a scalar in Eq. (4.1), where Eq. (3.12) has been inserted for the dissipation rate tensor. As mentioned in Section 3.3.3, the dissipation rate tensor is assumed isotropic and the transport equation for the dissipation rate is modeled similar to the one used in the standard k - ε model [7, p. 3520]¹.

$$\frac{\partial}{\partial t}(\rho\varepsilon) + \frac{\partial}{\partial x_j}(\rho\varepsilon\bar{u}_j) = \frac{\partial}{\partial x_j} \left(\left(\mu + \frac{\mu_t}{\sigma_\varepsilon} \right) \frac{\partial \varepsilon}{\partial x_j} \right) + C_{\varepsilon 1} \rho \frac{\varepsilon}{k} \frac{1}{2} P_{ii} - C_{\varepsilon 2} \rho \frac{\varepsilon^2}{k} \quad (4.9)$$

The modeling of the last term of Eq. (4.1), the pressure-strain term, Φ_{ij} is the main difference between the two Reynolds stress transport models in this thesis. The pressure-strain term is responsible for the redistribution of energy between the Reynolds stress components. This term is crucial since redistribution is a dominant process in the balance of the Reynolds stress components. The pressure-strain term is therefore considered the most important term to be modeled in

¹The STAR-CCM+ documentation contains a typing error in the dissipation rate equation for the Reynolds stress transport models, where the one-half in front of the production term is left out. According to the STAR-CCM+ support service, this is an error in the documentation only.

Reynolds stress transport models, and a variety of different proposals have been given in the literature [50, p. 316, pp. 387–390]. Two models are implemented in STAR-CCM+, and explained in the sections to follow.

4.2 Linear pressure-strain (LPS)

The linear pressure-strain model in STAR-CCM+ is abbreviated the LPS model in this thesis. The model is based on the formulation by Gibson and Launder [21]. The pressure-strain term is split in two parts, where each part has an additional wall-reflection term. Wall-reflection terms are added since the pressure fluctuations are reflected from walls, an effect that is not only important in the typical low-Reynolds region, but also far from walls [18, p. 102].

$$\Phi_{ij} = \Phi_{ij,1} + \Phi_{ij,2} + \Phi_{ij,1,w} + \Phi_{ij,2,w} \quad (4.10)$$

Where the four terms are given as follows.

$$\Phi_{ij,1} = -C_1 \frac{\varepsilon}{k} \left(\overline{u'_i u'_j} - \frac{2}{3} k \delta_{ij} \right) \quad (4.11a)$$

$$\Phi_{ij,2} = -C_2 \left(P_{ij} - \frac{1}{3} P_{kk} \delta_{ij} \right) \quad (4.11b)$$

$$\Phi_{ij,1,w} = C_{1w} \frac{\varepsilon}{k} \left(\overline{u'_k u'_m n_k n_m} \delta_{ij} - \frac{3}{2} \overline{u'_i u'_k} n_j n_k - \frac{3}{2} \overline{u'_j u'_k} n_i n_k \right) f_w \quad (4.11c)$$

$$\Phi_{ij,2,w} = C_{2w} \left(\Phi_{km,2} n_k n_m \delta_{ij} - \frac{3}{2} \Phi_{ik,2} n_j n_k - \frac{3}{2} \Phi_{jk,2} n_i n_k \right) f_w \quad (4.11d)$$

Where n_k is the x_k component of the wall normal unit vector. The coefficient f_w is defined as a function of the normal distance to the nearest wall, d .

$$f_w = \min \left[\frac{k^{\frac{3}{2}}}{C_l \varepsilon d}, 1.4 \right] \quad (4.12)$$

As can be seen in Eq. (4.11), the first part of the pressure-strain term, index 1, is dependent on turbulence quantities, while the last term, index 2, is dependent on turbulence quantities times mean velocity gradients, see Eq. (4.2). The redistribution of energy between Reynolds stress components is dependent on both parts, which is the idea behind this split of the pressure-strain term [18, p. 101].

The coefficients in the LPS model are given in Table 4.2.

Table 4.2: Coefficients in the LPS model in STAR-CCM+.

C_μ	C_M	σ_ε	$C_{\varepsilon 1}$	$C_{\varepsilon 2}$	C_1	C_2	C_{1w}	C_{2w}	C_l
0.065536	2	1.0	1.44	1.92	1.8	0.6	0.5	0.3	2.5

4.3 Quadratic pressure-strain (QPS)

The quadratic pressure-strain model in STAR-CCM+, abbreviated the QPS model in this thesis, is based on the formulation by Speziale, Sarkar, and Gatski [61]. The pressure-strain term is modeled with quadratic functions of the anisotropy tensor, the mean rate of strain, and the mean rate of rotation. The expression is given as follows [61] [7, p. 3433].

$$\begin{aligned} \Phi_{ij} = & - \left(C_{s1}\varepsilon + C_{r4}\frac{1}{2}P_{kk} \right) a_{ij} + \\ & C_{s2}\varepsilon \left(a_{ik}a_{kj} - \frac{1}{3}a_{mn}a_{mn}\delta_{ij} \right) + (C_{r3} - C_{r3}^*\sqrt{a_{mn}a_{mn}}) k\bar{S}_{ij} + \\ & C_{r1}k \left(a_{ik}\bar{S}_{jk} + a_{jk}\bar{S}_{ik} - \frac{2}{3}a_{mn}\bar{S}_{mn}\delta_{ij} \right) + C_{r2}k (a_{ik}\bar{\Omega}_{jk} + a_{jk}\bar{\Omega}_{ik}) \end{aligned} \quad (4.13)$$

Where a_{ij} is the dimensionless anisotropy tensor, S_{ij} is defined in Eq. 3.3, and $\bar{\Omega}_{ij}$ is the mean rate of rotation.

$$a_{ij} = \frac{\overline{u'_i u'_j}}{k} - \frac{2}{3}\delta_{ij} \quad (4.14)$$

$$\bar{\Omega}_{ij} = \frac{1}{2} \left(\frac{\partial \bar{u}_i}{\partial x_j} - \frac{\partial \bar{u}_j}{\partial x_i} \right) \quad (4.15)$$

The QPS model is more modern and likely the Reynolds stress transport model of choice, according to the STAR-CCM+ documentation [7, p. 3513]. The model is found to give superior performance in a range of basic shear flows [2, p. 86]. The first line of Eq. (4.13) is similar to the two first terms of Eq. (4.11), but unlike the LPS model, the QPS model does not contain specific terms to account for wall-reflection effects. Such wall-reflection terms are not needed in order to obtain satisfactory solutions with the quadratic pressure-strain model [2, p. 87].

The coefficients in the QPS model are given in Table 4.3.

Table 4.3: Coefficients in the QPS model in STAR-CCM+.

C_μ	σ_ε	$C_{\varepsilon 1}$	$C_{\varepsilon 2}$	C_{s1}	C_{s2}	C_{r1}	C_{r2}	C_{r3}	C_{r3}^*	C_{r4}
0.098596	1.22	1.44	1.83	1.7	1.05	0.625	0.2	0.8	0.65	0.9

4.4 Turbulence energy transport models

Instead of solving transport equations for all Reynolds stress components, a constitutive equation that relates the Reynolds stress tensor to other quantities, may be used. The most common constitutive model is the Boussinesq turbulence viscosity assumption. Analogous to the viscous stresses of a Newtonian fluid, the anisotropic part of the Reynolds stress tensor is assumed proportional to the mean rate of strain [71, p. 67].

$$-\overline{\rho u'_i u'_j} = 2\mu_t \overline{S}_{ij} - \frac{2}{3} \left(\rho k + \mu_t \frac{\partial \overline{u}_l}{\partial x_l} \right) \delta_{ij} \quad (4.16)$$

Where μ_t is an isotropic scalar, equal in every direction, known as the turbulence viscosity. The assumption reduces the six unknown Reynolds stress components to two new unknowns, the turbulence energy, k , and the turbulence viscosity, μ_t . The standard k - ε model, the realizable k - ε model, and the shear stress transport model use the Boussinesq viscosity assumption, while the cubic k - ε model uses a nonlinear constitutive relation that is presented in Section 4.8. These models solve a transport equation for the turbulence energy as well as a transport equation for the dissipation rate. The shear stress transport model is based on a k - ω formulation, which means that this model solves a transport equation for the specific dissipation rate instead of the dissipation rate. The turbulence viscosity is then found from an expression that combines the turbulence energy and the dissipation rate.

With the Boussinesq viscosity assumption, the variance of the vertical velocity component is calculated as follows.

$$\overline{w'w'} = -2\nu_t \frac{\partial \overline{w}}{\partial z} + \frac{2}{3}k + \nu_t \left(\frac{\partial \overline{u}}{\partial x} + \frac{\partial \overline{v}}{\partial y} + \frac{\partial \overline{w}}{\partial z} \right) \quad (4.17)$$

Where the three terms correspond to the strain rate term, the turbulence energy term and the velocity gradient term of Eq. (4.16). For constant density flows, the velocity gradient term is zero from the Reynolds-averaged continuity equation, Eq. (3.8). The flows in this thesis have, as mentioned in Section 3.2, negligible density variations, and the term may therefore be neglected. The strain rate term, on the other hand, should not be neglected, as the vertical velocity gradient may be non-zero even though the sum of the three velocity gradients is negligible.

One of the main flaws of the Boussinesq turbulence viscosity assumption is the incapability of returning the correct anisotropy. The assumption that the anisotropic part of the Reynolds stress tensor is proportional to the mean rate of strain is known to be incorrect in a number of flows [50, p. 94]. For helideck simulations, the use of the Boussinesq viscosity assumption may be problematic since the NORSOK Standard C-004 [44] criteria are given as bounds on the standard deviation of the vertical velocity component.

4.5 Standard k - ε (SKE)

The standard k - ε model, abbreviated SKE in this thesis, is based on the transport equations by Jones and Launder [27], with coefficients from Launder and Sharma [31]¹. The transport equations for the turbulence energy and the dissipation rate are modeled as follows in STAR-CCM+ [7, p. 3335].

$$\frac{\partial}{\partial t}(\rho k) + \frac{\partial}{\partial x_j}(\rho k \bar{u}_j) = \frac{\partial}{\partial x_j} \left(\left(\mu + \frac{\mu_t}{\sigma_k} \right) \frac{\partial k}{\partial x_j} \right) + \rho P_k - \rho((\varepsilon - \varepsilon_0) + \Upsilon) \quad (4.18)$$

$$\frac{\partial}{\partial t}(\rho \varepsilon) + \frac{\partial}{\partial x_j}(\rho \varepsilon \bar{u}_j) = \frac{\partial}{\partial x_j} \left(\left(\mu + \frac{\mu_t}{\sigma_\varepsilon} \right) \frac{\partial \varepsilon}{\partial x_j} \right) + \frac{\rho}{T} (C_{\varepsilon 1} P_k - C_{\varepsilon 2} (\varepsilon - \varepsilon_0)) \quad (4.19)$$

ε_0 is a source term that counteracts turbulence decay [7, p. 3335] [60]. According to the STAR-CCM+ support service, the value for this term is taken as the average of ε at the inlet.

P_k is the production rate of turbulence energy. This term may be modeled directly from Eq. (3.11) by inserting the Boussinesq turbulence viscosity assumption, Eq. (4.16). The modulus of the mean rate of strain formulation is used in STAR-CCM+ [7, p. 3336].

$$P_k = \nu_t S^2 - \frac{2}{3} \left(k + \nu_t \frac{\partial \bar{u}_l}{\partial x_l} \right) \frac{\partial \bar{u}_l}{\partial x_l} \quad (4.20)$$

Where S is the modulus of the mean rate of strain.

$$S = \sqrt{2 \bar{S}_{ij} \bar{S}_{ij}} \quad (4.21)$$

The turbulence viscosity is calculated as follows.

$$\mu_t = \rho C_\mu k T \quad (4.22)$$

In the original formulation by Jones and Launder [27], the turbulence timescale, T , is taken as k/ε . To avoid the turbulence timescale to become smaller than the Kolmogorov scale, a minimum constraint is implemented in STAR-CCM+. This constraint was suggested by Durbin [14] to avoid unphysical turbulence timescales close to walls where k goes to zero while ε is non-zero.

$$T = \max \left[\frac{k}{\varepsilon}, \sqrt{\frac{\nu}{\varepsilon}} \right] \quad (4.23)$$

The coefficients in the SKE model are given in Table 4.4.

¹The coefficients in the SKE model may also be cited to Launder and Spalding [32], but the citation is to Launder and Sharma [31] in the STAR-CCM+ documentation [7, p. 3295].

Table 4.4: Coefficients in the SKE model in STAR-CCM+, adopted from Launder and Sharma [31].

$C_{\varepsilon 1}$	$C_{\varepsilon 2}$	C_{μ}	σ_k	σ_{ε}
1.44	1.92	0.09	1.0	1.3

4.5.1 Atmospheric coefficients (SKE-A)

As will be further explained in Section 7.1, the SKE model is also used with a set of coefficients given by Duynkerke [16], which satisfy atmospheric boundary layer conditions. These coefficients are given in Table 4.5. When these coefficients are used, the model is abbreviated SKE-A (atmospheric).

Table 4.5: Coefficients by Duynkerke [16] for the SKE-A model.

$C_{\varepsilon 1}$	$C_{\varepsilon 2}$	C_{μ}	σ_k	σ_{ε}
1.46	1.83	0.033	1.0	2.38

4.5.2 Realizability constraint (SKE-D and SKE-P)

This section presents the SKE model with a maximum constraint on the turbulence timescale. The transport equations, coefficients and relations are exactly as for the SKE model, except for a new formulation for the turbulence timescale, T .

Durbin [15] found that many of his simulations gave a large turbulence timescale when approaching stagnation points. He therefore proposed a maximum constraint on the turbulence timescale, that would counteract the stagnation point anomaly – a term used for this phenomena where an excessive production of turbulence energy in stagnation regions occurs – of turbulence energy transport models. The explanation for the stagnation point anomaly is that the Boussinesq turbulence viscosity assumption gives an erroneous normal stress difference [15]. The normal Reynolds stress components can become negative, even though this is not physically possible, not realizable.

A maximum constraint on the turbulence timescale may be derived by writing the mean rate of strain in principle axes coordinates, in order to become purely diagonal. The eigenvalues, λ_1 , λ_2 , λ_3 , are the diagonal entries themselves, which fulfill [48]:

$$\lambda_1^2 + \lambda_2^2 + \lambda_3^2 = \frac{1}{2}S^2 \quad (4.24)$$

Where S is the modulus of the mean rate of strain, Eq. (4.21). Assuming constant density, the Reynolds-averaged continuity equation, Eq. (3.8), gives:

$$\lambda_1 + \lambda_2 + \lambda_3 = \overline{S_{ii}} = 0 \quad (4.25)$$

As is illustrated by Park and Park [48], Eqs. (4.24) and (4.25) may be thought of as a sphere of radius $\frac{1}{\sqrt{2}}S$, centered at the origin, and a plane passing through the origin of the coordinate system, respectively. The intersection of these two is a circle of radius $\frac{1}{\sqrt{2}}S$, centered at the origin. The maximum eigenvalue, $\max \lambda_\alpha$, fulfills the following requirement [48].

$$\sqrt{\frac{1}{12}}S \leq \max \lambda_\alpha \leq \sqrt{\frac{1}{3}}S \quad (4.26)$$

The variance of a velocity component for constant density flows and in principle axes coordinate system, is found from the Boussinesq turbulence viscosity assumption, Eq. (4.16).

$$\overline{u'_\alpha u'_\alpha} = -2\nu_t \lambda_\alpha + \frac{2}{3}k \quad (4.27)$$

Inserting the expression for the turbulence viscosity, Eq. (4.22), gives.

$$\overline{u'_\alpha u'_\alpha} = -2C_\mu k T \lambda_\alpha + \frac{2}{3}k \quad (4.28)$$

All variances should be larger or equal to zero. The largest eigenvalue gives the smallest variance, and thus:

$$0 \leq -2C_\mu k T \max \lambda_\alpha + \frac{2}{3}k \quad (4.29)$$

Which gives the following constraint for the turbulence timescale.

$$T \leq \frac{1}{3C_\mu \max \lambda_\alpha} \quad (4.30)$$

The most conservative constraint is found by using the smallest maximum value from Eq. (4.26).

$$T \leq \frac{2}{\sqrt{3}C_\mu S} \quad (4.31)$$

According to Pope [50, p. 397], this is the necessary condition for realizability with the standard k - ε model. A sufficient constraint is found by use of the largest maximum value from Eq. (4.26).

$$T \leq \frac{1}{\sqrt{3}C_\mu S} \quad (4.32)$$

The expression may be written with a tuning constant, C_T .

$$T \leq \frac{C_T}{\sqrt{3}C_\mu S} \quad (4.33)$$

Equation (4.32) is the expression for the turbulence timescale given by Durbin [15]. In a later paper, Medic and Durbin [39] tuned the constraint by use of $C_T = 0.6$ which is standard in STAR-CCM+. Simulations with this value are abbreviated SKE-D (Durbin) in this thesis.

Simulations are also run with the necessary condition $C_T = 2$. These simulations are abbreviated SKE-P (Park), where the reference is to Park and Park [48]. This model is more conservative in the sense that it will use the standard formulation for the turbulence timescale more often than the SKE-D model.

In the SKE-D and SKE-P models, the turbulence timescale is calculated as follows¹.

$$T = \min \left[\max \left[\frac{k}{\varepsilon}, \sqrt{\frac{\nu}{\varepsilon}} \right], \frac{C_T}{\sqrt{3}C_\mu S} \right] \quad (4.34)$$

The rest of the equations are the same as in the SKE model with the coefficients from Table 4.4.

4.6 Realizable k - ε (RKE)

The realizable k - ε model, abbreviated the RKE model in this thesis, is an alternative k - ε formulation that uses the same turbulence viscosity assumption as the SKE model, Eq. (4.16), but another transport equation for the dissipation rate, and other values for the coefficients. According to the STAR-CCM+ documentation, the RKE model is substantially better than the SKE model for many applications [7, p. 3304]. The RKE model is therefore recommended over the SKE model, and chosen if the auto-select option is used to select a k - ε turbulence model in STAR-CCM+. As with the models presented in Section 4.5.2, the term realizable indicates that this model guarantees that the normal components of the Reynolds stress tensor are physically correct. The realizability constraint is not imposed on the turbulence timescale, but instead by using a variable C_μ formulation.

The RKE model in STAR-CCM+ is based on the suggestions by Shih et al. [57], but with some modifications. The transport equation for the turbulence energy is the same as in the SKE model, and the production rate of turbulence energy is equally calculated, see Eqs. (4.18) and (4.20). The transport equation for the

¹The STAR-CCM+ documentation contains a typing error in the turbulence timescale formulation. According to the STAR-CCM+ support service, this is an error in the documentation only, and the correct expression is the one presented in Eq. (4.34)

dissipation rate is modeled as follows.

$$\frac{\partial}{\partial t}(\rho\varepsilon) + \frac{\partial}{\partial x_j}(\rho\varepsilon\bar{u}_j) = \frac{\partial}{\partial x_j} \left(\left(\mu + \frac{\mu_t}{\sigma_\varepsilon} \right) \frac{\partial \varepsilon}{\partial x_j} \right) + \rho C_{\varepsilon 1} S \varepsilon - \rho C_{\varepsilon 2} \frac{\varepsilon}{k + \sqrt{\nu \varepsilon}} (\varepsilon - \varepsilon_0) \quad (4.35)$$

The turbulence viscosity is calculated as in the original k - ε formulation by Jones and Launder [27], without constraints on the turbulence timescale.

$$\mu_t = \rho C_\mu \frac{k^2}{\varepsilon} \quad (4.36)$$

The coefficient C_μ is a function of mean rate of deformations, \bar{S}_{ij} and $\bar{\Omega}_{ij}$, and turbulence quantities, k and ε , in order to avoid negative values for the normal Reynolds stress components.

$$C_\mu = \frac{1}{A_0 + A_s U^{(*)} \frac{k}{\varepsilon}} \quad (4.37)$$

$$U^{(*)} = \sqrt{\bar{S}_{ij}\bar{S}_{ij} - \bar{\Omega}_{ij}\bar{\Omega}_{ij}} \quad (4.38a)$$

$$A_s = \sqrt{6} \cos \left(\frac{1}{3} \arccos(\sqrt{6}W) \right) \quad (4.38b)$$

$$W = \frac{\bar{S}_{ij}\bar{S}_{jk}\bar{S}_{ki}}{\sqrt{\bar{S}_{ij}\bar{S}_{ij}}^3} \quad (4.38c)$$

$$A_0 = 4.0 \quad (4.38d)$$

The coefficient $C_{\varepsilon 1}$ is a variable in the RKE model.

$$C_{\varepsilon 1} = \max \left[0.43, \frac{\frac{Sk}{\varepsilon}}{5 + \frac{Sk}{\varepsilon}} \right] \quad (4.39)$$

The rest of the coefficients are given in Table 4.6

Table 4.6: RKE model coefficients in STAR-CCM+, adopted from Shih et al. [57].

$C_{\varepsilon 2}$	σ_k	σ_ε
1.9	1.0	1.2

4.7 Shear stress transport (SST)

The turbulence energy transport models presented this far solve one transport equation for the turbulence energy and one for the dissipation rate. The shear stress transport model, abbreviated SST in this thesis, is a model based on a k - ω formulation. In spite of the name, there is no transport equation for shear stresses in this model. Instead, the model solves one transport equation for the turbulence energy and one transport equation for the specific dissipation rate, defined in Eq. (3.13).

According to the STAR-CCM+ documentation, one benefit of k - ω models over k - ε models is better ability to capture separation [7, p. 3368]. They can also be applied throughout the boundary layer without modifications. However, k - ω models have been known to be far more sensitive to inlet conditions than k - ε based models. The SST model is a newly developed turbulence model based on the k - ω formulation [40]. Compared to the standard k - ω formulation, this model has a cross-diffusion term in the transport equation for ω , which makes the model behave like a k - ε model [7, p. 3368]. The SST model includes blending functions with functions of wall distance, in order to use the cross-diffusion term far from walls, but not near walls. The model may therefore be seen as a combination of a k - ω and a k - ε model, with the attempt to combine benefits of the k - ω and k - ε models.

The two transport equations used in the SST model are as follows [7, p. 3395].

$$\frac{\partial}{\partial t}(\rho k) + \frac{\partial}{\partial x_j}(\rho k \bar{u}_j) = \frac{\partial}{\partial x_j} \left((\mu + \sigma_k \mu_t) \frac{\partial k}{\partial x_j} \right) + \rho P_k - \rho \beta^* (\omega k - \omega_0 k_0) \quad (4.40)$$

$$\frac{\partial}{\partial t}(\rho \omega) + \frac{\partial}{\partial x_j}(\rho \omega \bar{u}_j) = \frac{\partial}{\partial x_j} \left((\mu + \sigma_\omega \mu_t) \frac{\partial \omega}{\partial x_j} \right) + \rho P_\omega - \rho \beta (\omega^2 - \omega_0^2) + \rho D_\omega \quad (4.41)$$

Analogous to the k - ε models, k_0 and ω_0 are source terms that are added to counteract turbulence decay [7, p. 3395] [60]. Their values are taken as the averaged value of k and ω at the inlet.

The production rate of turbulence energy is calculated in the same way as for the SKE model, Eq. (4.20). The production rate of the specific dissipation rate is modeled as follows.

$$P_\omega = \gamma \left(S^2 - \frac{2}{3} \left(\omega + \frac{\partial \bar{u}_i}{\partial x_i} \right) \frac{\partial \bar{u}_i}{\partial x_i} \right) \quad (4.42)$$

The cross-diffusion term, D_ω , in the transport equation for the specific dissipation rate, comes from the transformation of a k - ε model into equations based on k and ω . The term is modeled as follows.

$$D_\omega = 2(1 - F_1) \sigma_\omega \frac{1}{\omega} \frac{\partial k}{\partial x_j} \frac{\partial \omega}{\partial x_j} \quad (4.43)$$

F_1 is the first of two blending functions.

$$F_1 = \tanh(\text{arg}_1^4) \quad (4.44)$$

$$\text{arg}_1 = \min \left[\max \left[\frac{\sqrt{k}}{0.09\omega d}, \frac{500\nu}{d^2\omega} \right], \frac{2k}{d^2CD} \right] \quad (4.45)$$

Where d is the distance to the nearest wall, and CD is related to the cross-diffusion term.

$$CD = \max \left[\frac{1}{\omega} \frac{\partial k}{\partial x_j} \frac{\partial \omega}{\partial x_j}, 10^{-20} \text{ s}^{-2} \right] \quad (4.46)$$

The coefficients in the SST model are calculated from the blending function F_1 , such that a coefficient ϕ is taken as follows.

$$\phi = F_1\phi_1 + (1 - F_1)\phi_2 \quad (4.47)$$

The inner layer (k - ω) coefficients are assigned with index 1 and the outer layer (k - ε) coefficients are assigned with index 2. The last three coefficients, β^* , α^* , and a , are the same in both layers. The coefficients used in STAR-CCM+ are given in Table 4.7.

Table 4.7: Coefficients used in the SST model in STAR-CCM+.

β_1	σ_{k1}	$\sigma_{\omega1}$	γ_1	β_2	σ_{k2}	$\sigma_{\omega2}$	γ_2	β^*	α^*	a
0.0750	0.85	0.5	0.055	0.0828	1.0	0.856	0.44	0.09	1	0.31

The turbulence viscosity is calculated with Durbin's realizability constraint as standard. As mentioned in Section 4.5.2, this constraint limits the turbulence timescale, which counteracts the stagnation point anomaly. Consequently, the SST model is a realizable model. Only the standard value in STAR-CCM+, $C_T = 0.6$, is used for the SST model in this thesis.

$$\mu_t = \rho k T \quad (4.48)$$

$$T = \min \left[\frac{1}{\max \left[\frac{\omega}{\alpha^*}, \frac{SF_2}{a} \right]}, \frac{C_T}{\sqrt{3}S} \right] \quad (4.49)$$

F_2 is the second blending function.

$$F_2 = \tanh(\text{arg}_2^2) \quad (4.50)$$

$$\text{arg}_2 = \max \left[\frac{2\sqrt{k}}{\beta^*\omega d}, \frac{500\nu}{d^2\omega} \right] \quad (4.51)$$

The origin of the SST model name lies in the new formulation for the turbulence viscosity. Although the original formulation of the SST model did not include Durbin's realizability constraint, the outer limit, the inner limit reduces the shear stress in adverse pressure gradients [12, p. 136]. The original formulation was based on the rate of rotation instead of the rate of strain in Eq. (4.49), but the present formulation is known to extend the model's applicability [7, p. 3396].

4.8 Cubic k - ε (CKE)

The cubic k - ε model, abbreviated CKE in this thesis, is based on the SKE model, but unlike the other turbulence energy transport models in this thesis, the CKE model does not use the Boussinesq viscosity assumption. Instead, the model uses a nonlinear constitutive relation proposed by Lien et al. [35]. The nonlinear constitutive relation can be thought of as an extension to the Boussinesq turbulence viscosity assumption, or as a simplification of a Reynolds stress transport model [3].

The Boussinesq turbulence viscosity assumption is known to fail in a number of flow situations [50, pp. 359–365]. One of the main deficiencies is the lack of capability to return the correct anisotropy between the normal stress components, which is the reason NORSOK Standard C-004 requires the use of Reynolds stress transport models in helideck simulations. To better represent anisotropic flow phenomena, a nonlinear constitutive relation can be applied [7, p. 3322]. Quadratic terms in the constitutive relation is known to better represent normal-stress anisotropy, while cubic terms makes the model capable of capturing curvature strain [3].

The constitutive relation in the CKE model is given in Eq. (4.52). The first line is the exact linear constitutive relation, Eq. (4.16). The following three lines represent quadratic extensions, while the last two lines are cubic extensions.

$$\begin{aligned}
 -\overline{\rho u'_i u'_j} &= 2\mu_t \overline{S}_{ij} - \frac{2}{3} \left(\mu_t \frac{\partial \overline{u}_l}{\partial x_l} + \rho k \right) \delta_{ij} \\
 &- 4C_{C1} \mu_t \frac{k}{\varepsilon} \left(\overline{S}_{ik} \overline{S}_{jk} - \frac{1}{3} \overline{S}_{kl} \overline{S}_{kl} \delta_{ij} \right) \\
 &- 4C_{C2} \mu_t \frac{k}{\varepsilon} \left(\overline{S}_{ik} \overline{\Omega}_{jk} + \overline{S}_{jk} \overline{\Omega}_{ik} \right) \\
 &- 4C_{C3} \mu_t \frac{k}{\varepsilon} \left(\overline{\Omega}_{ik} \overline{\Omega}_{jk} - \frac{1}{3} \overline{\Omega}_{kl} \overline{\Omega}_{kl} \delta_{ij} \right) \\
 &- 8C_{C4} \mu_t \frac{k^2}{\varepsilon^2} \left(\overline{S}_{ik} \overline{\Omega}_{jl} + \overline{S}_{jk} \overline{\Omega}_{il} \right) \overline{S}_{kl} \\
 &- 8C_{C5} \mu_t \frac{k^2}{\varepsilon^2} \left(\overline{S}_{kl} \overline{S}_{kl} \overline{S}_{ij} - \overline{\Omega}_{kl} \overline{\Omega}_{kl} \overline{S}_{ij} \right)
 \end{aligned} \tag{4.52}$$

The coefficients $C_{C1} - C_{C5}$ are given as follows.

$$C_{C1} = \frac{C_{NL1}}{\left(C_{NL4} + \left(\frac{k}{\varepsilon}S\right)^3\right) C_{\mu}} \quad (4.53a)$$

$$C_{C2} = \frac{C_{NL2}}{\left(C_{NL4} + \left(\frac{k}{\varepsilon}S\right)^3\right) C_{\mu}} \quad (4.53b)$$

$$C_{C3} = \frac{C_{NL3}}{\left(C_{NL4} + \left(\frac{k}{\varepsilon}S\right)^3\right) C_{\mu}} \quad (4.53c)$$

$$C_{C4} = C_{NL5}C_{\mu}^2 \quad (4.53d)$$

$$C_{C5} = C_{NL6}C_{\mu}^2 \quad (4.53e)$$

The CKE model is based on a variable C_{μ} formulation. This variable C_{μ} formulation is intended to reduce the excessive turbulence generation at stagnation points [3]. The formulation is however not realizable¹.

$$C_{\mu} = \frac{C_{a0}}{C_{a1} + C_{a2}S + C_{a3}\frac{k}{\varepsilon}\Omega} \quad (4.54)$$

The modulus of the mean rate of rotation, Ω , is defined analogous to the modulus of the mean rate of strain, Eq. (4.21).

$$\Omega = \sqrt{2\overline{\Omega_{ij}}\overline{\Omega_{ij}}} \quad (4.55)$$

The transport equations in the CKE model are the same as in the SKE model, Eqs. (4.18) and (4.19), but an addition term for the production rate of turbulence energy is included due to the nonlinear constitutive relation. The nonlinear production rate of turbulence energy is found by subtracting the linear constitutive relation, Eq. (4.16), from the cubic constitutive relation, Eq. (4.52), and multiplying with the velocity gradient [7, p. 3336].

Table 4.8: Additional coefficients in the CKE model, adopted from Lien et al. [35].

C_{NL1}	C_{NL2}	C_{NL3}	C_{NL4}	C_{NL5}	C_{NL6}	C_{a0}	C_{a1}	C_{a2}	C_{a3}
0.75	3.75	4.75	1000	-10	-2	0.667	1.25	1	0.9

¹The CKE model calculated negative values for the variance of the vertical velocity component for some wind headings in the helideck simulations.

The coefficients in the transport equations are the same as in the SKE model, except for the variable C_μ formulation. The additional coefficients in the constitutive relation and variable C_μ formulation, are given in Table 4.8.

5 Numerical approach

This section presents a brief introduction to some of the numerical approaches that are used in this thesis. Focus is on the finite volume method and discretization, solvers and linkage of transport equations, mesh generation, and boundary types and conditions. The assumptions and formulations for the wall functions of the tested turbulence models, are also given in this section. Derivation of wall functions may be considered part of turbulence modeling, Section 4, but are presented together with other boundary types and conditions in this section.

STAR-CCM+ is a commercial CFD package that includes tools for all three steps of a CFD analysis, pre-processing, processing solution, and post-processing. This package was used to simulate dispersion of CO₂ in the author's specialization project [41]. Having developed some experience with STAR-CCM+, the package was chosen for this thesis as well. STAR-CCM+ v.8.06, which was released in October 2013, is used for the simulations in this thesis.

Apart from having a closed source code, one of the main drawbacks with a commercial CFD package is the license fee. However, STAR-CCM+ offers an academic licensing program which makes it possible for students to use the software free of charge. Alternatively, KFX or OpenFOAM could have been used for the simulations in this thesis, but were not chosen due to lack of implemented turbulence models and the author's lack of experience, respectively.

5.1 Finite volume method

STAR-CCM+ is a finite volume method based CFD package. The term finite volume refers to the division of the spatial domain into control volumes of finite size [33, p. 231], corresponding to the cells of the meshed geometry [7, p. 5657]. The finite volume method starts with integration of the governing transport equations on such a control volume [71, p. 115]. The divergence theorem is used to convert divergence terms to surface integrals. These terms are then evaluated as fluxes at the faces of each control volume, which enables the finite volume method to be conservative [71, p. 142].

The integrated transport equation for a general transported scalar quantity ϕ may

be written as follows [7, p. 5657].

$$\frac{d}{dt} \left(\int_V \rho \phi \, dV \right) + \int_A (\rho \phi \mathbf{u}) \, dA = \int_A (\Gamma \nabla \phi) \, dA + \int_V S_\phi \, dV \quad (5.1)$$

The four terms of Eq. (5.1) are, from left to right, the transient term, the convective term, the diffusive term and the volumetric source term [7, p. 5657]. A discrete form of Eq. (5.1), for the cell with node point 0 and faces f against adjacent cells, may be written as follows [7, p. 5657].

$$\frac{d}{dt} (\rho \phi V)_0 + \sum_f [\rho \phi \mathbf{u} \cdot \mathbf{a}]_f = \sum_f [\Gamma \nabla \phi \cdot \mathbf{a}]_f + (S_\phi V)_0 \quad (5.2)$$

As can be seen in Eq. (5.2), the transient and source terms are evaluated inside the cell, while the convective and diffusive fluxes are evaluated at the faces of the cell.

5.1.1 Transient term

The transient term is zero and needs no further evaluation since a steady state solver is used for all simulations in this thesis [7, p. 5658].

$$\frac{d}{dt} (\rho \phi V)_0 = 0 \quad (5.3)$$

5.1.2 Convective term

The convective term at a face is discretized as follows [7, p. 5659].

$$[\rho \phi \mathbf{u} \cdot \mathbf{a}]_f = (\dot{m} \phi)_f = \dot{m}_f \phi_f \quad (5.4)$$

Where $(\dot{m} \phi)_f$ is the convective flux at the face, with \dot{m}_f being the mass flow rate at the face of cell 0, while ϕ_f is the value of the transported quantity at the face of cell 0. The way ϕ_f is calculated at the face is crucial for stability and accuracy. A second-order upwind scheme, which is standard in STAR-CCM+, is used in this thesis.

An upwind scheme calculates the face values based on upstream information. The calculation is therefore dependent on the flow direction.

$$\dot{m}_f \phi_f = \begin{cases} \dot{m}_f \phi_{f,0} & \text{for } \dot{m}_f \geq 0. \\ \dot{m}_f \phi_{f,1} & \text{for } \dot{m}_f < 0. \end{cases} \quad (5.5)$$

The face values, $\phi_{f,0}$ and $\phi_{f,1}$, are linearly interpolated from the cell values on either side of the face.

$$\phi_{f,0} = \phi_0 + \mathbf{s}_0 \cdot (\nabla \phi_0) \quad (5.6a)$$

$$\phi_{f,1} = \phi_1 + \mathbf{s}_1 \cdot (\nabla \phi_1) \quad (5.6b)$$

Where \mathbf{s} is the vector between the face and the cell centroid.

$$\mathbf{s}_0 = \mathbf{x}_f - \mathbf{x}_0 \quad (5.7a)$$

$$\mathbf{s}_1 = \mathbf{x}_f - \mathbf{x}_1 \quad (5.7b)$$

The gradients of the transported quantities, $\nabla \phi$, are solved by use of a hybrid scheme which blends the Gauss method with a weighted least squares method [7, p. 5671].

In the surface-mounted cube case, which will be presented in Section 6.3, convergence issues were found with some of the turbulence models. A first-order upwind scheme was therefore used in the Reynolds-averaged momentum equation to generate converged solutions. Upwind schemes has a diffusion-like error that is stabilizing and leads to robust convergence [7, p. 5660]. Decreasing the order of the scheme increases the error. The first-order method is therefore only used in the surface-mounted cube case for the models that did not converge. With the first-order upwind scheme, the convective flux is simply based on the upstream cell, without interpolation between the cells on either side of the face [7, p. 5659].

$$\dot{m}_f \phi_f = \begin{cases} \dot{m}_f \phi_0 & \text{for } \dot{m}_f \geq 0. \\ \dot{m}_f \phi_1 & \text{for } \dot{m}_f < 0. \end{cases} \quad (5.8)$$

5.1.3 Diffusive term

The diffusive term in Eq. (5.2) consists of the diffusivity, Γ , gradient, $\nabla \phi$, and area vector, \mathbf{a} . A second-order accurate scheme is used for the face gradient [7, p. 5664].

$$\nabla \phi_f = (\phi_1 - \phi_0) \alpha + (\nabla \phi)_a - ((\nabla \phi)_a \cdot \mathbf{ds}) \alpha \quad (5.9)$$

Where α , \mathbf{ds} , and $(\nabla \phi)_a$ are taken as follows.

$$\alpha = \frac{\mathbf{a}}{\mathbf{a} \cdot \mathbf{ds}} \quad (5.10a)$$

$$\mathbf{ds} = \mathbf{x}_1 - \mathbf{x}_0 \quad (5.10b)$$

$$(\nabla \phi)_a = \frac{\nabla \phi_0 + \nabla \phi_1}{2} \quad (5.10c)$$

Where \mathbf{x}_1 and \mathbf{x}_0 are the coordinates of the cells on either side of the face. A harmonic average, based on the adjacent cells, is typically used for the approximation

of the face diffusivity, Γ_f [7, p. 5664]. The diffusion term is then expressed as follows [7, p. 5664].

$$\Gamma_f \nabla \phi_f \cdot \mathbf{a} = \Gamma_f ((\phi_1 - \phi_0) \alpha \cdot \mathbf{a} + (\nabla \phi)_a \cdot \mathbf{a} - ((\nabla \phi)_a \cdot \mathbf{ds}) \alpha \cdot \mathbf{a}) \quad (5.11)$$

5.1.4 Volumetric source term

The volumetric source term of Eq. (5.1) is evaluated at the cell centroid in Eq. (5.2).

$$\int_V S_\phi dV = (S_\phi V)_0 \quad (5.12)$$

This expression for the source term is the simplest formulation that is consistent with second-order discretization [7, p. 5659].

5.2 Mesh tools

The discretized transport equations, represented by Eq. (5.2), are applied to all finite volumes, cells, in the domain. The process of dividing the domain into finite volumes is referred to as meshing in STAR-CCM+. Three mesh tools are used in the present simulations. The *Trimmed mesher* is used for all simulations, the *Surface remesher* is used for the three-dimensional simulations, while the *Prism layer mesher* is used only in the helideck simulations. A short presentation of these tools are given in this section, while details on cell sizes and prism layers are given in the simulation setup sections.

The trimmed mesher is the corner stone of all meshes in this thesis. Based on the surfaces of the geometries made with the STAR-CCM+ *3D-CAD model* tool, the trimmed mesher creates a predominantly hexahedral mesh with minimal cell skewness [7, p. 1963]. The geometries in the validation and verification simulations, to be presented in Section 6, are simple enough to provide a mesh where all cells are regular hexahedrons. Consequently, the two-dimensional cases consist of square cells, while the three-dimensional case consists of cubical cells. Most of the cells in the helideck simulations are regular hexahedrons as well, but some cells have other shapes due to more complex geometries on the rig.

The trimmed mesher makes the mesh based on the surfaces from the CAD model. The surface remesher is used to improve the overall quality of an existing surface and optimize it for the volume mesher [7, p. 1910], that is, the trimmed mesher in this thesis. The surface remesher is used with its standard values in the present simulations.

In addition to the trimmed mesher and the surface remesher, the prism layer mesher is used to generate orthogonal prismatic cells next to the wall boundaries, the ocean and the rig, in the helideck simulations. This layer improves the accuracy of the calculations [7, p. 1985]. The cells are gradually decreased close to walls, which

increases the mesh resolution and makes the near-wall distance suitable for use with wall functions, to be explained in Section 5.4.4.

Volumetric controls are used in the three-dimensional simulations of this thesis. The purpose of volumetric controls is to specify the mesh density in a specific zone of the domain [7, p. 1836]. This enables the use of smaller cells in regions of particular interest, for instance close to the rig and helideck in the helideck simulations. Cells outside the volumetric controls are typically made bigger to enable the use of large domains without extensive computational costs. To ensure smooth transitions between volumetric control regions of different cell sizes, the growth rate can be adjusted in the STAR-CCM+ mesh properties. A slow growth rate is used in the surface-mounted cube case and in the helideck simulations, which produces a minimum of four transition cells between different cell sizes [7, p. 1974].

The meshing process in STAR-CCM+ is three-dimensional. The geometries of the two-dimensional validation and verification simulations are made three-dimensional by adding a small distance in the lateral direction. The trimmed mesher is then used to generate the mesh. Finally, the mesh is made two-dimensional by use of the *Convert to 2D* tool.

5.3 Segregated flow solver

The segregated flow solver has been used for all simulations in this thesis. A coupled flow solver is also available in STAR-CCM+, but the segregated solver is faster and suitable for incompressible or mildly compressible flows [7, p. 2698]. The segregated flow solver is used with an isothermal energy assumption in the helideck simulations. This means that the temperature is set to a constant value in the domain and the energy equation is not needed. An equation of state is used to calculate the density in STAR-CCM+. The ideal gas law is used to express density as a function of the calculated pressure in the helideck simulations. The three test cases, to be presented in Section 6, are simulated with a constant density model.

The Reynolds-averaged continuity and momentum equations are discretized as described in Section 5.1, and solved in a segregated manner. Linkage between the Reynolds-averaged continuity and momentum equations is achieved with the SIMPLE algorithm. The SIMPLE algorithm is an iterative predictor-corrector method, which solves a simplified version of the Reynolds-averaged momentum equation with a guessed (initial for the first iteration) value for the pressure, and then uses the Reynolds-averaged continuity equation as a pressure corrector [71, pp. 186–190].

5.4 Boundary conditions

The boundaries of the calculation domain are set to specific boundary types in STAR-CCM+. Four boundary types are used in the simulations of this thesis -

velocity inlet, pressure outlet, symmetry plane, and wall. Details on the boundary types are given in the following sections.

5.4.1 Velocity inlet

The velocity inlet boundary type is used at the inlets of all simulations in this thesis. This boundary type is used on the top boundary of the helideck simulations as well, in order to specify fixed values for velocity and turbulence quantities. The face velocity is specified directly with components. This makes it possible to have a boundary-normal flow direction on the inlet boundary, and a boundary-parallel flow direction on the sky boundary, that is, no inflow from the top boundary. The face boundary pressure is extrapolated from the adjacent cell using reconstruction gradients [7, p. 2923]. For the Reynolds stress transport models, boundary values for the six Reynolds stress components and the dissipation rate are specified with inlet values directly, while the turbulence energy transport models are specified with the turbulence energy and (specific) dissipation rate.

5.4.2 Pressure outlet

The pressure outlet boundary type is used at the outlets of all simulations in this thesis. The velocity is specified by extrapolation from the interior using reconstruction gradients. The pressure is set equal to the reference pressure [7, p. 2926]. This means that the outlet should be placed far downstream of any obstacle that may influence the pressure, in order to ensure that the solution is not influenced by the pressure specification at the outlet. The turbulence quantities are extrapolated from the interior, but need to be specified in case of back-flow. No back-flow were found with any simulation, and the standard turbulence values were kept unchanged.

5.4.3 Symmetry plane

The face-normal velocity is zero at the symmetry plane boundary, while the parallel components are extrapolated from the adjacent cell using reconstruction gradients [7, p. 5671]. The pressure and turbulence quantities are also found by extrapolation from the adjacent cell.

5.4.4 Wall treatment

The velocities at the wall are set equal to the wall motion (zero) from the no-slip condition. The pressure is found by extrapolation from the adjacent cell. All turbulence models in this thesis use wall functions to determine boundary conditions

for wall boundaries. The formulations are based on dimensionless quantities for the wall distance normal to the wall and velocity in the streamwise direction.

$$z^+ = \frac{z u_*}{\nu} \quad (5.13a)$$

$$u^+ = \frac{\bar{u}}{u_*} \quad (5.13b)$$

These quantities are given as functions of the kinematic viscosity and friction velocity which is defined as follows.

$$u_* = \sqrt{\frac{\tau_w}{\rho}} \quad (5.14)$$

Where τ_w is the shear stress at the wall.

Presented in Fig. 5.1 are the turbulence energy budget and velocity profile as functions of the dimensionless wall-normal coordinate¹ from DNS of a boundary layer [55]. The velocity profile is approximately logarithmic for $30 \leq z^+ \leq 500$ -1000 [5]. In the same region, the turbulence production and dissipation dominate the turbulence energy budget, while shear produced by turbulence is dominating over viscous shear. These three observations are the basis for defining wall functions.

$$u^+ = \frac{1}{\kappa} \ln z^+ + D \quad (5.15)$$

$$P_k \approx \varepsilon \quad (5.16)$$

$$\tau_{turbulence} \gg \tau_{molecular} \quad (5.17)$$

By neglecting viscous shear, the shear stress at the wall is given from the Reynolds shear stress alone.

$$\tau_w \approx -\rho \overline{u'w'} \quad (5.18)$$

The turbulence viscosity is found from the Boussinesq viscosity assumption, Eq. (4.16).

$$-\rho \overline{u'w'} = \mu_t \frac{\partial \bar{u}}{\partial z} \quad (5.19)$$

By use of the logarithmic velocity profile assumption, and the definition for the friction velocity, the turbulence viscosity may be written as follows.

$$\mu_t = \rho \kappa z u_* \quad (5.20)$$

¹Since z is used as the coordinate normal to the helideck in the helideck simulations, z is used instead of y as the wall-normal coordinate here as well. This is also the case for the 2D simulations that will be presented later.

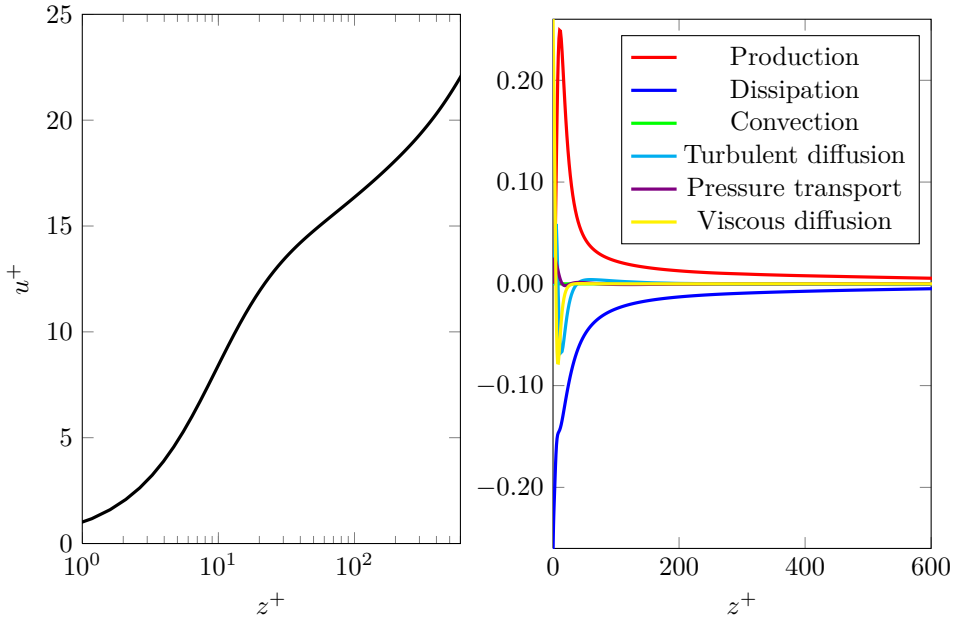


Figure 5.1: Dimensionless velocity profile (left) and turbulence energy budget (right) from DNS of boundary layer flow at $Re_\theta = 4060$ [55].

The production rate of turbulence energy is calculated from Eq. (4.20).

$$P_k = \nu_t 2\overline{S_{ij}}\overline{S_{ij}} = 2\nu_t \left(\frac{1}{4} \left(\frac{\partial \overline{u}}{\partial z} \right)^2 + \frac{1}{4} \left(\frac{\partial \overline{u}}{\partial z} \right)^2 \right) = \nu_t \left(\frac{\partial \overline{u}}{\partial z} \right)^2 \quad (5.21)$$

By use of Eqs. (5.15), (5.13), (5.14) and (5.20), the term may be defined as in the STAR-CCM+ documentation [7, pp. 3351–3352].

$$P_k = \frac{\rho}{\mu} \left(u_* \frac{\overline{u}}{u^+} \right)^2 \frac{\partial u^+}{\partial z^+} \quad (5.22)$$

By assuming that the dissipation rate is equal to the production rate of turbulence energy, it may be written as follows.

$$\varepsilon = \frac{u_*^3}{\kappa z} \quad (5.23)$$

Which gives the following expression for the specific dissipation rate.

$$\omega = \frac{\varepsilon}{k\beta^*} = \frac{u_*}{\sqrt{\beta^*}\kappa z} \quad (5.24)$$

Where the original formulation for the turbulence viscosity, without constraints on the turbulence timescale, have been used to derive an expression for the friction velocity.

$$u_* = C_\mu^{\frac{1}{4}} k^{\frac{1}{2}} \quad (5.25a)$$

$$u_* = \beta^*{}^{\frac{1}{4}} k^{\frac{1}{2}} \quad (5.25b)$$

The k - ε models used in this thesis, calculate the production, dissipation, and friction velocity from Eqs. (5.22), (5.23) and (5.25a), respectively [7, pp. 3351–3352]. The SST model is based on the specific dissipation rate and β^* , and uses Eqs. (5.22), (5.24) and (5.25b) for production, specific dissipation, and friction velocity, respectively [7, pp. 3401–3402]. Like the k - ε models, the Reynolds stress transport models use Eqs. (5.22), (5.23), and (5.25a) [7, pp. 3424, 3433–3435]. In addition, these models need specification of the Reynolds stress tensor. A method developed by Hadzic [22] is used in STAR-CCM+. The wall-normal velocity gradient is found from Eq. (5.15), while all other velocity gradients are neglected. The wall-normal coordinate system is then transformed to a Cartesian coordinate system and are together with the Reynolds stresses used to calculate the production terms in the Reynolds stress transport equations [22, p. 76]. Following this method, the set of wall functions for the Reynolds stress transport models are applicable also in non-equilibrium flows [22].

6 Validation and verification simulations

Validation and verification are two concepts that are used to quantify the level of confidence in CFD analyses [71, p. 293]. The definition of the two terms may be simplified to “solving the right equations” and “solving the equations right”, for validation and verification respectively [53]. A typical validation exercise could be to compare a model with experiments or DNS. Verification of a model could involve a comparison with other implementations and simulations of the same model.

To investigate the Reynolds stress transport model implementations in STAR-CCM+, a fully developed channel flow has been simulated and compared with simulations by Klein [29]. The verification exercise, which is based on a comparison of different Reynolds stress components, is done for the Reynolds stress transport models only. In addition, a comparison with the DNS by Abe et al. [1] is done for all models. Plots of the turbulence energy, vertical Reynolds stress component, and mean streamwise velocity profiles are used to evaluate the performance of the different turbulence models. The fully developed channel flow is presented in Section 6.1.

In addition to the fully developed channel flow, the models are tested and compared with experimental data by Driver and Seegmiller [13] for a backward-facing step case, presented in Section 6.2. This case is the simplest known test case that contains both separation and reattachment, and therefore an ideal test case for turbulence models [30]. A three-dimensional case, presented in Section 6.3, is simulated as well. This case is known as the surface-mounted cube case, studied experimentally by Martinuzzi and Tropea [38].

The validation and verification simulations may provide knowledge on the modeling errors and differences between the turbulence models, which can be useful for assessing the models in the helideck simulations. It is of particular interest to evaluate the performance differences between the Reynolds stress transport models and the turbulence energy transport models since NORSOK Standard C-004 [44] requires a Reynolds stress transport model for helideck simulations.

Testing of mesh dependence, boundary conditions, and domain size dependence may also be considered part of a validation and verification exercise. These tests for the helideck simulations, are presented in Section 8.1.

6.1 Fully developed channel flow

6.1.1 Case description and setup

The channel flow chosen to be simulated is the one performed by Abe et al. [1], which has been simulated by Klein [29]. The Reynolds number for this case is 1020 based on the channel half height and the friction velocity.

$$Re_* = \frac{\rho u_* \frac{h}{2}}{\mu} = 1020 \quad (6.1)$$

The Reynolds number may be written in terms of the bulk velocity, u_b .

$$Re_b = \frac{\rho u_b h}{\mu} \quad (6.2)$$

Where the bulk velocity is calculated as follows [50, p. 266].

$$u_b = \frac{1}{\frac{h}{2}} \int_0^{\frac{h}{2}} \bar{u} \, dz. \quad (6.3)$$

Abe et al. [1] obtained $Re_b = 41\,441$, but used the friction velocity to define the case setup. Klein [29] did it the other way around, and specified \bar{u} at the inlet. Since the most important purpose of this test case is verification of the Reynolds stress transport models, hence comparing with the simulations done by Klein [29], Re_b has been used here as well.

Klein [29] sets the density, height, and inlet velocity equal to unity in her simulations, and defines the dynamic viscosity from the Reynolds number.

$$\rho = 1 \text{ kg m}^{-3} \quad (6.4)$$

$$h = 1 \text{ m} \quad (6.5)$$

$$\bar{u} = 1 \text{ m s}^{-1} \quad (6.6)$$

Since the inlet velocity is constant, Eq. (6.3) gives $u_b = \bar{u}$ and the dynamic viscosity is the inverse of the bulk Reynolds number.

$$\mu = \frac{\rho h u_b}{Re_b} = \frac{1}{41\,441} \text{ kg m}^{-1} \text{ s}^{-1} \quad (6.7)$$

The present simulations use Eq. (6.4) to specify the density. Since density is specified explicitly, the constant density model is used, instead of the ideal gas model, for simplicity. To define conditions at the inlet, Eqs. (6.5)-(6.7) are used.

Inlet values for turbulence quantities are approximated as follows [29].

$$k = \frac{3}{2}(I\bar{u})^2 \quad (6.8a)$$

$$\overline{u'u'} = k \quad (6.8b)$$

$$\overline{v'v'} = 0.6k \quad (6.8c)$$

$$\overline{w'w'} = 0.4k \quad (6.8d)$$

$$\overline{u'w'} = 0 \quad (6.8e)$$

$$\varepsilon = \frac{C_\mu^{\frac{3}{4}} k^{\frac{3}{2}}}{L} \quad (6.8f)$$

$$\omega = \frac{\varepsilon}{k\beta^*} = \frac{k^{\frac{1}{2}}}{C_\mu^{\frac{1}{4}} L} \quad (6.8g)$$

Where the turbulence intensity and length scale at the inlet, I and L , are set to 6 % [29] and $0.07 h$ respectively [71, p. 77]¹. The constant value from the SKE model, $C_\mu = \beta^* = 0.09$, is used for all models at the inlet. The inlet conditions are therefore the same for all models, except for the specification of the Reynolds stress components, instead of the turbulence energy, in the Reynolds stress transport models, and the specific dissipation rate, instead of the dissipation rate, in the SST model.

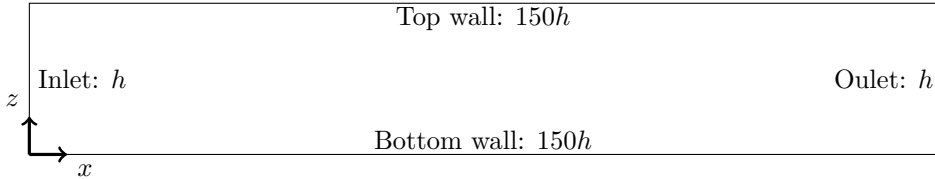


Figure 6.1: Fully developed channel flow domain. The sketch is not drawn to scale.

According to Lien et al. [36], the length of the channel should be 130-150 times the height, h , for the flow to be fully developed. This recommendation is used in the simulations and the domain is therefore $150h$ in the streamwise direction and h in the vertical direction. A simple sketch of the domain is given in Fig. 6.1. The setup is two-dimensional with no-slip wall boundaries on the top and bottom boundaries, a velocity inlet boundary type on the left boundary, and a pressure outlet boundary type on the right boundary. The simple geometry is created with the 3D-CAD model tool, then meshed with the trimmed mesher, and finally converted to a two-dimensional mesh with square cells of lengths Δ . Notice that x and z are used as coordinates for consistency with the helideck simulations,

¹There seems to be a typing error in the expression for the turbulence energy in Versteeg and Malalasekera [71, p. 77]. Equation (6.8a) has been used to define the turbulence energy as a function of turbulence intensity in the present simulation.

that is, the variance of the vertical velocity component is $\overline{w'w'}$ in all simulations of the thesis.

Dimensionless quantities, based on the friction velocity, are used in the presentation of the fully developed channel flow in Figs. 6.2 and 6.3.

$$\overline{u'u'}^+ = \frac{\overline{u'u'}}{u_*^2} \quad \overline{v'v'}^+ = \frac{\overline{v'v'}}{u_*^2} \quad \overline{w'w'}^+ = \frac{\overline{w'w'}}{u_*^2} \quad \overline{u'w'}^+ = \frac{\overline{u'w'}}{u_*^2} \quad (6.9)$$

$$k^+ = \frac{k}{u_*^2} \quad (6.10)$$

$$u^+ = \frac{u}{u_*} \quad (6.11)$$

It is possible to obtain Reynolds stress components for the turbulence energy transport models in STAR-CCM+, but this requires some effort by the user. First, the *Temporary storage retained* option must be ticked on in the *Segregated flow solver* expert properties. The Boussinesq viscosity assumption, Eq. (4.16), can then be implemented as a user field function. The variance of the vertical velocity component, Eq. (4.17), is implemented as a field function, named *ww2D*, as follows.

```
ww2D = 2/3*$TurbulentKineticEnergy
-2*$TurbulentViscosity/$Density*$$V_VelocityGrad [1]
```

Notice that STAR-CCM+ counts the coordinates as 0, 1 and 2. Since this test case is two-dimensional, 1 is used for the vertical direction in STAR-CCM+.

The last term of Eq. (4.17) is not included since a constant density model is used in the simulations. This term is zero from the Reynolds-averaged continuity equation for constant density flows. The second term, the strain rate term, is included, although the term equals zero if the flow is fully developed. The mean lateral velocity gradient is zero from the two-dimensional assumption, and the mean streamwise velocity is independent of the streamwise coordinate since the flow is fully developed. The Reynolds-averaged continuity equation then gives zero vertical velocity dependence on the vertical coordinate, and the variance of the vertical velocity component reduces to $\overline{w'w'} = \frac{2}{3}k$ in Eq. (4.17).

The variance of the vertical velocity component is obtainable without a user field function for the Reynolds stress transport models. For the CKE model, the component is available if the temporary storage retained option is enabled for the *K-Epsilon turbulence solver*.

6.1.2 Results

A simple test of the mesh resolution was done with the QPS model by evaluating the calculated boundary layer thickness, δ_{99} , with decreasing mesh cell base size. The boundary layer thickness was found by linear interpolation of the two cells where

the mean streamwise velocity component was found to equal 99 % of the mean streamwise velocity in the center of the channel. The boundary layer thicknesses, as well as z_{wall}^+ values, for three Δ values are given in Table 6.1. All results presented in this section are taken at $x = 140h$ and compared with the corresponding values at $x = 130h$ to ensure fully developed conditions.

Table 6.1: Mesh refinement test: Boundary layer thickness, δ_{99} , for the QPS model.

Mesh	Δ	Cells	Boundary Layer Thickness	z_{wall}^+
<i>fdc1</i>	0.05 h	60 000	0.146 h	50
<i>fdc2</i>	0.0250 h	240 000	0.175 h	25
<i>fdc3</i>	0.0125 h	960 000	0.172 h	13

A near wall cell distance of $z_{wall}^+ = 13$ may be too short for use with wall functions, although the STAR-CCM+ documentation suggests that wall functions can be used with z_{wall}^+ as low as 12 without significant errors [7, p. 3256]. The deviation in the calculated boundary layer thickness between *fdc2* and *fdc3* is negligible, which suggests that the resolution of the second finest mesh may be sufficient. The finest mesh requires four times as many cells to be calculated, and the second finest mesh is therefore used in the simulations of this test case.

The Reynolds number may be written as a function of the friction velocity or the bulk velocity, Eqs. (6.1) and (6.2). To see how consistent the two Reynolds numbers are, the friction velocity Reynolds number was calculated for each turbulence model. The results are presented in Table 6.2. Ideally, a bulk velocity Reynolds number of $Re_b = 41\,441$ should give $Re_* = 1020$, as was found in the DNS by Abe et al. [1]. Although some deviation is found for all models, the differences compared to the DNS are likely to be insignificant.

Table 6.2: Calculated Reynolds number based on friction velocity, Re_* , with the relative difference from the DNS by Abe et al. [1] of $Re_* = 1020$.

Turbulence model	Re_*	Deviation
LPS	1018	-0.2 %
QPS	1031	1.1 %
SKE, SKE-D, SKE-P	1032	1.2 %
SKE-A	999	-2.1 %
RKE	1008	-1.2 %
SST	1038	1.8 %
CKE	1027	0.7 %

The comparison of the Reynolds stress transport models in the present simulations, with the simulations by Klein [29], is given in Fig. 6.2. The four Reynolds stress components are used for verification of the Reynolds stress transport models in STAR-CCM+. The mean streamwise velocity, turbulence energy, and vertical

Reynolds stress component profiles, calculated by all turbulence models, are presented in Fig. 6.3. The vertical Reynolds stress component is of particular interest due to the requirements in NORSOK Standard C-004 [44], and is presented in the other validation and verification simulations as well.

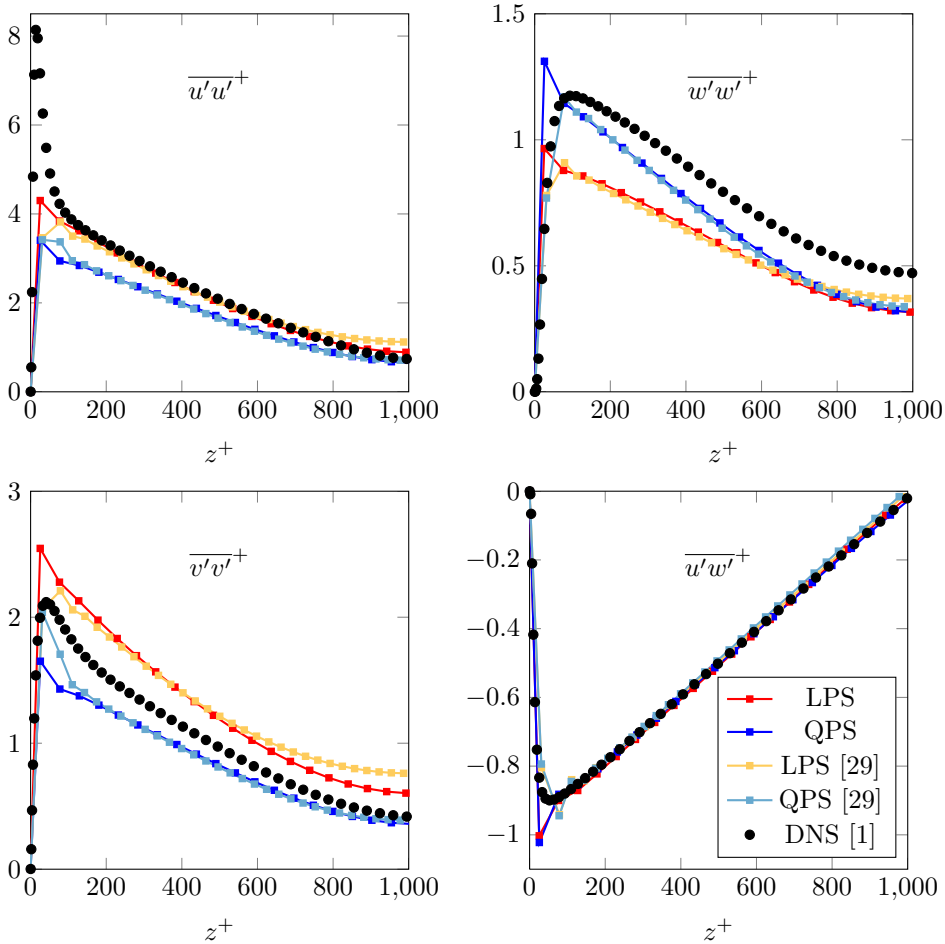


Figure 6.2: Dimensionless kinematic Reynolds stress profiles compared with simulations by Klein [29] and DNS by Abe et al. [1].

The Reynolds stress profiles in Fig. 6.2 indicate that the tested models are similar to the models used by Klein [29]. The curves are almost identical in most of the domain, but the values in the cells closest to the wall, $25 \lesssim z^+ \lesssim 125$, are somewhat different. Simulation with slightly bigger cell sizes were tested to see if the differences in mesh and z_{wall}^+ between the present simulations and the simulations by Klein [29], could cause this divergence. However, the same differences were found in the simulations with slightly bigger cells.

A second possibility is that the values in the cells closest to the wall are different because the wall functions are different. Klein [29] uses the following expression for the dissipation rate at the wall.

$$\varepsilon = \frac{k^{\frac{3}{2}}}{2.55z} \quad (6.12)$$

The present simulations use Eq. (5.23). The two expressions are equal when $C_\mu = 0.09$, but this is not the case in STAR-CCM+. As mentioned in Section 4.1, the tested Reynolds stress transport models in STAR-CCM+ use $C_{\mu,LPS} = 0.065536$ and $C_{\mu,QPS} = 0.098596$, which give different dissipation rates at the wall.

The difference in C_μ may be an explanation for the divergence close to the wall, but the Reynolds stress components far from the wall are also somewhat different in the present simulations compared to the simulations by Klein [29], most noticeable for the LPS model. This divergence may come from different modeling of the turbulence diffusion. An isotropic model, with the given C_μ values, is used in the present simulations, while Klein [29] uses the generalized gradient diffusion model by Daly and Harlow [11]. The generalized gradient diffusion model is also used in the dissipation rate equation by Klein [29], while the present simulations use the isotropic model here as well. Additionally, the function f_w , Eq. (4.12), is given without the maximum constraint in the equation used by Klein [29].

The dimensionless mean streamwise velocity, turbulence energy, and vertical Reynolds stress component profiles, for all turbulence models, are presented in Fig. 6.3. The maximum limit on the turbulence timescale had no effect on the SKE model for this test case. The green curve in Fig. 6.3 is therefore representative for the SKE, SKE-D and SKE-P models.

The velocity profiles are similar for all models, and almost spot on the DNS by Abe et al. [1]. The magnitude of the velocity profile is somewhat smaller with the SST model than with the other models. More significant differences are found for the turbulence energy plots. The tuning of coefficients in the SKE-A model, to satisfy atmospheric conditions, makes the model unsuited for this case, as it clearly overestimates the turbulence energy.

The peak in turbulence energy close to the wall is not correctly predicted with any turbulence model, although the SKE-A model is close due to its general overprediction. The same was found for the calculations of the streamwise Reynolds stress component with the Reynolds stress transport models in Fig. 6.2. The rest of the turbulence energy profiles are similar for the different models (except SKE-A), and close to the DNS by Abe et al. [1]. The best performance is found with the LPS model, while the worst is found with the QPS model which underestimates the turbulence energy, similarly to the underestimated streamwise Reynolds stress component in Fig. 6.2. All turbulence energy transport models (except SKE-A) have profiles between the two Reynolds stress transport models in most of the domain.

The turbulence energy transport models overestimate the vertical Reynolds stress component. As already mentioned, the expression for the variance of the vertical velocity component with the Boussinesq viscosity assumption simplifies to $\overline{w'w'} = \frac{2}{3}k$ for a fully developed channel flow. The vertical Reynolds stress component should however be smaller than the isotropic assumption, as confirmed by the DNS, and the vertical Reynolds stress component profiles are therefore overpredicted by all turbulence energy transport models. The CKE model which is based on a nonlinear extension to the Boussinesq viscosity assumption, suffers from the same problem. Close to the wall, where the anisotropy is largest, the calculations of the vertical Reynolds stress component are approximately 100 % larger than the DNS data. Far from the wall, where the differences between the normal Reynolds stress components even out, the turbulence energy transport models perform better. The RKE model is especially good at predicting the vertical Reynolds stress component in this region, and is the best model for $z^+ > 700$. The Reynolds stress transport models perform significantly better in the whole region, but they are not perfect. Both models underestimate the vertical Reynolds stress component compared to the DNS, with the calculations with the QPS model being somewhat better than the calculations with the LPS model.

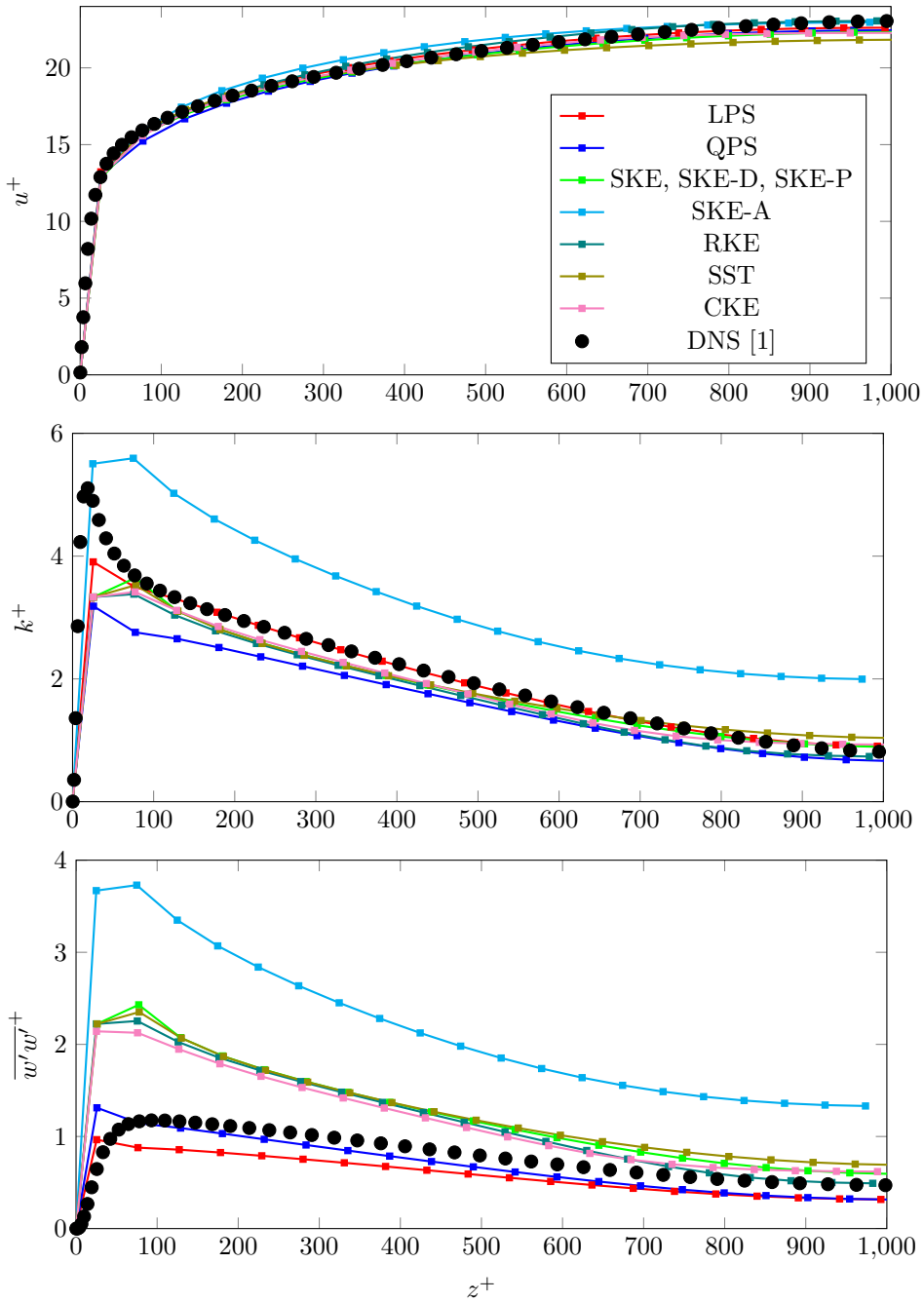


Figure 6.3: Dimensionless mean streamwise velocity, turbulence energy, and variance of vertical velocity component compared with DNS by Abe et al. [1].

6.2 Backward-facing step

6.2.1 Case description and setup

The backward-facing step chosen to be simulated is based on the experiment performed by Driver and Seegmiller [13] with zero degree divergence of the top wall. Experimental measurements for this setup are available online [45]. The Driver and Seegmiller [13] case has an 8:1 inlet channel to step height ratio. When testing turbulence models on a backward-facing step case, the step size should be small compared to the total height of the channel. This will keep the pressure gradient limited, and the calculated flow field will depend more on the turbulence modeling [30].

The Reynolds number for this backward-facing step case is $Re_\theta = 5000$ based on the inlet reference velocity, $u_r = 44.2 \text{ m s}^{-1}$, and the boundary layer momentum thickness, θ , four step heights upstream of the step [13].

$$Re_\theta = \frac{\rho\theta u_r}{\mu} = 5000 \quad (6.13)$$

This corresponds to a Reynolds number of $Re_H = 36\,000$ based on the step size, $H = 1.27 \times 10^{-2} \text{ m}$ [45].

$$Re_H = \frac{\rho H u_r}{\mu} = 36\,000 \quad (6.14)$$

The first location where Driver and Seegmiller [13] have measured the velocity profile is four step heights upstream of the step. The inlet of the simulations is therefore placed here, and the measured values for the mean streamwise velocity component are used directly as inlet conditions for \bar{u} . The measured vertical velocity component is small and assumed negligible. The density at the inlet is taken from the material database in STAR-CCM+.

$$\rho = 1.184 \text{ kg m}^{-3} \quad (6.15)$$

The dynamic viscosity is found from the Reynolds number, Eq. (6.14).

$$\mu = \frac{\rho H u_r}{Re_H} = 1.846 \times 10^{-5} \text{ kg m}^{-1} \text{ s}^{-1} \quad (6.16)$$

In addition to the velocity, the Reynolds stress components $\overline{u'u'}$, $\overline{w'w'}$, and $\overline{u'w'}$, are measured by Driver and Seegmiller [13] at the inlet. These profiles are used directly, while the same assumption as in the fully developed channel flow is used for the lateral Reynolds stress, $\overline{v'v'}$.

$$\overline{v'v'} = 0.6\overline{u'u'} \quad (6.17a)$$

$$k = \frac{1}{2} (\overline{u'u'} + \overline{v'v'} + \overline{w'w'}) \quad (6.17b)$$

The dissipation rate and specific dissipation rate are approximated as follows.

$$\varepsilon = \frac{C_\mu^{\frac{3}{4}} k^{\frac{3}{2}}}{L} \quad (6.18a)$$

$$\omega = \frac{\varepsilon}{k\beta^*} = \frac{k^{\frac{1}{2}}}{C_\mu^{\frac{1}{4}} L} \quad (6.18b)$$

$$L = \kappa \min[z - H, 9H - z] \quad (6.18c)$$

A constant $C_\mu = \beta^* = 0.09$ is used to calculate the inlet dissipation rate for all models. The inlet profile for the dissipation rate is dependent on a length scale which has been approximated as the von Kármán constant times the wall distance [42]. Merci et al. [42] reported that the dependence on inlet conditions for the backward-facing step case is noticeable, but not of major importance. Other profiles for the lateral Reynolds stress and the dissipation rate are therefore not tested.

The backward-facing step case is simulated as a two-dimensional case in STAR-CCM+, illustrated in Fig. 6.4. Origin is placed at the bottom of the step. The inlet, which is placed at $x = -4H$, is modeled with the velocity inlet boundary type in STAR-CCM+. The outlet is placed $32H$ downstream of the step, and modeled with a pressure outlet boundary type. The remaining boundaries, the step top, the step, the bottom wall, and the top wall, are modeled as no-slip walls with wall-functions for turbulence quantities.

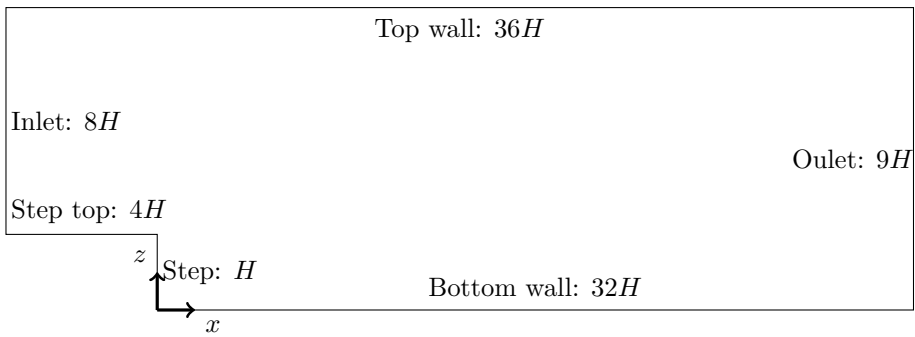


Figure 6.4: Backward-facing step domain. The sketch is not drawn to scale.

The mesh is made with the trimmed mesher in STAR-CCM+ and consists of square cells. As for the fully developed channel flow, the mesh is based on the geometry made with the 3D-CAD model tool. The mesh is then converted to use for a two-dimensional setup. The mesh region is split in two, an upper and a lower region, as is done in a backward-facing step tutorial in the STAR-CCM+ documentation

[7, p. 8141]. The upper region consists of all cells above $z = 1.5H$. These cells have lengths Δ . The lower region is for all cells below $z = 1.5H$ and consists of cells with lengths $\frac{1}{2}\Delta$.

6.2.2 Results

Different Δ values have been tested to check the mesh dependence and z_{wall}^+ values. The mesh dependence test was done for the QPS model by comparing the resulting reattachment lengths. Turbulence models typically underestimates the reattachment length [30], as is also the case for most models in the present simulations. There are different techniques available for determination of the reattachment length. In this thesis, the reattachment length is found by linear interpolation between the two cells where the wall shear stress becomes positive at the bottom wall.

The results from the mesh dependence test are given in Table 6.3. The z_{wall}^+ values are calculated for the last cell before the step on the step top.

Table 6.3: Reattachment lengths calculated with the QPS model for different meshes.

Name	Δ	Cells	Reattachment length: x_r/H	z_{wall}^+
<i>bfs1</i>	$0.2H$	18 770	4.91	73
<i>bfs2</i>	$0.1H$	72 920	5.52	37
<i>bfs3</i>	$0.05H$	292 102	5.79	18
<i>bfs4</i>	$0.025H$	1 147 280	5.81	9

The two coarser meshes have reattachment lengths significantly lower than the two finer meshes. The reattachment lengths are almost the same for the two finest meshes, but *bfs3* has a more suited z_{wall}^+ and the number of cells needed to be calculated is 25 % of *bfs4*. As mentioned for the fully developed channel flow, z_{wall}^+ could be lower than 30, but $z_{wall}^+ = 9$ may be too low. The second finest mesh, *bfs3*, has therefore been used for the rest of the simulations.

The use of wall functions on the bottom wall downstream of the step may be problematic in the backward-facing step. The z_{wall}^+ values in Table 6.3 are given for the last cell before the step, but the z_{wall}^+ values downstream of the step are too low for the wall function assumptions. At one step length downstream of the step, calculations with the second finest mesh gave $z_{wall}^+ \approx 7$, with some differences between different models. The z_{wall}^+ values increased to $z_{wall}^+ \approx 12$ and $z_{wall}^+ \approx 15$ two and three step sizes downstream of the step, respectively.

Hanjalić and Jakirlić [23] discussed the problem with invalid wall functions in the recirculation zone of the backward-facing step case. Even though the assumptions for the wall boundary conditions were invalid, they concluded that the general flow patterns were reproduced reasonably well. They recommended the use of standard

wall functions even if the z_{wall}^+ values became too low. This approach would give considerably better results than switching to a linear law for $z_{wall}^+ < 11$ [23].

The effects of adjusting the z_{wall}^+ values on the bottom wall have been investigated. The second finest mesh, *bfs3*, was simulated with increased cell sizes next to the bottom wall. Simulations were run with both doubled and quadrupled cell sizes close to the bottom wall, referred to as the doubled mesh and the quadrupled mesh. Both simulations had two layers with these cells before switching to the standard cells. The quadrupled mesh had three layers of doubled cells between the standard and quadrupled cells. The LPS and SKE models were tested. Both models calculated $z_{wall}^+ > 15$ one step length downstream of the step with the doubled mesh, and $z_{wall}^+ > 30$ with the quadrupled mesh.

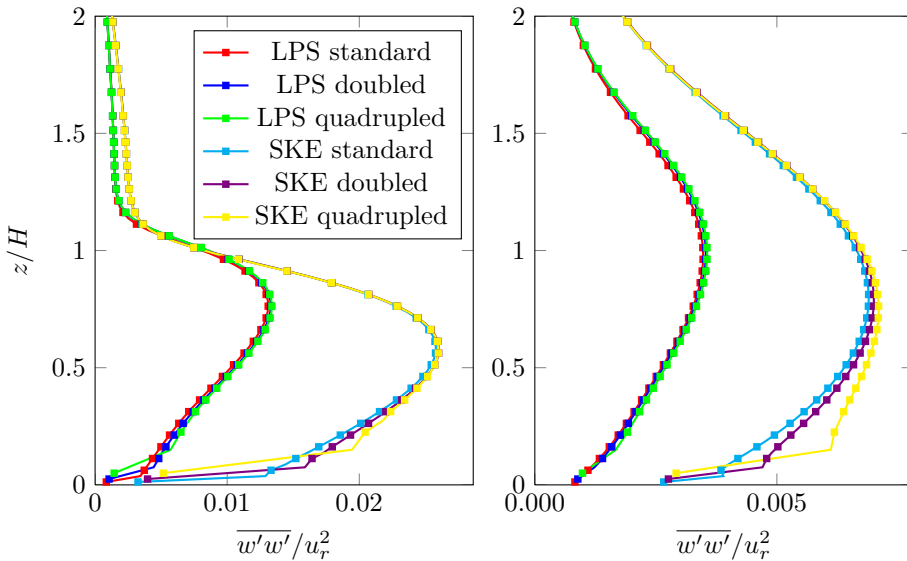


Figure 6.5: Dimensionless variance of vertical velocity component at $x = 4H$ (left) and $x = 20H$ (right) with increased cell sizes close to the bottom wall.

Figure 6.5 presents the two models with different near wall cell sizes at the bottom wall, inside the recirculation zone (left) and far downstream of the step (right). The SKE model is somewhat affected close to the wall, most noticeable far downstream of the step, but the differences are small, and the second finest mesh, *bfs3*, is therefore used for the rest of the simulations. Even though Fig. 6.5 illustrates that the low z_{wall}^+ values are acceptable inside the recirculation zone, the assumptions may still be invalid. Wall functions are typically developed for simple boundary layer flows [18, p. 74], and the assumptions for developing wall functions may be invalid even though the z_{wall}^+ values are acceptable.

Reattachment lengths calculated with the second finest mesh are presented in Table 6.4. Results from simulations performed by others are given for comparison. As

well as the reasons mentioned in Section 6.1.2, the uncertainty of using invalid wall functions may be an explanation for the differences in reattachment lengths between the present simulations and simulations by others. The results in Table 6.3 also indicated that the reattachment lengths are sensitive to the mesh resolution. Different boundary conditions and inlet profiles are other possible explanations.

Table 6.4: Reattachment length for different turbulence models in STAR-CCM+ compared with experiment by Driver and Seegmiller [13].

Model	Reattachment length	
	x_r/H	Deviation from exp. [13]
LPS	5.06	-19 %
QPS	5.79	-7 %
SKE	5.38	-14 %
SKE-A	10.06	61 %
SKE-D	6.31	1 %
SKE-P	5.38	-14 %
RKE	6.06	-3 %
SST	6.72	7 %
CKE	6.12	-2 %
Experiment [13]	6.26	-
LPS [4]	5.44	-13 %
LPS [47]	5.67	-9 %
QPS [4]	5.40	-14 %

The reason for testing the SKE-A model is to see if the tuned coefficients influence the model behavior. A 61 % overshoot of the reattachment length compared with the experiment is found, significantly more than the other models. The SKE-A model may therefore be unsuited for flows with separation and recirculation. The other models are closer to the experimental measurement. Newer models are found to perform better than older models at predicting the reattachment length. The RKE model (1994), the CKE model (1996), and the SKE-D model (1996), are significantly better than the SKE model (1972) at predicting the experimental reattachment length. The same can be said about the QPS model (1991) compared to the LPS model (1978). The increased accuracy may indicate that newer models perform better, but it is also possible that flows similar to the backward-facing step have been more important in tuning of model coefficients for these models. As can be seen from the result with the SKE-A model, tuning the coefficients of a model changes the model significantly. Although the newer models seem to predict better reattachment lengths for this test case, the models can perform worse in other situations.

As was the case for the fully developed channel flow, using Park's constraint [48], SKE-P, does not affect the performance for the backward-facing step case. This confirms that $C_T = 2$ is a conservative value in the expression for the turbulence

timescale. The constraint may be useful to obtain a realizable version of the SKE model, without major changes on the behavior of the model.

Measurements of velocity and Reynolds stress profiles are done at several locations in the experiment by Driver and Seegmiller [13]. Like for the fully developed channel flow, profiles of the dimensionless mean streamwise velocity component and the variance of the vertical velocity component are presented. The same user field function as in the fully developed channel flow, $wv2D$, is used to obtain the vertical Reynolds stress component for the turbulence energy transport models. The turbulence energy is not presented, as experimental data for the lateral Reynolds stress component were not found. The profiles are made dimensionless with the reference velocity, $u_r = 44.2 \text{ m s}^{-1}$.

The mean streamwise velocity component and the variance of the vertical velocity component have been evaluated at six locations downstream of the step. The first three locations downstream of the step, $x = 4H$, $x = 6H$, and $x = 8H$, are close to the reattachment point, while the last three, $x = 12H$, $x = 16H$, and $x = 20H$, show the development of the flow after reattachment. The profiles at $x = 6H$ and $x = 20H$ are presented in Figs. 6.6 and 6.7, while the profiles at the other locations are given in App. A. The measurements by Driver and Seegmiller [13] are given for comparison.

The Reynolds stress transport models underestimate the peak of the experimental vertical Reynolds stress component profile close to the reattachment point, as seen in Fig. 6.6. The vertical Reynolds stress component is typically overpredicted by the turbulence energy transport models. The same pattern was found for the fully developed channel flow, and indicates the incapability of calculating the correct anisotropic distribution of the normal Reynolds stress components with the Boussinesq viscosity assumption. However, the Reynolds stress transport models are not significantly better since these models underestimate the vertical Reynolds stress component by roughly the same amount as the overestimation with the turbulence energy transport models. The differences between the different models are smaller far from the wall.

The mean streamwise velocity component profiles in the figures close to reattachment are best predicted by the SKE and SKE-P models which are closer to the experimental measurements than the other models for $z < H$. The SKE-A model is found to perform significantly worse than the other models. The rest of the models predict similar velocity profiles, with some turbulence energy transport models found between the two Reynolds stress transport models, as seen in Fig. 6.6.

The last three figures show how the mean streamwise velocity component and vertical Reynolds stress component profiles have developed after reattachment. Ignoring the results from the SKE-A model, the turbulence energy transport models are as good as, or even better than, the Reynolds stress transport models in prediction of both profiles, as shown in Fig. 6.7. The differences are most significant close to the bottom wall. Here the SST model calculates the best vertical Reynolds stress component profile compared to the experiment.

The RKE model is one of the better turbulence models for calculation of the vertical Reynolds stress component further away from the wall. At $x = 20H$, it lies between the overestimating SKE and SKE-P models, and the rest of the models which underestimate the vertical Reynolds stress component compared to the experiment. As is also the case close to reattachment, the two Reynolds stress transport models underpredict the vertical Reynolds stress component. Although their profiles have the shape of the experimental data, the magnitudes are significantly lower. The LPS model is worst, and has a maximum Reynolds stress value more than 30 % lower than the corresponding experimental value, which is roughly the same as the overestimation with the SKE model.

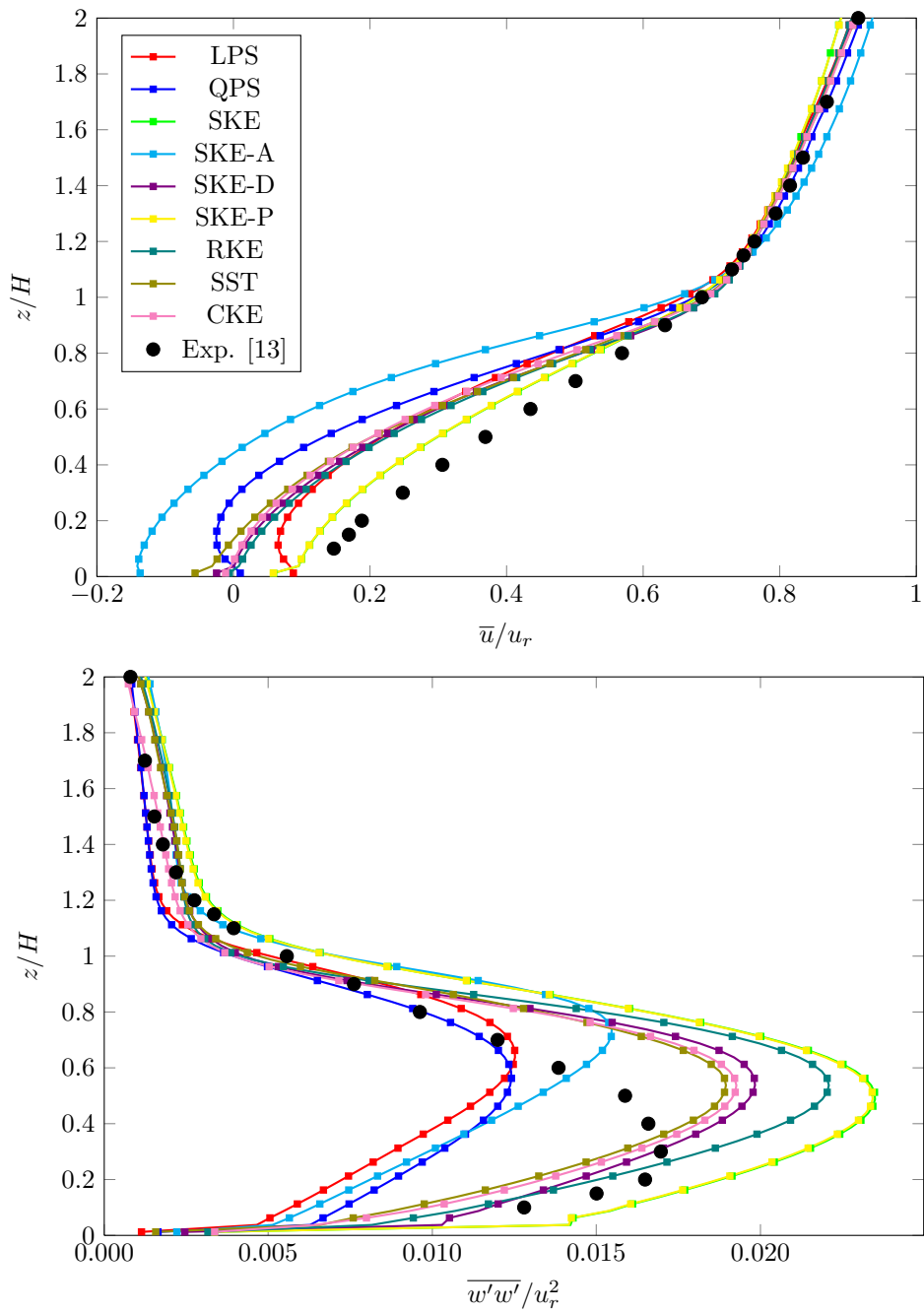


Figure 6.6: Dimensionless mean streamwise velocity component and variance of vertical velocity component at $x = 6H$.

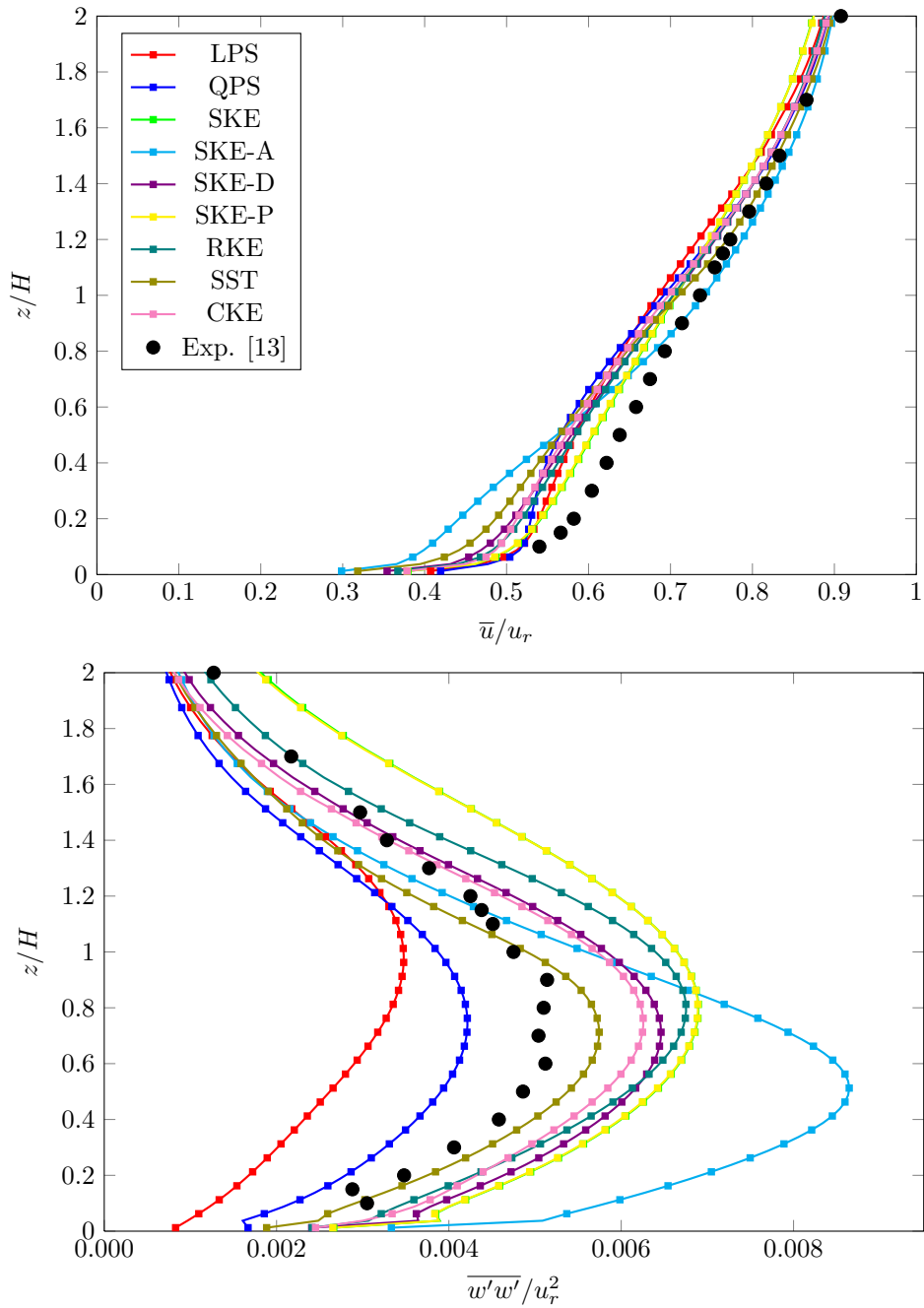


Figure 6.7: Dimensionless mean streamwise velocity component and variance of vertical velocity component at $x = 20H$.

6.2.3 Calculation time

Calculation times have been measured for the backward-facing step case with the second finest mesh, *bfs3*, and are presented in Table 6.5. Minor differences were found between the different turbulence energy transport models. Calculation times with the SKE-A, SKE-P, and SKE-D models were therefore not measured.

Table 6.5: Measured calculation times for the backward-facing step case.

Turbulence model	Iteration time	Iterations	Total time
LPS	2.9s	7900	6.4 hours
QPS	2.6s	7100	5.1 hours
SKE	1.2s	5400	1.8 hours
RKE	1.2s	5000	1.7 hours
SST	1.2s	5300	1.8 hours
CKE	1.4s	5100	2.0 hours

Five transport equations are solved when a turbulence energy transport model is used, while the Reynolds stress transport models require eight transport equations to be solved. All models solve the Reynolds-averaged continuity equation, two components of the Reynolds-averaged momentum equation, and a dissipation rate equation. In addition, the turbulence energy transport models solve one equation for the turbulence energy, while the Reynolds stress transport models solve four equations, $\overline{u'u'}$, $\overline{v'v'}$, $\overline{w'w'}$, and $\overline{u'w'}$. This corresponds well to doubled iteration times.

The number of iterations are increased as well. According to the STAR-CCM+ documentation, the increase in iterations for convergence is typical for Reynolds stress transport models due to numerical stiffness in the Reynolds stress transport equations [7, p. 3412]. The same patterns were found for the fully developed channel flow and the surface-mounted cube cases. The increase in iteration times are roughly doubled, but the total calculation times are three to four times the calculation times with the turbulence energy transport models, due to an increase in the number of iterations.

Due to convergence issues, calculation times were not measured in the helideck simulations. Both Reynolds stress transport models needed the converged solution from the simulation of another turbulence model as initial value in order to converge for some wind headings. This made a direct comparison of calculation times impossible. For a three-dimensional simulation, there is one more component in the Reynolds-averaged momentum equation and two more Reynolds stress transport equations. The total number of transport equations in the helideck simulations are therefore six and eleven for a simulation with a turbulence energy transport model and a Reynolds stress transport model, respectively. The difference between the two approaches in calculation times for a three-dimensional case may therefore be roughly the same as for a two-dimensional setup.

6.3 Surface-mounted cube

6.3.1 Case description and setup

The surface-mounted cube case is simulated to see how the turbulence models perform upstream and downstream of a three-dimensional obstacle. The setup is based on an experiment by Martinuzzi and Tropea [38], where a cube is placed on the bottom wall of a fully developed channel flow. According to personal communication with R. Martinuzzi, the surface-mounted cube experiments were validated in two different air channels and one water channel. The results were then scaled to a Reynolds number of 40 000 based on the bulk velocity and the lengths of the cube.

$$Re_l = \frac{\rho u_b l}{\mu} = 40\,000 \quad (6.19)$$

The lengths of the cube are $l = 0.025$ m in the experiment, which is used in the simulations as well. The bulk velocity is approximated to $u_b = 19.3$ m s⁻¹ based on numerical integration of the velocity profile from the experimental data three cube lengths upstream of the cube [63]. Like in the backward-facing step case, the standard value for density is used, and the dynamic viscosity is calculated from the Reynolds number.

$$l = 0.025 \text{ m} \quad (6.20)$$

$$u_b = 19.3 \text{ m s}^{-1} \quad (6.21)$$

$$\rho = 1.184 \text{ kg m}^{-3} \quad (6.22)$$

$$\mu = \frac{\rho l u_b}{Re_l} = 1.428 \times 10^{-5} \text{ kg m}^{-1} \text{ s}^{-1} \quad (6.23)$$

Inlet conditions are taken from the experimental measurements three cube lengths upstream of the cube. The velocity profile in the streamwise direction is used directly, while the lateral and vertical velocities are small and neglected. Experimental Reynolds stress profiles are given for $\overline{u'u'}$, $\overline{w'w'}$, and $\overline{u'w'}$. The same assumption as for the other test cases, $\overline{v'v'} = 0.6\overline{u'u'}$, is used for the lateral Reynolds stress profile. The last Reynolds stress profiles are assumed equal to zero. The dissipation rate and specific dissipation rate are approximated as follows.

$$\varepsilon = \frac{C_\mu^{\frac{3}{4}} k^{\frac{3}{2}}}{L} \quad (6.24a)$$

$$\omega = \frac{\varepsilon}{k\beta^*} = \frac{k^{\frac{1}{2}}}{C_\mu^{\frac{1}{4}} L} \quad (6.24b)$$

Where L has been set to 0.07 times the width of the channel, 0.60 m, that is, $L = 0.042$ m [71, p. 77], and $C_\mu = \beta^* = 0.09$ for all models.

The domain setup is illustrated in Fig. 6.8. The inlet, modeled with a velocity inlet boundary type, is placed three cube lengths upstream of the cube. The outlet is modeled as a pressure outlet and placed 51 cube lengths downstream of the cube. The width of the channel is 24 cube lengths and the height is two cube lengths. All boundaries except the inlet and outlet are modeled as no-slip walls.

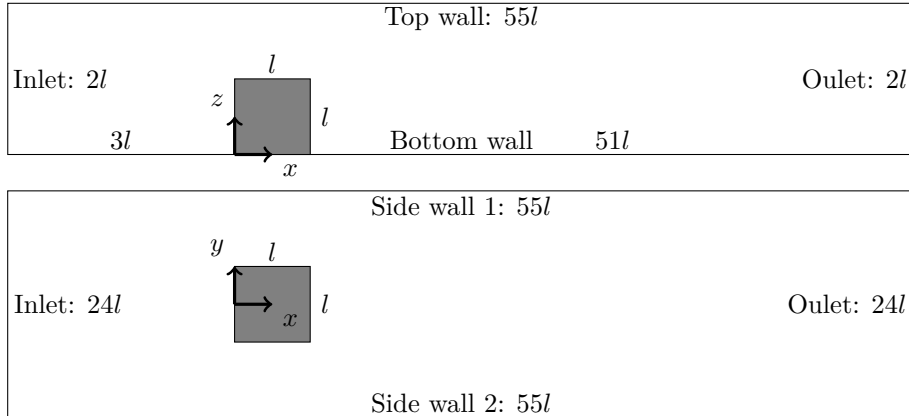


Figure 6.8: Surface-mounted cube domain seen from side (top) and above (bottom). The sketches are not drawn to scale.

The mesh is made with the trimmed mesher and surface remesher, based on the geometry created with the 3D-CAD model tool, and all cells are cubes with equal lengths in the three directions. Since the main region of interest, and the largest gradients, are found close to the surface-mounted cube, the mesh is made finer by use of volumetric controls in this region of the domain. The growth rate is set to slow to ensure a gradual transition from larger cells far from the cube, as shown in Fig. 6.9. The cell sizes in the refined regions are set as a fraction of the base size, Δ , such that variations of Δ affects all cells in the domain.

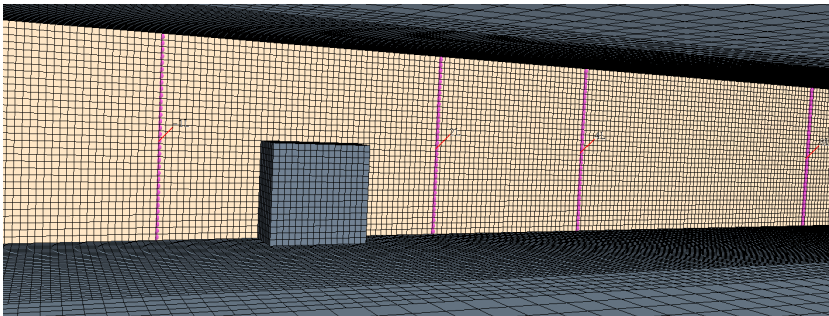


Figure 6.9: Mesh refinement close to the cube. Measurement lines illustrated by pink dots, while the yellow “wall” is a plane section through the origin.

The variance of the vertical velocity component is, like in the other simulations,

found by use of a user field function for the models that use the Boussinesq viscosity assumption. The formulation for the field function is different from the previous simulations since this is a three-dimensional case. The field function is named *ww3D* and written as follows.

$$\text{ww3D} = 2/3 * \text{TurbulentKineticEnergy} \\ - 2 * \text{TurbulentViscosity} / \text{Density} * \text{W_VelocityGrad} [2]$$

6.3.2 Results

A mesh dependence test was done for the surface-mounted cube case. The SKE model was tested for different Δ values and the reattachment lengths downstream of the cube were compared. The results are presented in Table 6.6. The “Near cube” column represents the relative refinement of the base size in the volumetric control close to the cube. The z_{wall}^+ values that are presented, were measured one cube length upstream of the cube. The smallest z_{wall}^+ value found in the domain with the finest mesh was $z_{wall}^+ = 14$. Too low z_{wall}^+ should therefore not be a major issue for this test case.

Table 6.6: Mesh for surface-mounted cube case.

Name	Δ	Near cube	Cells	Reattachment: x_l/l	z_{wall}^+
<i>smc1</i>	0.025 m	50 %	7644	0.45	465
<i>smc2</i>	0.025 m	25 %	22 000	2.17	230
<i>smc3</i>	0.0125 m	25 %	109 128	2.20	115
<i>smc4</i>	0.00625 m	25 %	680 950	2.10	56

The coarsest mesh is clearly a bad choice. There are minor differences between the reattachment lengths of the three finer meshes. The reattachment length is closer to the finest mesh with the third finest mesh than with the second finest mesh. This may seem odd, but is likely to be related to the way the reattachment lengths have been calculated. The same method as in the backward-facing step has been used, a linear interpolation between the two cells where the wall shear stress becomes positive on the bottom wall downstream of the cube. The profile for the wall shear stress is not linear, and the assumption may give a small error.

An evaluation of the calculated turbulence energy seven cube lengths downstream of the cube was done to further investigate the mesh dependence, as seen in Fig. 6.10. The three finest meshes are again found close to each other, but the resolution of the plots are obviously best with the finest mesh.

Some of the turbulence models did not converge with the three finest meshes. Tuning of under-relaxation parameters and use of a transient solver were tested, but divergence was still an issue. Use of a first-order upwind scheme for the convective term in the Reynolds-averaged momentum equation solved the problem and gave

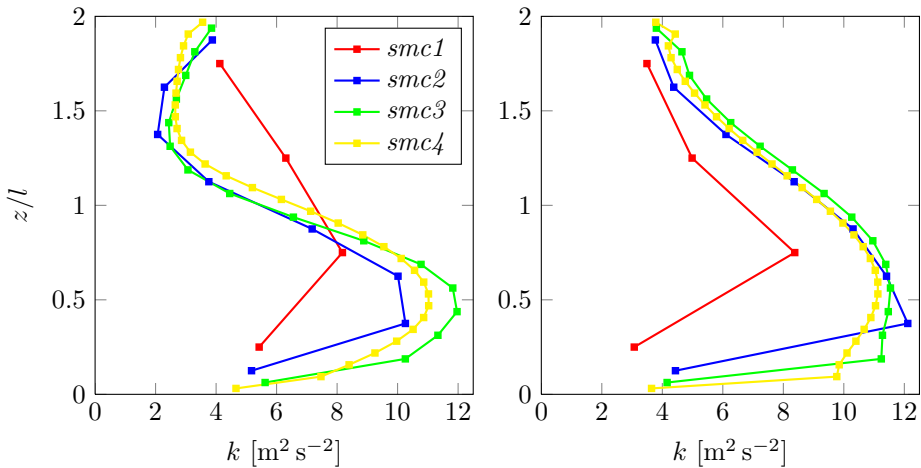


Figure 6.10: Turbulence energy with the LPS (left) and SKE (right) models at $x = 8l$ for four mesh qualities.

convergent solutions for all models. As mentioned in Section 5.1.2, upwind schemes produce an error of diffusion-like appearance. The added diffusion smooths out singularities and enhance stability. The erroneous diffusion may be decreased if the order of the scheme is increased or if the resolution of the calculation mesh is increased [71, p. 151]. An investigation of the error produced with the first-order scheme, compared to the second-order scheme, was therefore necessary.

Figure 6.11 presents the turbulence energy seven cube lengths downstream of the cube with the LPS and SKE models for the two finest meshes. Both the first-order and the second-order upwind schemes are tested for the convective term in the Reynolds-averaged momentum equation. The figure clearly illustrates that a significant error is found with the first-order upwind scheme. It is also clear that mesh refinement counteracts the problem. The finest mesh is therefore used for the final simulations of the surface-mounted cube.

The increased numerical diffusion with the first-order upwind scheme reduce the turbulence energy calculations for both the LPS and SKE models. The LPS model is found to be more dependent than the SKE model on the scheme order of the convective term in the Reynolds-averaged momentum equation, as seen in Fig. 6.11. This can be related to the less favorable numerical coupling between the flow and turbulence equations in Reynolds stress transport models. According to Pope [50, pp. 459–460], there are three main reasons why Reynolds stress transport models are more difficult and costly compared to the $k-\varepsilon$ model. Increased amount of turbulence equations and more complicated turbulence equations are the first two, while the less favorable numerical coupling, resulting from solving the Reynolds stress tensor directly, is the third reason.

The QPS, SKE-A, SKE-D, and SST models needed the first-order upwind scheme

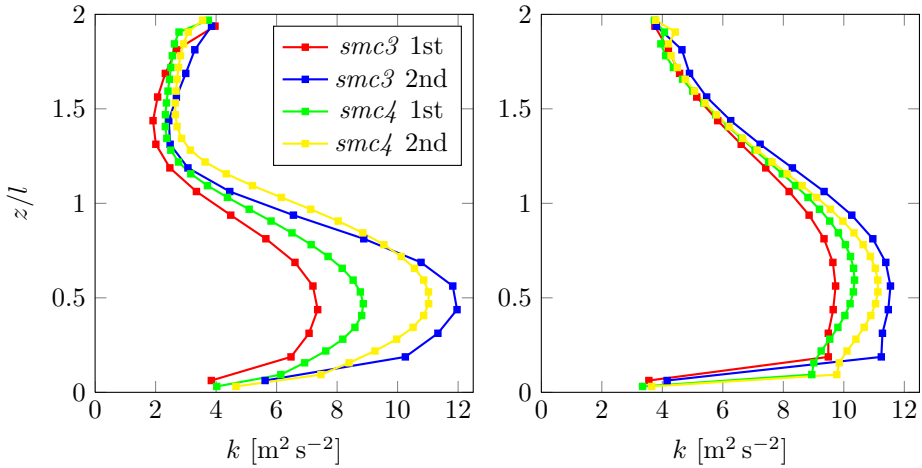


Figure 6.11: Turbulence energy with the LPS (left) and SKE (right) models at $x = 8l$ with the two finest meshes using 1st and 2nd order upwind schemes.

to produce convergent solutions for both the second finest and the finest mesh. The CKE model converged with the second-order scheme for the second finest mesh, but needed the first-order scheme with the finest mesh. The four other models, LPS, SKE, SKE-P, and RKE, are presented with the second-order upwind scheme. Comparing models with a first-order and a second-order scheme may seem like comparing apples and oranges. Alternatively, all models could have been compared using the first-order scheme. However, stability may also be seen as a parameter for turbulence model performance. The models that converged with the second-order scheme are therefore presented using the second-order scheme.

Reattachment lengths have been calculated for all models with the finest mesh, and are presented in Table 6.7. The calculated lengths are compared with the experimental measurement by Martinuzzi and Tropea [38]. All models calculate too long reattachment lengths behind the cube compared to the experiment. The SKE model is the best model at this test. Notice that the increased false diffusion caused by the first-order upwind scheme has a positive effect for both the LPS and SKE models. To choose a turbulence model and order of an upwind scheme based on such simple tests may therefore be insufficient.

The mean velocity in the streamwise direction and the variance of the vertical velocity component have been evaluated at $x = -1l$, $x = 2l$, $x = 4l$, and $x = 8l$. Profiles at $x = -1l$ and $x = 8l$ are given in Figs. 6.12 and 6.13, while profiles at the two other locations are given in App. B.

Figure 6.12 presents the profiles one cube length upstream of the cube. The velocity profiles are good compared to the experimental measurements. Most models lie almost spot on the experimental velocity profile, except for the SKE and SKE-A models, which calculate somewhat higher velocities close to the walls, and lower

Table 6.7: Reattachment lengths downstream of the cube compared to the experimental measurement by Martinuzzi and Tropea [38] provided in [54].

Model	Upwind scheme	Reattachment length	
		x_l/l	Deviation
LPS	1st order	2.36	47 %
LPS	2nd order	2.44	51 %
QPS	1st order	3.25	102 %
SKE	1st order	1.96	22 %
SKE	2nd order	2.09	30 %
SKE-A	1st order	2.68	67 %
SKE-D	1st order	3.25	102 %
SKE-P	2nd order	2.22	38 %
RKE	2nd order	2.68	67 %
SST	1st order	2.88	79 %
CKE	1st order	2.90	80 %
Experiment [38]	-	1.61	-

velocities in the center. The velocity profile calculated by the SKE-P model is found between the SKE model and the other models.

The Reynolds stress transport models have profiles for the variance of the vertical velocity close to the experimental measurements at $x = -l$. The LPS model is a little better than the QPS model which has a slight overestimation of this Reynolds stress. The vertical Reynolds stress component is overestimated by the turbulence energy transport models as well, seemingly due to weaknesses with the Boussinesq assumption. Even though this is upstream of the cube, just two cube lengths downstream of the inlet, there are significant differences between the turbulence energy transport models. The SKE, SKE-A, and SKE-P models, which had somewhat different velocity profiles compared to the rest of the models, have vertical Reynolds stress component profiles with significantly larger values than the experiment. The SKE-A model calculates a negative value for the variance of the vertical velocity in one of the cells close to the center of the channel, which proves that this model is unrealizable. It seems that a limit on the turbulence timescale improves the performance for the SKE model at this location, with SKE-P ($C_T = 2$) and SKE-D ($C_T = 0.6$) being gradually closer to the experimental data.

There is not much information about the lateral Reynolds stress in the experimental data [63], and measured values for the turbulence energy are only possible to obtain for six z -locations at $x = -l$, marked as black dots in Fig. 6.12. By allowing linear interpolation of the streamwise and vertical Reynolds stress components, with maximum 1 mm distance from the measured to the interpolated point, the turbulence energy can be calculated at four additional z -values. These values

are presented as black triangles in Fig. 6.12. Since the interpolation distance is minimal, the interpolated values can be considered to be sufficiently accurate.

The turbulence energy plot is presented to see if there are indications of the stagnation point anomaly with some of the turbulence models. The SKE and SKE-A models do not have any modifications to counteract the stagnation point anomaly, while the modification in the SKE-P model is conservative. These models have the largest turbulence energy values, significantly larger than the rest of the models, and about 100-300 % larger than the experimental values. The performance with the SKE-P model is somewhat better than the SKE model compared to the experiment, but the turbulence energy is still excessive. The excessive production is most dominant in the lower part of the domain, $z < l$, seemingly due to the cube being placed on the bottom wall.

The best calculated turbulence energy, compared to the experiment, is found with the SKE-D, SST, and CKE models. The first two models use a more active constraint on the turbulence timescale ($C_T = 0.6$) compared to the SKE-P model ($C_T = 2$), while the last model uses a variable C_μ formulation to counteract the stagnation point anomaly, as mentioned in Section 4.8. The performance of these three models are better than both the LPS and QPS models. The Reynolds stress transport models underestimate the turbulence energy close to the walls and overestimate the turbulence energy around $z = l$. The RKE model has a minor excessive production of turbulence energy, but the overall performance is fairly good, significantly better than the SKE, SKE-A, and SKE-P models.

The turbulence energy transport models have significant performance differences in calculations of the vertical Reynolds stress component compared to the calculations of the turbulence energy. The incapability of the Boussinesq viscosity assumption in returning the correct normal stress anisotropy is again illustrated. As seen in Fig. 6.12, the problem is most significant close to walls, where the normal stress anisotropy is largest.

The second measurement location is one cube length downstream of the cube. The profiles at this location are given in App. B. All models underestimate the magnitude of the vertical Reynolds stress component compared to the experiment. The LPS, RKE, and SKE-P models are among the least worst models, but even these models are far from the experimental values in the recirculation zone behind the cube, $0 < z \leq l$. The QPS, SST, and SKE-D models have lower values for the vertical Reynolds stress component. Part of the reason may be the use of a first-order scheme for the convective term in the Reynolds-averaged momentum equation, as was found to reduce the turbulence energy for the LPS and SKE models. The calculated velocity profiles are more consistent with the measured values, without too significant differences between the turbulence models. The RKE and SKE-P models are among the best models compared to the experimental measurements.

The next evaluated location is at $x = 4l$, presented in App. B. This is downstream of reattachment for most models, but the QPS and SKE-D models have

not reattachment, as seen with negative values for the mean streamwise velocity component. Since the reattachment length is overestimated with all models, the velocity profiles are underestimated in the lower part of the channel. The SKE and SKE-P models have the shortest reattachment lengths and calculate the best velocity profiles compared to the experiment at this location. The vertical Reynolds stress component at $x = 4l$ is better predicted than inside the recirculation zone for most models, with a less significant underestimation compared to the experimental measurements. The performance is more in accordance with the experiment in the upper half of the channel, seemingly due to the cube being placed on the bottom wall. Among the better turbulence model are the SKE-P, RKE, and SKE models, but the magnitude of the vertical Reynolds stress component close to the top wall is somewhat overestimated. The LPS model is more correct close to the top boundary, but has significantly lower values in the lower part of the domain. The first-order scheme models are generally disappointing. Especially bad is the performance of the SKE-A model, where the vertical Reynolds stress component is hugely overestimated in the upper part of the domain.

The last location, presented in Fig. 6.13, is found seven cube lengths downstream of the cube. All models underestimate the velocity profile in the lower half of the channel, as was also the case at $x = 4l$. The best profiles compared to the experiment are found with the SST and LPS models, while the QPS, SKE-D, and CKE models calculate the worst velocity profiles. As were found far downstream of the step in the backward-facing step case, the variance of the vertical velocity component profiles are underestimated compared to the experimental measurements with both Reynolds stress transport models. The turbulence energy transport models tend to overestimate the vertical Reynolds stress component. Worst profiles are found with the SKE-A model, while the SKE-D and RKE models are among the better turbulence energy transport models.

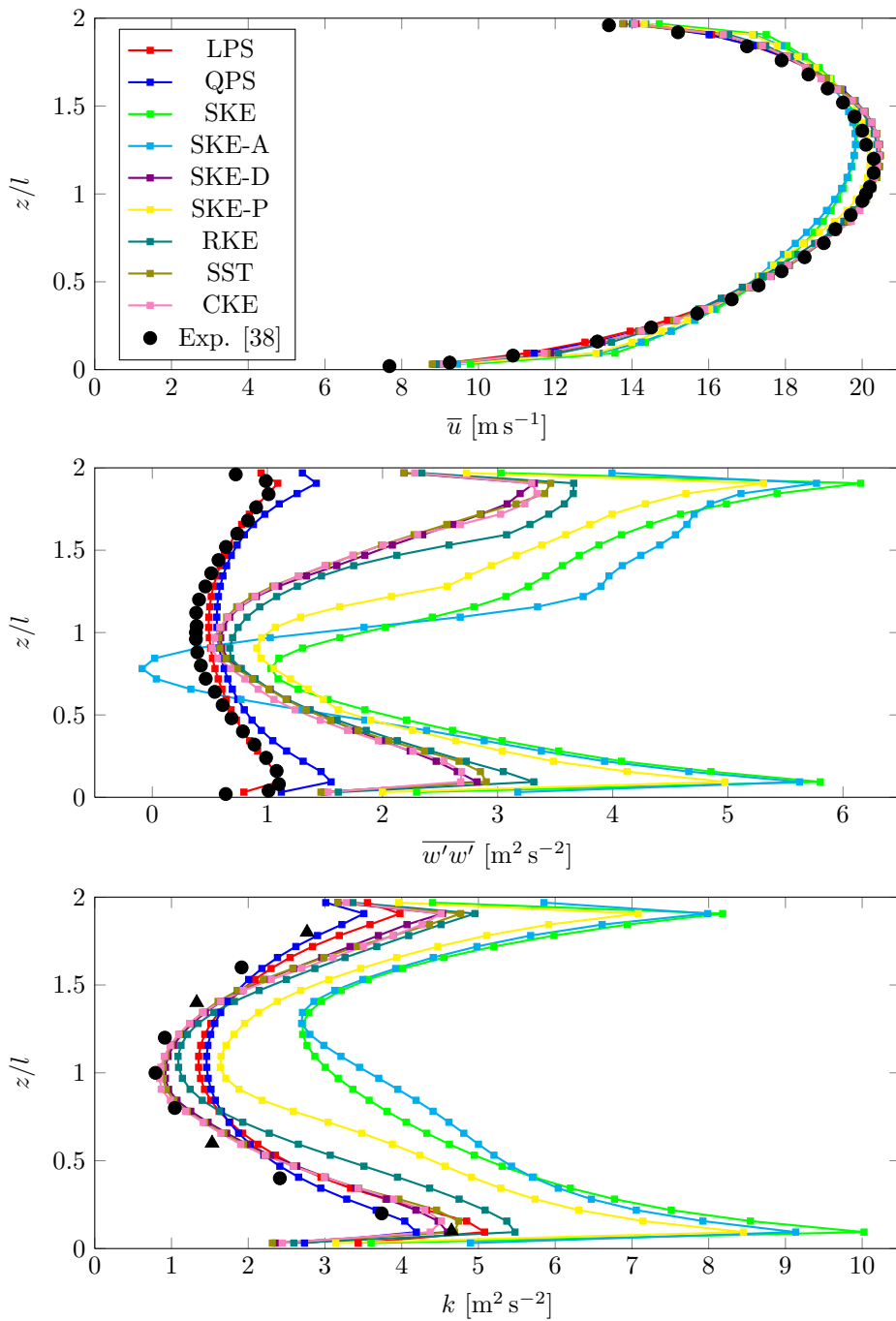


Figure 6.12: Mean streamwise velocity component, variance of vertical velocity component, and turbulence energy at $x = -1l$.

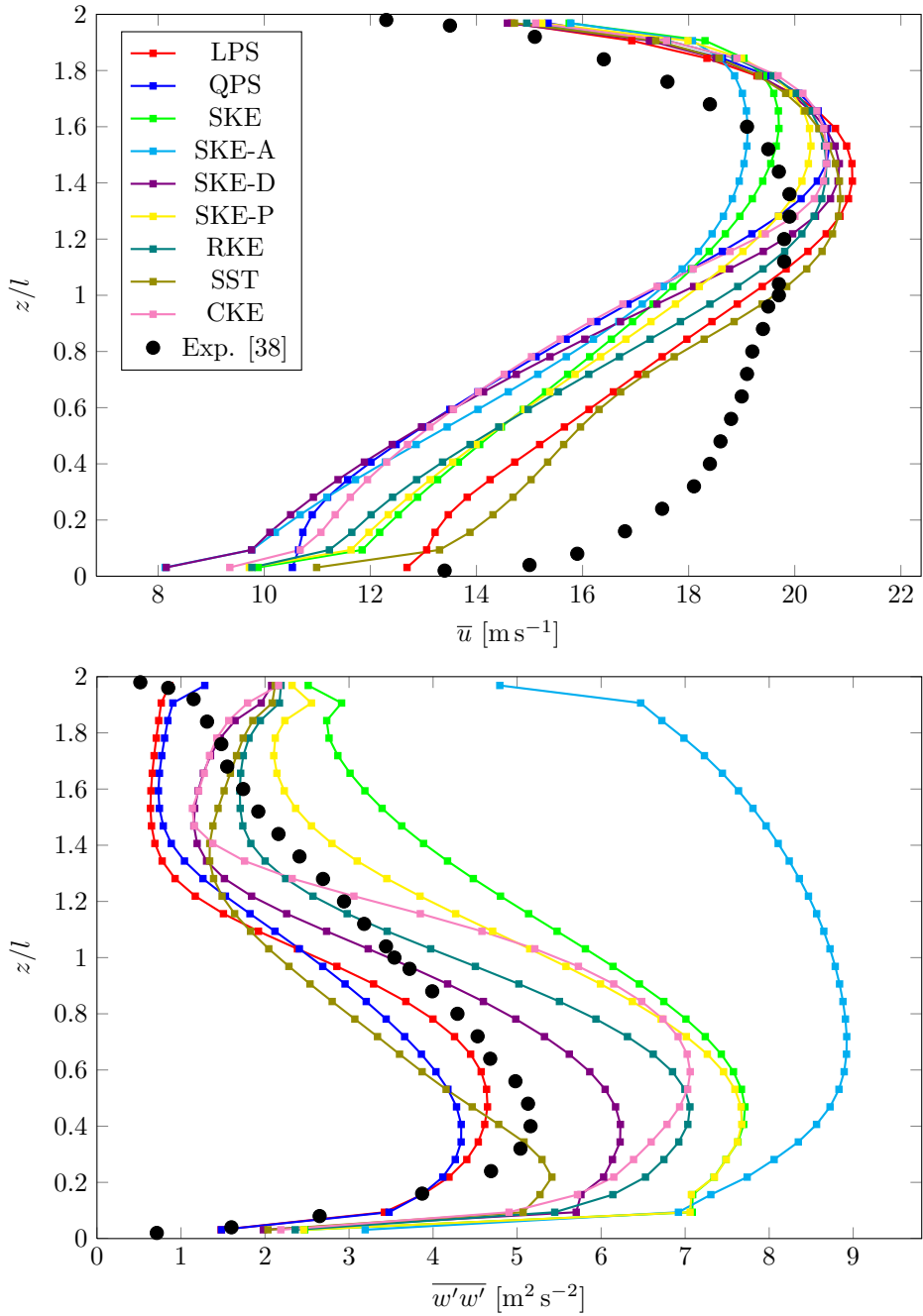


Figure 6.13: Mean streamwise velocity component and variance of vertical velocity component at $x = 8l$.

7 Helideck simulation setup

7.1 Atmospheric boundary layer conditions

The atmospheric boundary layer is the lowest part of the troposphere that is directly influenced by the surface of the Earth, and responds to surface forcings within a timescale of an hour [62, p. 2]. The thickness of the atmospheric boundary layer varies from 100 m to 3 km [62, p. 22]. The layer may be divided in an outer Ekman layer with little dependence on the surface, and an inner surface layer where surface effects are important [20, p. 2]. Unlike in the outer Ekman layer, the forces due to rotation of the Earth (Coriolis) are not significant in the inner surface layer [20, pp. 1, 45]. For high wind speeds, turbulence production may be assumed to be purely mechanical, that is, neutral atmospheric stability [46, p. 120]. The Reynolds shear stress can be treated as a constant in the inner surface layer [46, p. 119], and the velocity has a near logarithmic profile [62, p. 22]. The velocity profile by Richards and Hoxey [51] are based on the above assumptions, and used in this thesis.

$$\bar{u} = \frac{u_*}{\kappa} \ln \left(\frac{z + z_0}{z_0} \right) \quad (7.1)$$

The temperature profile for neutral atmospheric stability is decreasing upwards at the isentropic rate [46, p. 108]. Even though the temperature is slightly reduced with height, an isothermal assumption is used in the present simulations, which enables the problem to be solved without use of the energy equation.

The friction velocity in Eq. (7.1), is calculated from a reference velocity and height.

$$u_* = \frac{u_h \kappa}{\ln \left(\frac{h_{ref} + z_0}{z_0} \right)} \quad (7.2)$$

Where u_h is the velocity at a reference height h_{ref} , typically 10 m above the ground, and z_0 is the physical roughness length. The mean velocity in the lateral and vertical directions are zero, and the flow is not changing in the horizontal plane. Additionally, the viscous stress is negligible compared to the Reynolds stress. Based on these assumptions, a simple solution for k and ε from the standard k - ε formulation

may be derived [51].

$$k = \frac{u_*^2}{\sqrt{C_\mu}} \quad (7.3)$$

$$\varepsilon = \frac{u_*^3}{\kappa_{k\varepsilon}(z + z_0)} \quad (7.4)$$

Where $\kappa_{k\varepsilon}$ is the von Kármán constant calculated by the coefficients in the k - ε model.

$$\kappa_{k\varepsilon} = \sqrt{(C_{\varepsilon 2} - C_{\varepsilon 1})\sigma_\varepsilon \sqrt{C_\mu}} \quad (7.5)$$

With standard coefficients by Launder and Sharma [31], the solutions are as follows.

$$k = 3.33u_*^2 \quad (7.6)$$

$$\varepsilon = \frac{u_*^3}{0.433(z + z_0)} \quad (7.7)$$

The calculated $\kappa = 0.433$, derived from the coefficients of the standard k - ε formulation, is somewhat larger than typical estimates of the von Kármán constant, but this difference is unlikely to be too significant [52]. The profile for the turbulence energy may be a bigger problem. Measurements of the atmospheric boundary layer suggests that k is larger than $3.33u_*^2$ [51]. The Reynolds stress profiles for flat terrain provided by Panofsky and Dutton [46, p. 160] are given as follows.

$$\overline{u'u'} = (2.39u_*)^2 \quad (7.8a)$$

$$\overline{v'v'} = (1.92u_*)^2 \quad (7.8b)$$

$$\overline{w'w'} = (1.25u_*)^2 \quad (7.8c)$$

$$\overline{u'w'} = -u_*^2 \quad (7.8d)$$

$$k = \frac{1}{2} (\overline{u'u'} + \overline{v'v'} + \overline{w'w'}) = 5.48u_*^2 \quad (7.8e)$$

To satisfy Eq. (7.6), C_μ may be lowered to 0.033 in simulations of the atmospheric boundary layer [25, 37]. Keeping the other coefficients by their standard values gives $\kappa_{k\varepsilon} = 0.337$. Some accept this value, others change other coefficients as well in order to get a more realistic value for the von Kármán constant.

Another option is to use the standard values by Launder and Sharma [31] in the transport equations, and Eq. (7.6) at the inlet, equivalent to having $C_\mu = 0.033$ at the inlet and $C_\mu = 0.09$ in the domain. This setup may give decay of turbulence downstream of the inlet. The issue of decaying turbulence was addressed by Spalart and Rumsey [60] who suggested to add small source terms in the transport equations of the transport equations to counteract turbulence decay. Such source terms are added in the transport equations of the tested turbulence energy

transport models in STAR-CCM+, as seen in Section 4.

A set of coefficients that are consistent with the inlet conditions have been tested for the SKE model. Simulations with these coefficients are abbreviated SKE-A in the present simulations. The coefficients are given by Duynkerke [16], and were presented in Table 4.5. With $C_\mu = 0.033$, Eq. (7.3) is consistent with Eq. (7.8e). The von Karman constant based on these coefficients, Eq. (7.5), equals $\kappa_{k\varepsilon} = 0.40$. In addition to using this model in the helideck simulations, the SKE-A model was tested in the validation and verification simulations of Section 6. The intention behind doing these simulations with the SKE-A model was to see how the performance of a model changes when the coefficients are tuned. Even though the validation and verification simulations are internal flows without atmospheric boundary layer conditions, they contain flow phenomena that may be present in a helideck simulation, for instance separation, recirculation, stagnation, and reattachment. To know how an atmospheric boundary layer tuned model perform in such cases may be of importance if the model is to be used in helideck simulations.

Equation (7.8) is used to define turbulence quantities at the inlet in the simulations. The Reynolds stress transport models have been specified by the Reynolds stress components, while the turbulence energy transport models use the expression for k . The last Reynolds stress components, $\overline{u'v'}$ and $\overline{v'w'}$, are set equal to zero [37]. The dissipation rate and specific dissipation rate are calculated as follows.

$$\varepsilon = \frac{u_*^3}{\kappa(z + z_0)} \quad (7.9a)$$

$$\omega = \frac{u_*}{5.48\kappa(z + z_0)\beta^*} \quad (7.9b)$$

To investigate how the turbulence energy develops from the inlet, all turbulence models are tested in an empty domain simulation. The simulation setup is the same as for the rig simulations, explained in Section 7.2. Simplifications are done in the meshing process due to the absence of the rig, that is, there is not used volumetric controls to gradually refine the mesh close to the location of the rig. The mesh consists of cubical cells with lengths of 20 m in all directions, with a ten layer prism layer mesh close to the bottom surface in order to have a suitable value for z_{wall}^+ . This setup is the same as for the cells far from the rig in the main simulations.

The turbulence energy is measured 709 m downstream of the inlet, which corresponds to 50 m upstream of the helideck in the rig simulation with wind heading 090°. The resulting profiles are presented in Section 8.1.1. In brief, the turbulence energy profiles are found to be good enough maintained, and the standard coefficients of the turbulence models are therefore used unless else is pointed out.

Reference values are set in the helideck simulation domain. These values, presented in Table 7.1, are taken from the material database in STAR-CCM+ for air at atmospheric conditions. The temperature in the simulations is set to 285 K which

Table 7.1: Reference values in the helideck simulations.

p [kg m ⁻¹ s ⁻²]	μ [kg m ⁻¹ s ⁻¹]	M [kg mol ⁻¹]	R [kg m ² s ⁻² K ⁻¹ mol ⁻¹]
101 325	$1.855\,08 \times 10^{-5}$	$2.896\,64 \times 10^{-2}$	8.314 46

is a typical air temperature in the North Sea [6]. As mentioned in Section 3.1, density is calculated from the ideal gas law in the helideck simulations. By use of Eq. (3.4), the density in the helideck simulations is found to be approximately $\rho = 1.239 \text{ kg m}^{-3}$ with minor variations depending on the calculated pressure.

7.2 Rig model and simulation domain

A simple rig model is built with the 3D-CAD model tool in STAR-CCM+. The rig is based on data and pictures of an actual rig [17], but the construction is simplified. The rig data and pictures have been used in order to have some realistic values for scaling and sizing of the rig, the helideck, and other objects on the rig. All objects that are placed on the modeled rig are assumed to be hexahedrons in order to make the meshing process easier.

The modeled rig is approximately 120 m long and 85 m wide, with the top of the rig tower 130 m above the sea level. The top surface of the main deck is placed 42 m above the sea level and the top surface of the helideck is located at 48.1 m. The vertical component $z' = z - 48.1$ m is used in some figures in order to have the helideck at $z' = 0$.

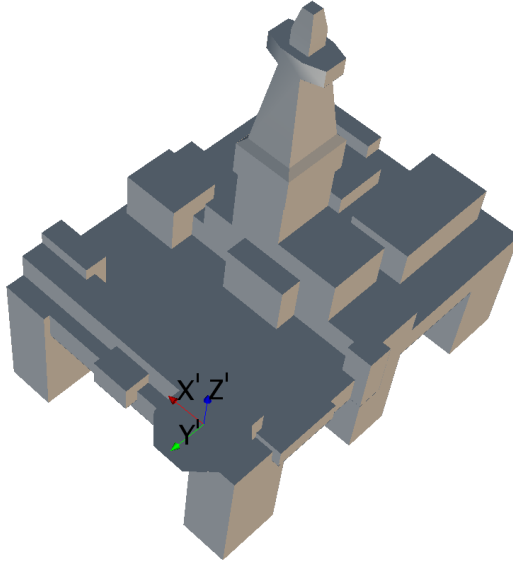


Figure 7.1: Rig model with helideck coordinate system.

Figure 7.1 shows the modeled rig with a coordinate system placed in the center of the helideck top surface. Four wind headings have been simulated, 000° , 090° , 180° , and 270° . North is defined in the y -direction, which means that the 000° wind heading is the most obstructed case. The 090° and 180° wind headings are unobstructed cases, while the 270° wind heading is a semi-obstructed case.

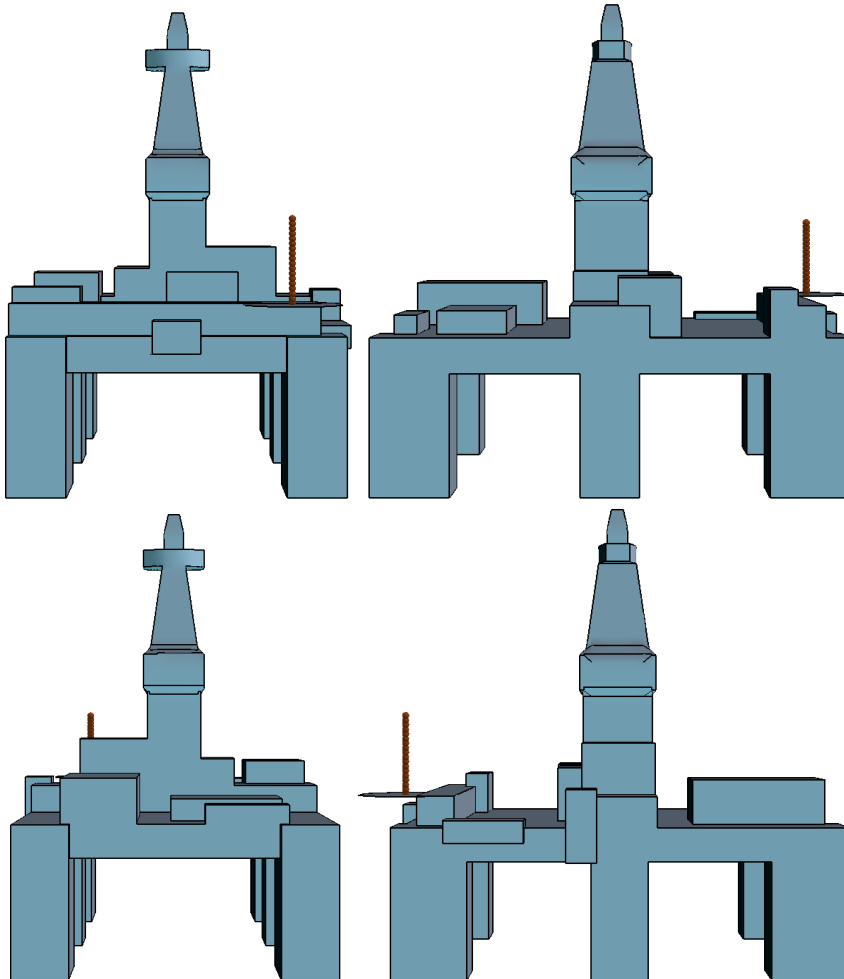


Figure 7.2: Rig seen from north (top left), east (top right), south (bottom left), and west (bottom right). The measurement line is marked with orange dots.

The helideck is partially placed on top of a cuboid box in the north-west corner of the rig, as seen in Figs. 7.1 and 7.2. NORSOK Standard C-004 [44] requires that an air gap beneath the landing area is provided when the helideck is placed above a building or solid structure. The air gap should be at least 2 m – 5 m high [44]. The present approach has been to place the helideck on the corner of the

rig with approximately 25 % of the helideck with 6 m of free air above the main deck, and approximately 50 % of the helideck above free air all the way down to the ocean. This seems to be in agreement with pictures of the actual rig [17]. The setup is likely to provide different results depending on the wind heading, and test the turbulence models in different scenarios.

Additional construction support below the helideck is neglected for easier meshing. This may cause less turbulence in the simulations compared to the real world, but the support consists mainly of thin pipes that are unlikely to induce major amounts of turbulence compared to the rest of the rig. As already mentioned, the purpose is not to make an exact copy of an actual rig, but to have some realistic values to use in the simulations.

The helideck is shaped like a regular octagon with lengths of 10 m, consistent with the rig data [17] and NORSOK Standard C-004 [44] which requires the minimum helideck size to be “*the maximum external dimension of the helicopter with both rotors rotating*” [44]. For a Sikorsky S-92, the maximum external dimension is 20.9 m [58], less than 24.1 m which is the medium diagonal of a regular octagon with the given lengths. Different helideck thicknesses were tested in simulations with the SKE model, but only minor differences in the standard deviation of vertical velocity component, turbulence energy, velocity magnitude, and mean vertical velocity component, above the helideck, were found between thicknesses of 0.1 m, 0.3 m, and 0.5 m. The first thickness resulted in a smoother mesh around the helideck, and was therefore used in the rest of the simulations.

Table 7.2: Boundary types used in helideck simulations. Details in Section 5.4.

Boundary	STAR-CCM+ boundary type
Inlet	Velocity inlet
Outlet	Pressure outlet
Domain side 1	Symmetry plane
Domain side 2	Symmetry plane
Ocean	Rough wall
Rig	Smooth wall

The rig is placed in the middle of a cuboid domain with dimensions $1600\text{ m} \times 1600\text{ m} \times 260\text{ m}$. This symmetric setup makes it easy to test different wind headings, by changing boundary conditions on the surfaces of the cuboid domain. Even though the inlet and symmetry boundaries could have been placed closer to the rig, the increase in cell number is small since the cells are large far from the rig. As seen in Table 7.2, the outlet is simulated with a pressure outlet boundary type. To avoid inflow from, and ensure an almost constant pressure on, the outlet boundary, the outlet should be placed far downstream of the rig, which is possible with this domain setup [7, p. 6270]. A test on the influence of the top boundary is done by performing simulations with heights of 500 m, but the 260 m height is found to be favorable and therefore used for the simulations.

The boundary conditions at the top boundary have also been investigated. There are different practices on how to model the top boundary in the literature [37, 52]. The use of a velocity inlet boundary type makes it possible to define the assumed atmospheric boundary layer conditions for velocity and turbulence quantities. This approach may be favorable in order to avoid turbulence decay and maintaining the inlet profiles. The differences between using a symmetry plane boundary type and a velocity inlet boundary type were found to be small, but the QPS model maintained the turbulence energy profile better when the latter was used, and thus the top boundary is modeled with a velocity inlet boundary type. The flow direction is set parallel to the flow, so the term velocity *inlet* may seem strange, but this is the name of the boundary type in STAR-CCM+, as explained in Section 5.4.1.

The bottom surface in the simulations, the ocean, is modeled as a rough wall. According to Charnock [8], the physical roughness length, z_0 , for flows over an ocean, is given as follows.

$$z_0 = \frac{\alpha_c}{g} u_*^2 \quad (7.10)$$

Charnock's parameter, α_c , may be assumed to be a constant, $\alpha_c = 0.0144$ [19]. Inserting the expression for u_* , Eq. (7.2), yields.

$$z_0 = \frac{\alpha_c}{g} \left(\frac{\kappa u_h}{\ln \left(\frac{h_{ref} + z_0}{z_0} \right)} \right)^2 \quad (7.11)$$

The simulated wind speed is $u_h = 10 \text{ m s}^{-1}$ at a reference height $h_{ref} = 10 \text{ m}$. For this wind speed, Eq. (7.11) gives $z_0 = 2 \times 10^{-4} \text{ m}$. This estimate is within the recommended roughness lengths provided by Panofsky and Dutton [46, p. 123].

When modeling surface roughness in STAR-CCM+, the equivalent sand-grain roughness, r_0 , is used. For an atmospheric boundary layer, r_0 is approximately 35 times the physical roughness length [7, p. 6320]. The equivalent roughness length, that is used in the simulations, is therefore $r_0 = 7 \times 10^{-3} \text{ m}$.

7.3 Mesh generation

The mesh is generated by use of the trimmed mesher, the surface remesher and the prism layer mesher in STAR-CCM+. The mesh around the rig is shown in Fig. 7.3. By use of volumetric controls, the mesh is gradually refined from large cells far from the rig to smaller cells close to the rig, thus increasing the accuracy of the calculations, while keeping the number of cells and calculation time at a satisfactory level. Base sizes of 20 m and 40 m have been used far from the rig, with refinements closer to the rig. The refinements are given as percentages of the base size, such that typical lengths for the cells closer to the rig are 10 m, 5 m, 2.5 m, and 1.25 m.

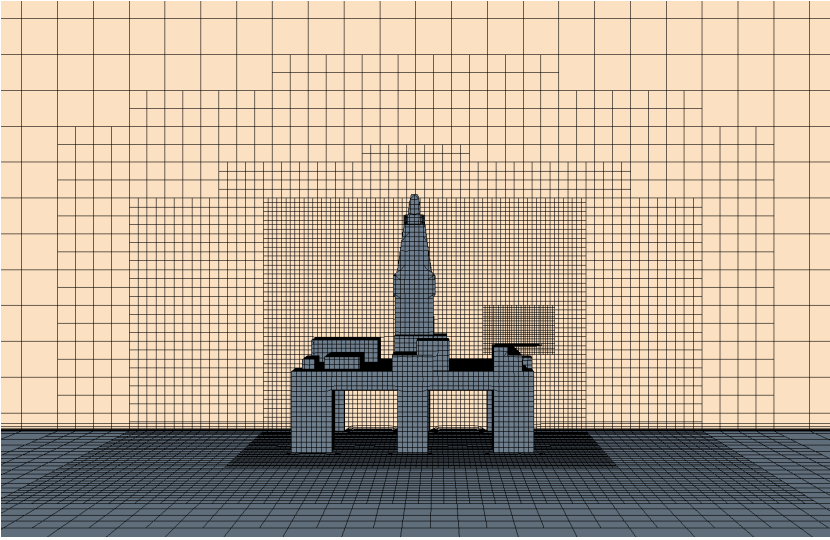


Figure 7.3: Mesh with 624 960 cells. The yellow “wall” is a plane section through the center of the helideck.

Three different mesh resolutions are tested to investigate mesh dependence. The details for the meshes are presented in Table 7.3. The three meshes have the same structure, but the cells are generally smaller and the area around the rig is further refined in the finer meshes. The third column of Table 7.3, “Around rig”, gives the base size of the volumetric control 50 m – 70 m from the rig. The next column, “Close to rig”, gives the base size in the volumetric control 10 m – 30 m from the rig, while the last column, “Helideck”, contains base sizes in the helideck measurement region. The coarsest mesh consists of 152 625 cells. This mesh has a base size far from the rig of 40 m. The second mesh, which near rig region is presented in Fig. 7.3, has a base size of 20 m far from the rig and the same relative refinement around the rig as the coarsest mesh. This gives a total of 624 960 cells. The finest mesh uses the same base size of 20 m far from the rig, but the cells are further refined near the rig, which increases the cell count to 3 096 528. The cells in the helideck measurement region have lengths of 1.25 m with all three meshes.

Table 7.3: Mesh details with cell sizes in volumetric controls.

Cells	Base size	Around rig	Close to rig	Helideck
152 625	40 m	10 m	5 m	1.25 m
624 960	20 m	5 m	2.5 m	1.25 m
3 096 528	20 m	2.5 m	1.25 m	1.25 m

The prism layer mesher is used to get suitable heights for the cells close to the wall boundaries. A ten layer prism layer is used above the bottom surface, the ocean,

while a five layer prism layer is used above the rig surface, both shown in Fig. 7.4. The number of prism layers differ since the bottom surface covers the ocean which generally have larger cells than the ones found close to the rig.

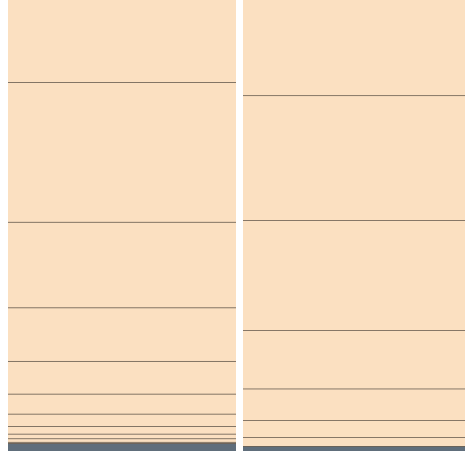


Figure 7.4: Prism layer mesh above the ocean for $0 \leq z \leq 5$ m (left) and above the helideck for $0 \leq z' \leq 1$ m (right).

As mentioned in Section 5.4, the first cell adjacent to a wall boundary should have a node height of $30 \leq z^+ \leq 500-1000$. The bottom surface has some additional constraints due to the use of roughness on this surface. Guidelines in the STAR-CCM+ documentation recommends that the first cell should be higher than $0.4r_0$ and higher or equal $20z_0$ [7, p. 6323]. Both prism layers have a first cell height of 0.02 m which satisfy these recommendations. For the ocean surface, the prism layer height corresponded to $z^+ \approx 250-300$, while the helideck was found to have $z^+ \approx 300-500$, with some variations between different wind headings and turbulence models.

7.4 STAR-CCM+ field functions

Like in the validation and verification simulations, the variance of the vertical velocity component is found with a user field function.

```
ww3DidealGas = 2/3*$TurbulentKineticEnergy
-2*$TurbulentViscosity/$Density*$$W_VelocityGrad [2]
+2/3*$TurbulentViscosity/$Density*($$U_VelocityGrad [0]
+$$V_VelocityGrad [1]+$$W_VelocityGrad [2])
```

As mentioned in Section 3.1, the density is a function of the pressure in the helideck simulations. The last term of Eq. (4.17) is therefore included in the field function. However, the pressure variations are small compared to the reference atmospheric

pressure and this term is negligible and can be ignored. The importance of the second term, the strain rate term, is discussed in Section 8.2.2.

User field functions are also used to define boundary conditions for the inlet and top of the domain, as well as roughness on the bottom domain. Field functions are used to define the boundary conditions from Eqs. (7.1), (7.2), (7.8), and (7.9). The constants in the equations are defined as follows.

$$\text{\$kappa} = 0.41$$

$$\text{\$z0} = 0.0002$$

$$\text{\$h} = 10$$

$$\text{\$uh} = 10$$

$$\text{\$betas} = 0.09$$

The following functions are calculated from the defined constants. Notice that $\log(a)$ is an inbuilt field function for the natural logarithm of the number a , while $\text{\$Centroid}[2]$ returns the vertical component.

$$\text{\$r0} = 35 * \text{\$z0}$$

$$\text{\$lnz} = \log((\text{\$Centroid}[2] + \text{\$z0}) / \text{\$z0})$$

$$\text{\$lnh} = \log((\text{\$h} + \text{\$z0}) / \text{\$z0})$$

The friction velocity is then defined as follows.

$$\text{\$ustar} = \text{\$kappa} * \text{\$uh} / \text{\$lnh}$$

Which makes it possible to calculate the other quantities needed. Here $\text{pow}(a,b)$ is used to raise a to the power b .

$$\text{\$u} = \text{\$ustar} / \text{\$kappa} * \text{\$lnz}$$

$$\text{\$uu} = \text{pow}((2.39 * \text{\$ustar}), 2)$$

$$\text{\$vv} = \text{pow}((1.92 * \text{\$ustar}), 2)$$

$$\text{\$ww} = \text{pow}((1.25 * \text{\$ustar}), 2)$$

$$\text{\$uw} = -\text{pow}(\text{\$ustar}, 2)$$

$$k = 0.5 * (u_u + v_v + w_w)$$

$$\epsilon = \text{pow}(u_{\text{star}}, 3) / (\kappa * (\text{Centroid}[2] + z_0))$$

$$\omega = \epsilon / (k * \beta_s)$$

8 Helideck simulation results

Results from the helideck simulations are given in this section. Initial sensitivity tests are presented in Section 8.1. The development of the turbulence energy and Reynolds stress profiles, influence on different top boundary conditions, and mesh dependence have been investigated. The final helideck results are presented in Section 8.2. Four wind headings are simulated with the turbulence models presented in Section 4.

8.1 Initial sensitivity tests

8.1.1 Turbulence energy development

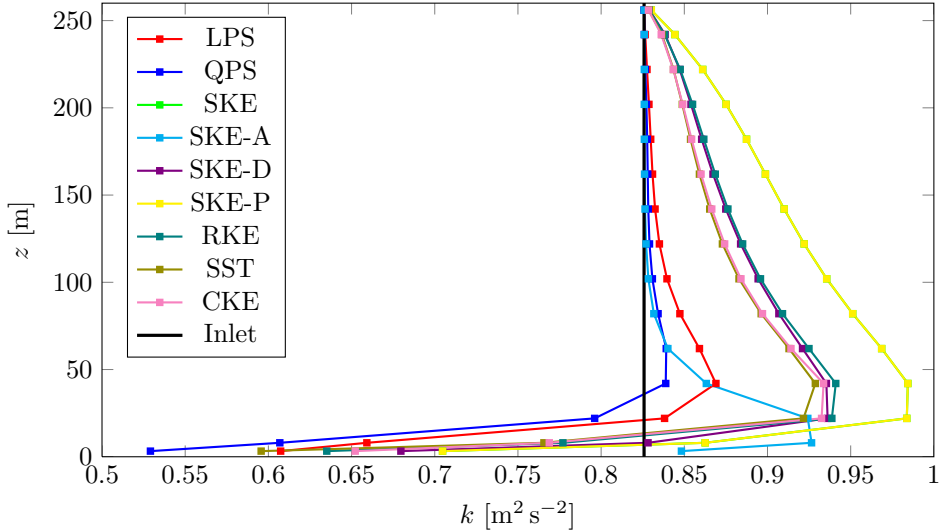


Figure 8.1: Turbulence energy 709 m downstream of the inlet in an empty domain.

As mentioned in Section 7.1, the turbulence profiles may change downstream of the inlet due to inconsistency between the inlet conditions and the turbulence models. To investigate how the turbulence models develop from the inlet conditions, the

turbulence energy profiles are compared with the inlet turbulence energy profile in an empty domain and a rig simulation 709 m downstream of the inlet, which corresponds to 50 m upstream of the helideck in the 090° wind heading simulation. Figure 8.1 shows the turbulence energy in the empty domain simulations. A decay of turbulence energy is not found. Instead, all models increase their turbulence energy profiles. The most prominent increases are found with the SKE and SKE-P models, while the Reynolds stress transport models are least affected. The small source terms that are added in STAR-CCM+ to counteract turbulence decay are found in the transport equations for all turbulence energy transport models, but not for the Reynolds stress transport models. These source terms may explain why the turbulence energy transport models increase their turbulence energy profiles more than the Reynolds stress transport models. The use of coefficients that satisfy atmospheric boundary layer conditions in the SKE-A model results in a better maintained turbulence energy profile.

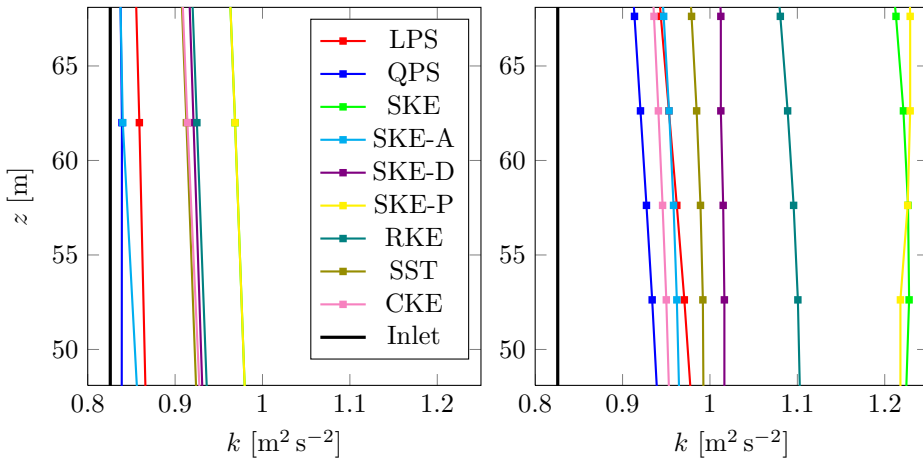


Figure 8.2: Turbulence energy 709 m downstream of the inlet (50 m upstream of the helideck), in the helideck measurement region, in an empty domain (left) and in the simulations with the rig (right).

A comparison of the turbulence energy profiles in the empty domain simulations and the 090° wind heading rig simulation, is given in Fig. 8.2. The turbulence energy 709 m downstream of the inlet is presented for the helicopter measurement region, $48.1 \text{ m} \leq z \leq 68.1 \text{ m}$. The figure shows that the presence of the rig is noticeable 50 m upstream of the rig, especially for the SKE, SKE-P, and RKE models. The SKE-D model does not get the same relative increase in turbulence energy, which suggests that the SKE, SKE-P, and RKE models may have some stagnation point issues with this wind heading. Using the value from Park and Park [48] for the realizability constraint, $C_T = 2$, in the SKE-P model, gives negligible differences compared to the SKE model this far upstream. The turbulence energy profiles in the empty domain simulations are identical for these two models.

8.1.2 Reynolds stress development

The development of the non-zero Reynolds stresses at the inlet, $\overline{u'u'}$, $\overline{v'v'}$, $\overline{w'w'}$, and $\overline{u'w'}$, are investigated for the two Reynolds stress transport models. The profiles 709 m downstream of the inlet in an empty domain is presented in Fig. 8.3. The red lines are the results of the LPS model, while the blue lines represent the QPS model. The inlet Reynolds stress profiles are indicated with black lines.

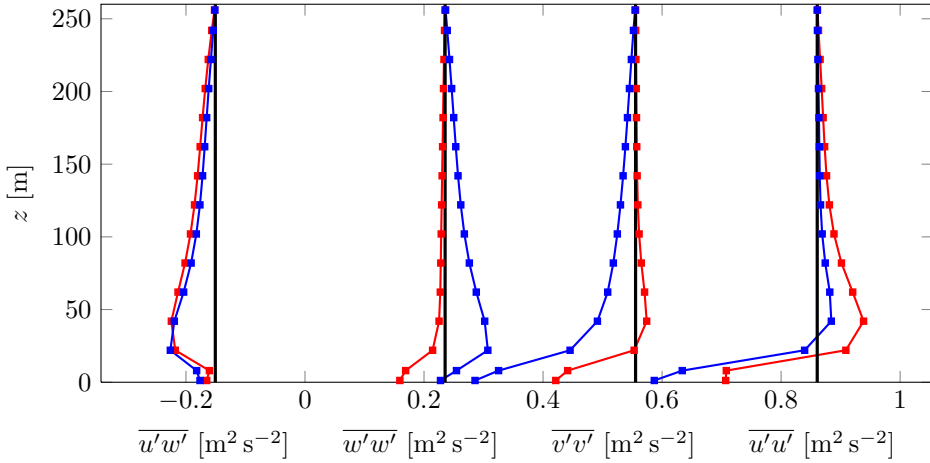


Figure 8.3: Reynolds stress development in an empty domain 709 m downstream of the inlet with the LPS (red) and QPS (blue) models compared to the inlet conditions (black).

Some of the Reynolds stress components change significantly from the inlet, as seen in Fig. 8.3. The streamwise-vertical Reynolds shear stress, $\overline{u'w'}$, decreases similarly for both the LPS and QPS models, while the development of the normal Reynolds stress components differ between the two models. The streamwise Reynolds stress component profiles develop similarly to the turbulence energy profiles, seen in Fig. 8.1. The vertical Reynolds stress component, that is used in the NORSOK criteria [44], is best maintained with the LPS model which gives a minor underestimation 709 m downstream of the inlet. The QPS model, on the other hand, has a significant increase in the vertical Reynolds stress component, which is compensated by a decrease in the lateral Reynolds stress component.

The main difference between the two Reynolds stress transport models is the modeling of the pressure-strain term. The pressure-strain term redistributes energy between the Reynolds stress components [50, p. 316]. The LPS model may be more appropriate for these helideck simulations, as it better maintains the atmospheric distribution between the normal Reynolds stress components. The streamwise Reynolds stress component and the turbulence energy are best maintained with the QPS model, but this model seems to even out the differences between the lateral and vertical Reynolds stress components in the present simulations.

8.1.3 Top boundary conditions

Placement and type of conditions on the top boundary of the domain have been investigated. A symmetry boundary type and a velocity inlet boundary type have been tested with two different domain heights. The least and the most affected turbulence models from the inlet turbulence energy development test, see Fig. 8.1, are presented with different heights and top boundary conditions in Fig. 8.4. The QPS model was found to be the model with least variations in the turbulence energy profile from the inlet, while the turbulence energy profile changed the most from the inlet with the SKE model. These two models have been tested in simulations with a 260 m domain height and a 500 m domain height. Use of a symmetry boundary type on the top boundary is indicated by a S, while the velocity inlet boundary type is indicated by a V.

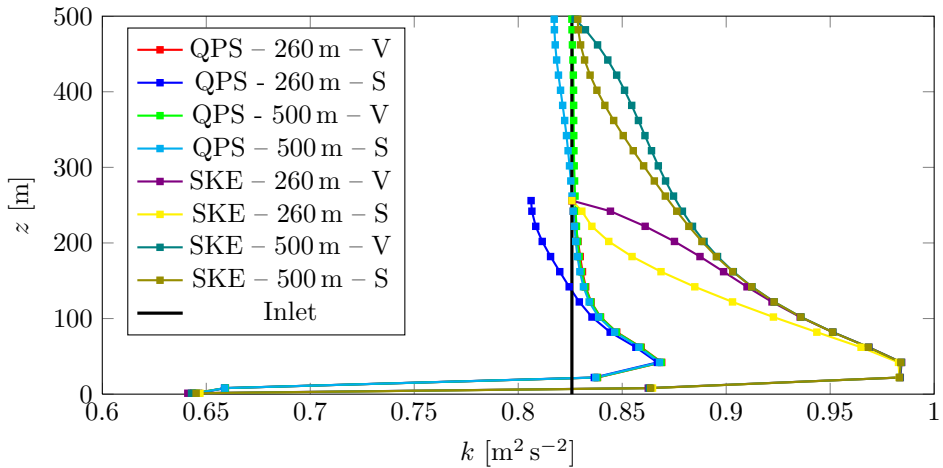


Figure 8.4: Turbulence energy in empty domain 709 m downstream of inlet with different top boundaries (V: Velocity inlet. S: Symmetry plane).

On the basis of the top boundary conditions test, the domain height is set to 260 m and a velocity inlet boundary type is used on the top boundary. Although the SKE model is somewhat better when the symmetric boundary type is used, this setup gives the best maintained turbulence energy profile for the QPS model. The symmetry boundary type gives some turbulence decay for this model. Using fixed values on the top boundary may therefore maintain the inlet profiles better for models that experience turbulence decay.

The difference between a 260 m height and a 500 m height is negligible in the region of interest for both models. The 260 m height is considered high enough to not affect the flow above the helideck. A plane section through the tower of the rig, illustrating the turbulence energy with the SKE model in the 000° wind heading, is presented in Fig. 8.5. This wind heading is the most obstructed case and the SKE model is the model that is found to be most affected by excessive

turbulence energy in stagnation regions. Setting a boundary height based on this figure should therefore be conservative. Figure 8.5 suggests that the 260 m height may be high enough, but also indicates that the height should not be much reduced, in order to avoid too large gradients close to the top boundary. A shift in color from the darkest blue color that represents the free stream turbulence energy value, to a lighter blue color is found approximately 30 m from the top boundary above the rig in Fig. 8.5. Simulations with heights lower than 260 m were therefore not tested.

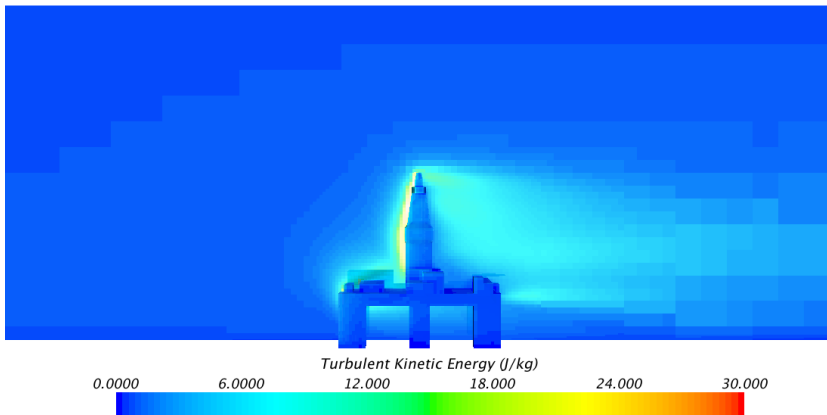


Figure 8.5: Turbulence energy in a plane section through the tower of the rig for the 000° wind heading with the SKE model.

There may be some benefits of choosing the 260 m domain height. It needs less cells, which means less calculation time, than a domain with a height of 500 m. Furthermore, some of the assumptions used in the simulations may be more correct with a lower domain. As mentioned in Section 7.1, the domain is assumed to be isothermal, although the temperature decreases slightly as a function of height close to the surface of the Earth. A logarithmic velocity profile has also been used, but a power-law velocity profile may be better suited deeper into the atmospheric boundary layer [28]. Both a variable temperature profile and a power-law velocity profile, as well as other extensions to the present problem, like buoyancy induced turbulence, could have been interesting to investigate further, but such extensions have not been tested due to time and resource limitations.

8.1.4 Mesh dependence

Three different meshes are tested to investigate mesh dependence by evaluating the turbulence energy in the 090° wind heading. Six turbulence models have been tested and the results are presented in Fig. 8.6.

Figure 8.6 shows some differences between the meshes for all turbulence models. The simulations with the coarsest mesh have larger peak values than the simulations

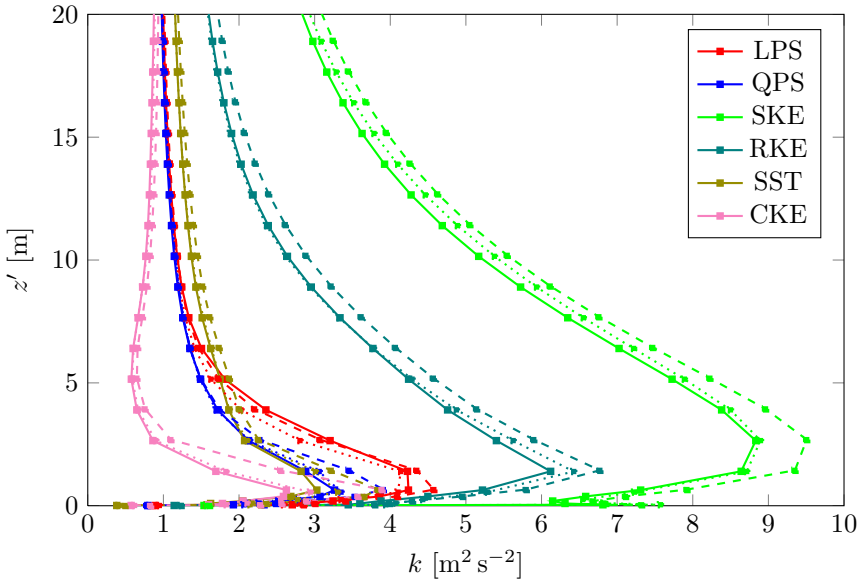


Figure 8.6: Turbulence energy above helideck for wind heading 090° . Dashed lines: 152 625 cells. Solid lines: 624 960 cells. Dotted lines: 3 096 528 cells.

with the two finer meshes. The values in the free stream high above the helideck are also somewhat larger with the coarsest mesh than with the finer meshes. The differences between the second finest and the finest mesh are not that significant.

The calculated turbulence energy profiles decrease for all turbulence models when the mesh is refined. The CKE model has a relatively large peak in turbulence energy close to the helideck with the coarsest mesh compared to the finer meshes. This model uses the same transport equations as the SKE model which is also found to be somewhat more mesh dependent than other models. However, the differences are small, and the other extensions to the SKE model (SKE-A, SKE-D, SKE-P) were therefore not tested.

The 090° wind heading was the first wind heading that was simulated, and the mesh dependence test was therefore done for this wind heading. Based on Fig. 8.6, the second finest mesh was chosen for the simulations. However, the 090° wind heading is an unobstructed wind heading, and may be less influenced by mesh refinements than the more obstructed wind headings. To get some estimation of the error in choosing this mesh for more obstructed wind headings, the RKE model, which was found to be among the fastest models, was tested for the other wind headings as well.

The turbulence energy profiles for the three meshes with the RKE model are presented in Fig. 8.7. The 000° wind heading is found to be more mesh dependent than the other wind headings. The turbulence energy profiles have the same shape,

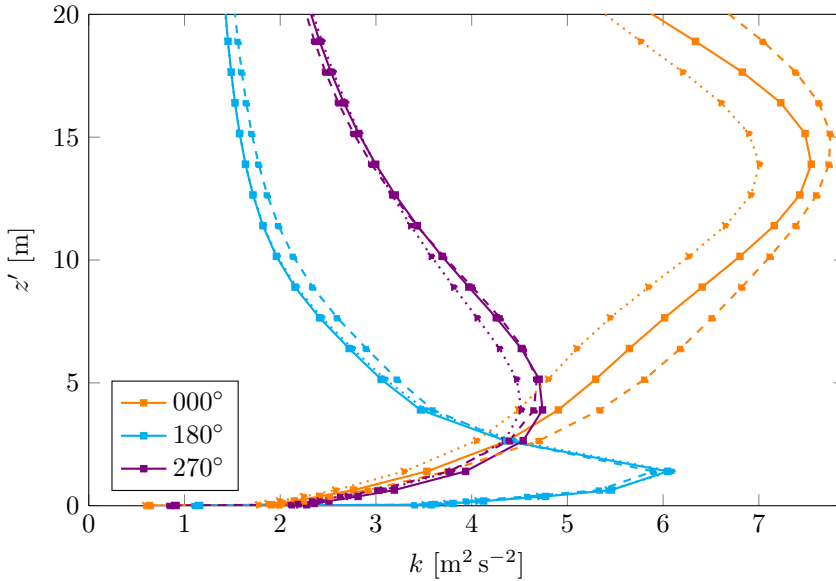


Figure 8.7: Turbulence energy above the helideck with the RKE model for the second finest (624 960 cells) and finest mesh (3 096 528 cells).

but differ in magnitude. The profile with the second finest mesh has, on average, 9 % larger values than the finest mesh, while the coarsest mesh has 16 % larger values than the finest mesh. The semi-obstructed wind heading, 270° , shows some mesh dependence, while the differences between the two finest meshes in the 180° wind heading are hardly visible.

The second finest mesh is used for the 090° , 180° , and 270° wind headings, while the finest mesh is used for the obstructed wind heading, 000° . Use of the finest mesh in the simulations for the 000° gave a considerable time penalty. Further testing, with even finer meshes and in simulations with other turbulence models, are therefore not done. The increase in calculation time is also the reason why the second finest mesh is used in the 270° wind heading. Nevertheless, based on the results presented in Figs. 8.6 and 8.7, the present approach is considered a reasonable compromise between calculation time and accuracy.

A specific look at the prism layer mesh above the helideck was done for the 090° wind heading. The QPS, SKE, and SST models were tested for different near wall prism layer heights. This is the nearest cell above the helideck, hence z_{wall}^+ is determined from the height of this cell. Although z_{wall}^+ varied from $z_{wall}^+ \approx 100$ to $z_{wall}^+ \approx 3000$, there was no visible differences in the turbulence energy profiles. The mesh with a near wall prism layer height of $z = 0.02$ m, $z_{wall}^+ \approx 300 - 500$, was used for the rest of the simulations, as this prism layer mesh had the smoothest transition to the outer cells.

8.2 Helideck analysis

The helideck simulation results are presented in this section. According to NORSOK Standard C-004 [44], a helideck analysis should contain plots of the standard deviation of the vertical velocity component, the velocity magnitude, and the vertical velocity component. In addition, plots of the turbulence energy profiles are presented since criteria on k were proposed in Section 2.3. The four quantities are all measured above the center of the helideck, from the first cell above the helideck to 20 m above the helideck, that is, $0 < z' \leq 20$ m.

Four different wind headings are simulated. The first wind heading, 000° , represents an obstructed case where the wind field flows over obstacles on the rig before approaching the helideck. The second and third wind headings, 090° and 180° , are unobstructed cases where the wind field flows over the helideck before other structures on the rig. The last wind heading, 270° , is a semi-obstructed case with minor obstacles before the helideck.

Turbulence and velocity profiles are given in Figs. 8.8-8.11. The differences between turbulence models are most visible in the turbulence plots, while the velocity profiles are of the same shape and magnitude with most models for several wind headings. This is especially true for the unobstructed wind headings, while wind heading 000° , the most obstructed case, is found to differ more between different turbulence models in calculations of the velocities.

As was found for the validation and verification simulations of Section 6, the turbulence timescale constraint by Park and Park [48] does not radically change the SKE model. The results with the SKE-P model are therefore similar to the results with the SKE model. The SKE-D and SST models, which use the same value for the turbulence timescale constraint, $C_T = 0.6$, are similar in all wind headings.

Wind heading 000° is presented in Fig. 8.8. The shape of the turbulence profiles for the Reynolds stress transport models are similar, they increase almost linearly as a function of the height above the helideck. The QPS model continue to increase in both turbulence plots, while the values with the LPS model decreases from $z' = 15$ m. The turbulence profiles with the CKE model are similarly shaped as the profiles with the QPS model, but the values are slightly larger. The SKE, RKE, and SKE-P models have profiles of approximately the same shape as the LPS model, with decreasing values from approximately $z' = 15$ m. The SST and SKE-D models have more curved profiles than the other models, which may be related to triggering of the turbulence timescale constraint. All models violate the “noticeable turbulence” criterion in NORSOK Standard C-004, and the SKE, SKE-A, and CKE models violate the “flight limitations” criterion as well. The proposed criteria on k give almost the same results, but these criteria are found to be less restrictive than the criteria on w_{rms} since the SKE-A model is the only model that violates the proposed flight limitations criterion.

Significant differences between the models are found in the velocity plots of wind heading 000° . The QPS and CKE models, which had similarly shaped turbulence

profiles, calculate similar velocity profiles as well. These models predict almost zero vertical velocity component profiles for the whole measurement region, and smaller velocity magnitude profiles than the other models. The LPS, SKE-D, and SST models, on the other hand, calculate larger velocity magnitude profiles and smaller values for the vertical velocity component. The velocity profiles are similar for the SKE, SKE-P, and RKE models. Their calculations for the vertical velocity component are between the QPS and CKE models, and the LPS, SKE-D, and SST models. The SKE-A model is found close to the QPS and CKE models in the lowest part of the measurement region for the velocity magnitude, and with larger values in the upper half. The vertical velocity component profile of the SKE-A model is similar to the profiles of the QPS and CKE models throughout the measurement region.

Wind heading 090° and 180° , presented in Figs. 8.9 and 8.10, represent unobstructed cases. Since the helideck is symmetric and the measurements are done above the center of the helideck, these two wind headings have almost equal results. The velocity plots are similar for all models in these wind headings. The vertical velocity component profiles are negative close to the helideck and become positive around $z' = 4$ and $z' = 6$ for wind heading 090° and 180° , respectively. The magnitudes of the vertical velocity component profiles differ significantly between different models. A two-group pattern where the SKE, SKE-P, and SKE-A models are found with smaller peak values than the SST, SKE-D, QPS, CKE, and LPS models, can be seen in Figs. 8.9 and 8.10. The profile for the RKE model is found between the two groups.

The two-group pattern is found in the velocity magnitude and turbulence plots as well. In the turbulence plots, the first group (SKE, SKE-P, SKE-A) have larger turbulence values, w_{rms} and k , than the second group. In the velocity magnitude plots, the models in the second group have steeper gradients close to the helideck. The turbulence criteria are not violated by the models in the second group at these wind headings. In the first group, all models violate the “noticeable turbulence” criterion on w_{rms} and corresponding criterion on k . The SKE-A model violates the “flight limitations” criterion on w_{rms} in the 090° wind heading. The RKE model is again found between the two groups, violating the “noticeable turbulence” criterion on w_{rms} , but not on k . As in wind heading 000° , the proposed criteria on k are found less restrictive than the criteria on w_{rms} .

The constitutive relation in the CKE model is found to give negative values for the variance of the vertical velocity component for wind heading 090° , 180° , and 270° as shown in Figs. 8.9-8.11. These unphysical results illustrate that the CKE model is not a realizable turbulence model. The SKE-A model has a negative value in one of the cells in the 180° wind heading, as seen in Fig. 8.10. Although the variance of the vertical velocity component profiles are found with negative values for the CKE and SKE-A models, the turbulence energy profiles are seemingly not much affected.

Plots for wind heading 270° are presented in Fig. 8.11. The 270° case is more

similar to the unobstructed cases than the obstructed case. The two-group pattern found with wind heading 090° and 180° is also visible for this wind heading. In the turbulence plots, the SKE-A, SKE, SKE-P, and RKE models have larger magnitudes than the other models. Their profiles are almost identically shaped in both turbulence plots. The same is found for the second group of models, but the CKE model differ from the pattern due to its unrealizable variance. Six models, SKE-A, SKE, SKE-D, RKE, SST, and CKE, violate the “*noticeable turbulence*” criterion on w_{rms} , while the proposed corresponding criterion on k is violated only by the SKE-A model.

The models are again divided in two groups in the velocity plots, where the smallest vertical velocities are found with the SST, SKE-D, QPS, CKE, and LPS models, peaking at $\bar{w} \approx -1.4 \text{ m s}^{-1}$, while the vertical velocities peak at $\bar{w} \approx -0.5 \text{ m s}^{-1}$ with the other models. The relative differences are smaller in the velocity magnitude plots, but the two-group pattern is found here as well.

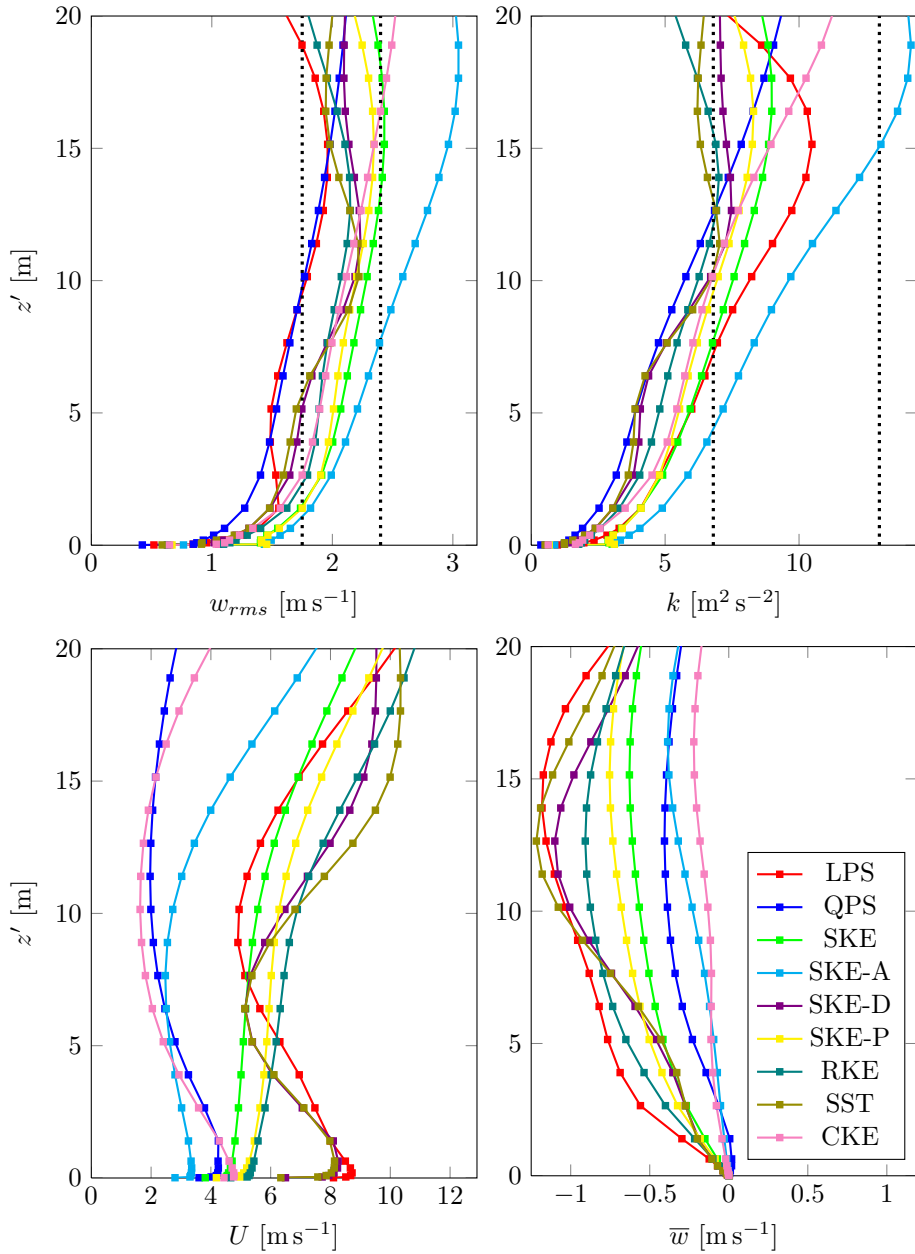


Figure 8.8: Helideck results for wind heading 000°. Dashed lines: NORSEK criteria on w_{rms} [44] and proposed criteria on k from Eq. (2.8).

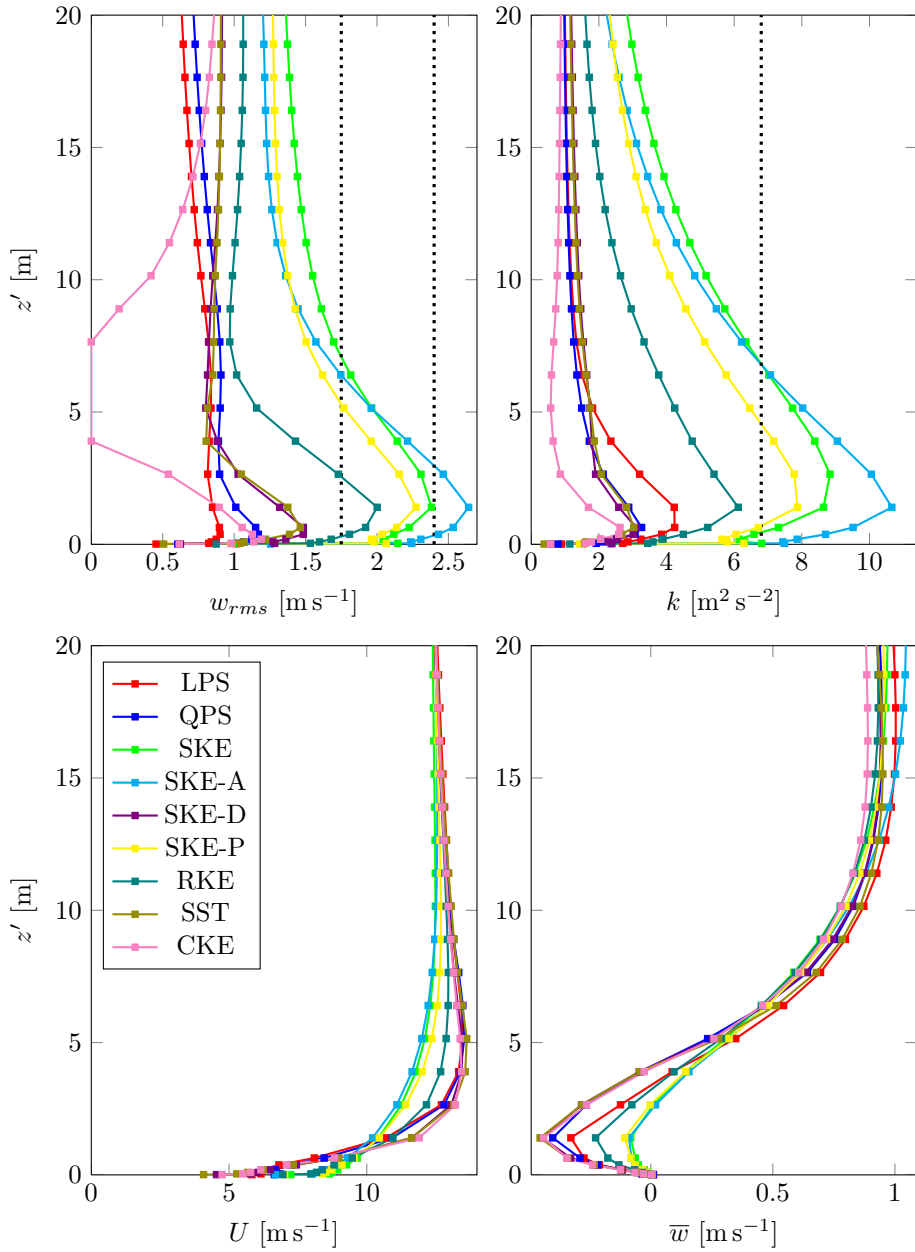


Figure 8.9: Helideck results for wind heading 090° . Dashed lines: NORSEK criteria on w_{rms} [44] and proposed criteria on k from Eq. (2.8).

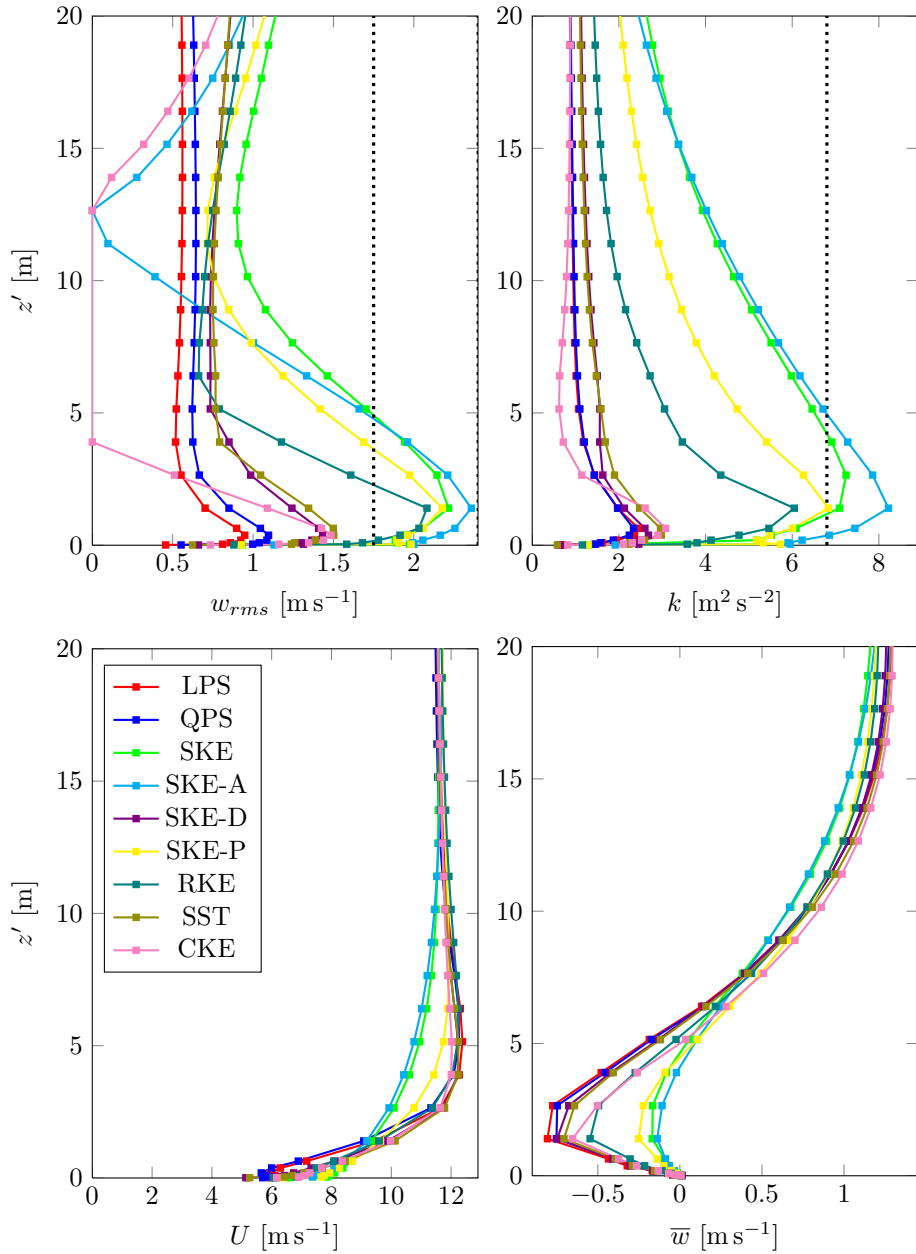


Figure 8.10: Helideck results for wind heading 180° . Dashed lines: NORSEK criteria on w_{rms} [44] and proposed criteria on k from Eq. (2.8).

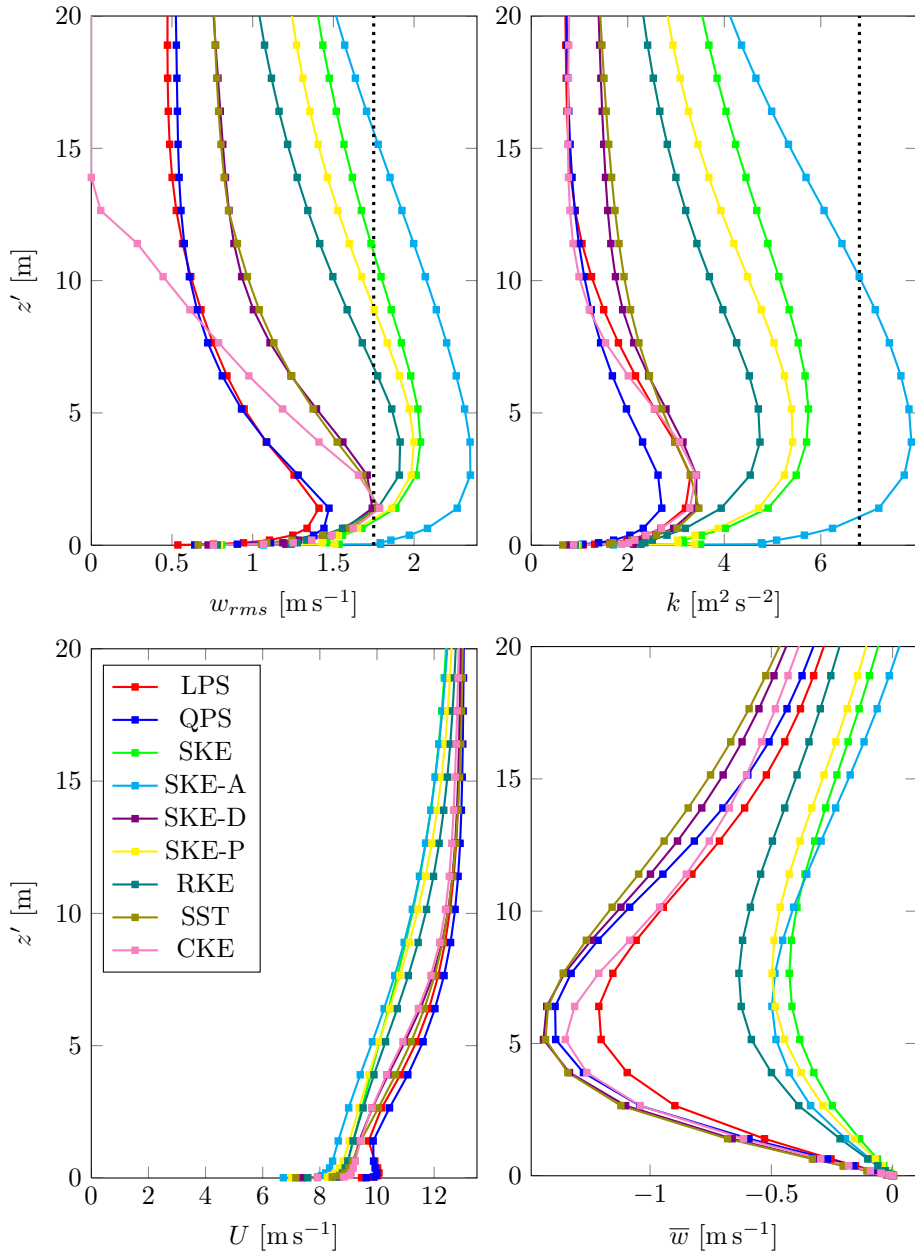


Figure 8.11: Helideck results for wind heading 270° . Dashed lines: NOROSOK criteria on w_{rms} [44] and proposed criteria on k from Eq. (2.8).

A summary of the turbulence plots, with maximum values for w_{rms} and k , is given in Table 8.1. Blue text color represents violation of the noticeable turbulence criterion in NORSOK Standard C-004 [44], and proposed corresponding criterion on turbulence energy from Section 2.3, while red color indicates violation of the flight limitations criteria.

Table 8.1: Maximum w_{rms} [m s^{-1}] and k [$\text{m}^2 \text{s}^{-2}$] in the helideck simulations. “Noticeable turbulence” (blue) and “flight limitations” (red) from Eqs. (2.1) and (2.8).

	000°		090°		180°		270°	
	w_{rms}	k	w_{rms}	k	w_{rms}	k	w_{rms}	k
LPS	1.96	10.48	0.90	4.24	0.95	2.45	1.41	3.30
QPS	2.12	9.37	1.17	3.26	1.10	2.34	1.47	2.71
SKE	2.43	8.98	2.38	8.83	2.22	7.24	2.04	5.74
SKE-A	3.05	14.18	2.64	10.66	2.36	8.22	2.35	7.88
SKE-D	2.23	7.48	1.48	3.10	1.43	2.68	1.74	3.42
SKE-P	2.35	8.30	2.27	7.87	2.18	6.84	2.00	5.42
RKE	2.15	7.01	2.00	6.12	2.08	6.05	1.91	4.74
SST	2.22	7.04	1.46	3.03	1.50	2.98	1.78	3.47
CKE	2.53	11.28	1.19	2.63	1.48	3.08	1.79	3.42

The maximum values for the standard deviation of the vertical velocity component are higher with all turbulence energy transport models than the Reynolds stress transport models. The calculated maximum turbulence energy values are more similar between the two model types. Between the two Reynolds stress transport models, the differences in calculations of the turbulence energy are smaller than the differences in calculations of the variance of the vertical velocity component. Compared to the average of the two models, the relative differences in $\overline{w'w'}$ are 8 %, 25 %, 14 %, and 4 % for the four wind headings. The corresponding differences in k are 6 %, 13 %, 2 %, and 10 %. As mentioned in Section 2.3, a sensible comparison should be between the turbulence energy and the variance, not the standard deviation, of the vertical velocity component since these quantities have the same units.

8.2.1 Durbin’s realizability constraint

The results for the SKE model are found to differ significantly with and without the turbulence timescale constraint by Durbin [15]. The calculated turbulence energy upstream of the helideck in the 180° wind heading, with and without the constraint activated, is presented in Fig. 8.12. The same color scale, divided in 100 colors from blue to red, is used in both figures.

The right edge of the figures corresponds to approximately 100 m upstream of the helideck. In the simulation with the SKE model, the stagnation region close to the

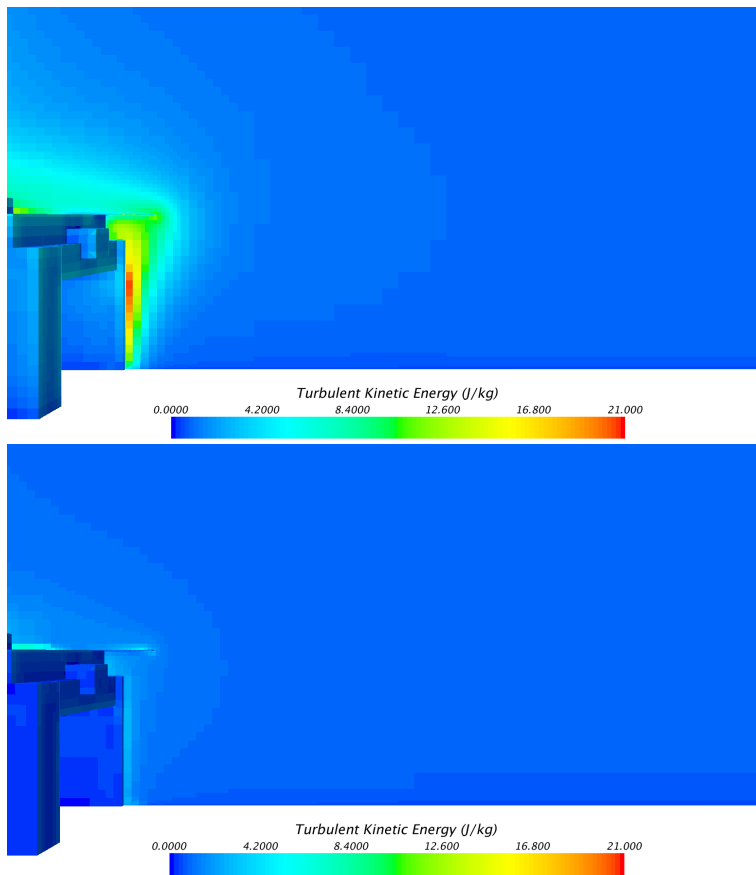


Figure 8.12: Turbulence energy upstream of the helideck for the 180° wind heading without (top) and with (bottom) Durbin's realizability constraint activated, $C_T = 0.6$, in the SKE model.

rig is felt earlier compared to the simulation with the turbulence timescale constraint activated. The first shift in color is found approximately 50 m upstream of the helideck with the SKE model, while the same increase is found approximately 10 m upstream of the helideck with the SKE-D model. The turbulence energy increases to higher values in the simulation without the turbulence timescale constraint, which gives significantly higher turbulence energy in the helideck approach area.

8.2.2 Relation between vertical variance and turbulence energy

The proposed turbulence criteria on k , presented in Section 2.3, correspond to $\overline{w'w'} = 0.45k$ for the wind tunnel measurements given in CAA Paper 2004/03 [66, App. T]. The relations between $\overline{w'w'}$ and k for the helideck simulations are presented in Fig. 8.13.

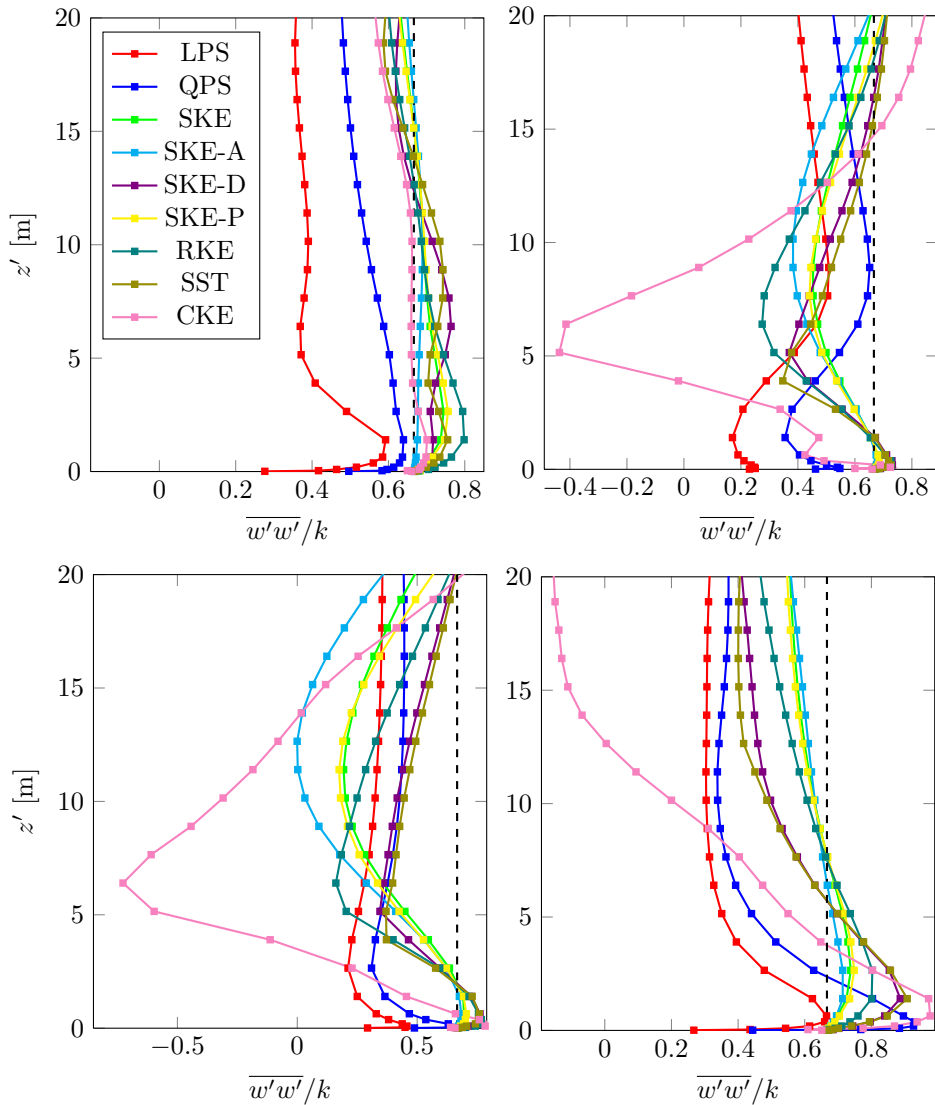


Figure 8.13: $\overline{w'w'}/k$ in 000° (upper left), 090° (upper right), 180° (bottom left), and 270° (bottom right). Dashed lines: Isotropic assumption $\overline{w'w'} = \frac{2}{3}k$.

There are significant differences between the Reynolds stress transport models and the turbulence energy transport models in the 000° wind heading. Both Reynolds stress transport models have smaller relations between $\overline{w'w'}$ and k , compared to the turbulence energy transport models, in the whole measurement region. There are also differences between the two Reynolds stress transport models, where the LPS model has a significantly smaller relation than the QPS model. The turbulence energy transport models are found to provide similar results, with somewhat larger relations than the isotropic assumption in the lowest part of the measurement region, and smaller relations in the upper part.

The two unobstructed cases, 090° and 180° , have similar average relations for all models (except CKE) with a value of $\overline{w'w'} \approx 0.5k$. Since the CKE model calculates negative variances of the vertical velocity component for some cells in the measurement region, the relation becomes negative in both plots for the corresponding cells. The Reynolds stress transport models have similar profiles, but the values calculated with the LPS model are again smaller than with the QPS model. The relation differences between the two model types are smaller than for the obstructed wind heading. The shape of the profiles are however different, where the Reynolds stress transport models curve in opposite direction compared to the turbulence energy transport models.

There are differences between the two model types in wind heading 270° , but not as significant as in the obstructed wind heading. The CKE model is again found to be different from the rest of the models. In the upper part of the measurement region, the relation is negative since the variance of the vertical velocity component is negative. The other turbulence energy transport models have somewhat larger relations, between $\overline{w'w'}$ and k , than the Reynolds stress transport models. There are some differences between the SKE-D and SST models compared to the SKE, SKE-A, and SKE-P models. The first two models have profiles with stronger curvature than the last three models which calculate relations closer to the isotropic assumption. As seen in Fig. 8.11, the first two models have larger gradients of the vertical velocity component which affect the strain rate term in the Boussinesq viscosity assumption, and thereby the calculations of the variance of the vertical velocity component.

9 Discussion

The validation and verification simulations demonstrated that basic test cases, despite their simple geometry and setup, can cause considerable difficulties for the tested turbulence models. Results from the fully developed channel flow indicated that the Reynolds stress transport models in STAR-CCM+ are of the prescribed types, but may differ from the author's original models [21, 61] in some aspects. This case also illustrated that the Boussinesq viscosity assumption is incapable of returning the correct normal stress anisotropy. The second test case, the backward-facing step, indicated challenges in simulating recirculation zones where wall functions may become invalid. The calculated reattachment lengths with the Reynolds stress transport models differed from other simulations, which may be related to mesh differences and invalid wall functions, as well as the formulation differences found in the fully developed channel flow. The surface-mounted cube case illustrated how turbulence models may perform poorly in cases with several recirculation zones and stagnation points. Numerical influence on simulation results, by means of discretization order and mesh resolution, was also illustrated with this test case. Stability issues were found for some models, which highlighted the importance of numerical robust turbulence models.

The issues found in the validation and verification cases may be part of the explanation for the discrepancies found between the simulations and experiments. Numerical errors, input uncertainty, and uncertainty in the experiments are other reasons. Input uncertainty is associated with discrepancies between the computational model of an experiment and the actual experiment [71, p. 289]. Assumptions are made for the inlet profiles in the simulations, and domains have been simplified. However, by attempting to use the same setup for all models, knowledge on general performance differences between the tested turbulence models may still be obtained.

The mean streamwise velocity component and the variance of the vertical velocity component have been evaluated at different locations in the validation and verification simulations. The streamwise velocity profiles are mostly consistent with experimental measurements, but the vertical Reynolds stress profiles are questionable. The Reynolds stress transport models do not outperform the simpler turbulence energy transport models in the present simulations. Their calculations of the vertical Reynolds stress component are often underestimated compared to the experimental measurements. Since the Reynolds stress transport models underes-

timate the vertical Reynolds stress component in some of the test cases, they may underestimate the vertical Reynolds stress component above the helideck. The calculated profiles for the vertical Reynolds stress component using the present Reynolds stress transport models, tend to be smaller in magnitude than with many of the turbulence energy transport models in the helideck simulations. Although this may be related to better maintained turbulence energy profiles, with smaller magnitudes than the turbulence energy transport models, as was illustrated in Figs. 8.1 and 8.2, the vertical Reynolds stress component may be underestimated with the Reynolds stress transport models in helideck simulations. If the vertical Reynolds stress component profiles are underestimated, simulations with these models may allow helidecks that should not be approved. The turbulence energy transport models, on the other hand, tend to overestimate the vertical Reynolds stress component in the validation and verification simulations, which is related to the incapability of returning the correct anisotropy. The strain rate term should be included when calculating the variance of the vertical velocity component with a turbulence energy transport model, since the vertical velocity component can vary significantly as a function of the height above the helideck, but the turbulence energy transport models are still likely to return larger relations between $\overline{w'w'}$ and k , than the Reynolds stress transport models.

Excessive production of turbulence energy in stagnation regions may be a problem in helideck simulations. Using a model that counteracts the stagnation point anomaly is therefore recommended. The RKE model, which uses a variable C_μ formulation, may be suitable. The performance of this model was generally good in the validation and verification simulations, even though the model had some indications of the stagnation point anomaly. The CKE model is another alternative with a variable C_μ formulation, but this model is unrealizable and calculated negative values for the variance of the vertical velocity component, which is particularly unfortunate in helideck simulations since the NORSOK criteria are on the square root of this quantity. The proposal by Durbin [15], to put a limiter on the turbulence timescale, is a simple and effective alternative to a variable C_μ formulation. However, models with this constraint had convergence issues in the surface-mounted cube case. This may indicate that variable C_μ formulations are favorable, but final conclusions on stability should not be drawn based on this limited number of simulations.

Compared to the original formulations for the turbulence energy transport models in this thesis, the models in STAR-CCM+ contain additional source terms that counteract turbulence decay. These terms may explain why the turbulence energy profiles are maintained in the atmospheric boundary layer simulations. The actual implementations of these source terms are somewhat unclear and better documentation would have been favorable in order to evaluate their effect on the model behavior. Even though additional terms will influence the behavior of the turbulence models, this approach seems to be better than tuning of coefficients, which was tested with the SKE-A model. The turbulence energy profile downstream of the inlet was found to be more correct when the coefficients were tuned, but the

performance of the model was changed significantly. Since helideck simulations may contain obstacles that cause separation and recirculation of the flow, tuning of coefficients should be done with caution.

Only two of the tested turbulence models fulfill the “*differential*” requirement in Norsok Standard C-004 [44]. A Reynolds stress transport model must be used, but there are no words in Norsok Standard C-004 regarding which Reynolds stress transport model that is preferred for helideck simulations. The present simulations show noticeable differences between two different models for the pressure-strain term. The shape of the turbulence and velocity profiles are mostly consistent for the two models, but their magnitude are somewhat different. In all helideck simulations, the LPS model calculates smaller standard deviations of the vertical velocity component. This may be related to a smaller approach value, as was illustrated in Fig. 8.3, and a more correct redistribution between the normal Reynolds stress components. Since the turbulence criteria in Norsok Standard C-004 are on the vertical component only, the LPS model may be better suited as it maintains the vertical Reynolds stress better than the QPS model. However, some of the vertical Reynolds stress component plots from the validation and verification simulations indicated significant underestimations with the LPS model compared to experimental measurements. Underestimations with the QPS model are also found, and this model may have more stability issues, as found in the surface-mounted cube case.

The working hypothesis of this thesis was that Reynolds stress transport models provide more accurate and unambiguous results for the turbulence quantities in question, compared to simpler turbulence energy transport models. Despite their differences in redistribution, the results are more unambiguous with the two Reynolds stress transport models than the results with the seven turbulence energy transport models. However, the results are not found to be more accurate in the validation and verification simulations. Based on the present simulations, it seems unnecessary to require the use of a Reynolds stress transport model in helideck simulations of structure induced turbulence, since the criteria are on maximum allowed values for the standard deviation of the vertical velocity component, and turbulence energy transport models are likely to give conservative results. For cases of structure induced turbulence, use of a Reynolds stress transport model could be favorable to avoid violations of the criteria, but the requirement seems unlikely to be necessary from a safety perspective.

The helideck simulations are performed with the same wind speed of 10 m s^{-1} . It could be interesting to study the turbulence quantities for other wind speeds to see if the relative performance between the turbulence models is dependent on the wind speed. The 000° and 090° wind headings were therefore tested with a reference wind velocity of 25 m s^{-1} . All inlet profiles were changed according to the new wind velocity, and the roughness on the ocean surface was increased according to Eq. (7.11). Since the roughness was changed, the near wall cell height in the prism layer mesh above the ocean was slightly increased, consistent with the guidelines mentioned in Section 7.3. Simulations with a wind speed of 25 m s^{-1} were found

more difficult to converge, with stability problems for some models. The SST model was found to be among the more stable models and both Reynolds stress transport models needed the result from this model as initial conditions in order to converge. The end results, for all turbulence models, were found to be similar to scaling the 10 m s^{-1} cases with 2.5. Further work with these simulations were therefore dropped.

The present simulations illustrate some of the challenges with numerical simulations of turbulent flows. Despite using the same setup, domain, inlet conditions, mesh, and solvers, different turbulence models will produce different results. The fact that there are a double digit number of turbulence models to choose from in STAR-CCM+, proves that there is not one perfect model suitable for all flow phenomena. Add the countless number of modifications and tuning options available, and one will always find models that satisfy a given requirement, and models that do not. Specifying which type of models that should be used can therefore be understandable, but it seems strange that simulations performed by turbulence energy transport models, that are found to have larger safety margins, will not be accepted according to NORSOK Standard C-004. It is important to point out that the present simulations represent a minority of helideck simulations, and only structure induced turbulence is considered.

A reevaluation of the turbulence requirements in NORSOK Standard C-004 could be beneficial. Is it just the standard deviation of the vertical velocity component that is important to ensure safe flying conditions, or should turbulence in all directions be considered? As mentioned in the introduction of the thesis, an alternative could be to have criteria on the turbulence energy instead of the standard deviation of the vertical velocity component. The present simulations showed that the differences in predictions of turbulence energy between different models are smaller than the differences in predictions of the variance of the vertical velocity component. This comes as no surprise since the turbulence energy transport models need a constitutive relation to calculate the Reynolds stress components. However, between the two Reynolds stress transport models, the relative differences were smaller in k than in $\overline{w'w'}$. The reason is seemingly related to the challenges of modeling the redistribution between the Reynolds stress components, a problem that is minimized if the criteria are on half the sum of the normal components since the sum of the normal pressure-strain terms equals zero for constant density flows. Calculations of turbulence energy are therefore likely to give less differences between different models, and thereby increase confidence in the results. As mentioned in Section 2.3, the turbulence criteria were set on the standard deviation of the vertical velocity component because this quantity varied the least between different scenarios in wind tunnel tests. The turbulence energy was found to vary with the same magnitude, as was shown in Table 2.3. The same tendency is found in the present simulations, the differences in $\overline{w'w'}$ and k for different wind headings are of the same magnitude when comparing the results for the two Reynolds stress transport models. The average relation $\overline{w'w'} = 0.45k$ was found for the wind tunnel measurements in CAA Paper 2004/03 [66, App. T], and used to propose criteria

on the turbulence energy. This value seems to be a reasonable estimation in the present simulations as well, as illustrated in Fig. 8.13, but it would be favorable to validate this proposal with further measurements or simulations.

10 Conclusion

The present study suggests that the Reynolds stress transport model requirement in NORSOK Standard C-004 is unnecessary for modeling of structure induced turbulence above helidecks, since the simulation results with turbulence energy transport models are found to be more conservative. Even though simulations with Reynolds stress transport models can provide more accurate and unambiguous results in some cases, these models seem more likely to underestimate the actual turbulence, compared to turbulence energy transport models.

The turbulence criteria in NORSOK Standard C-004 could be based on the turbulence energy instead of the standard deviation of the vertical velocity component, which would include turbulence in all directions. Calculations of the turbulence energy are less sensitive to the modeling of redistribution in Reynolds stress transport models and the constitutive relation in turbulence energy transport models. In the present simulations, the turbulence models are found to differ more in calculations of the variance of the vertical velocity component, than in calculations of the turbulence energy. Furthermore, turbulence energy based criteria seem to be consistent with the origin of the present criteria, with variations of the same magnitude as the variance of the vertical velocity component in the experimental measurements reported in CAA Paper 2004/03.

Excessive production of turbulence in stagnation regions can be a problem in helideck simulations. The standard k - ε model may therefore be unsuited. Using a realizable model with a constraint on the turbulence time- or lengthscale, or a variable C_μ formulation, is likely to provide more realistic results.

Adjusting coefficients in turbulence models for helideck simulations should be done with caution, as such adjustments may change the general model behavior significantly. The turbulence energy is not found to decay in the present simulations, which likely is due to additional source terms in the turbulence transport equations in STAR-CCM+. Using fixed values on the top boundary of the simulation domain may also maintain the turbulence energy better in atmospheric boundary layer simulations.

If the requirements in NORSOK Standard C-004 remain unchanged, the terms *differential turbulence model* and *vertical velocity fluctuations*, should at least be changed. The terms *Reynolds stress transport model* and *standard deviation of the vertical velocity component*, are less prone to misinterpretation.

References

- [1] Abe, H., Kawamura, H., and Matsuo, Y. Surface heat-flux fluctuations in a turbulent channel flow up to $Re_\tau = 1020$ with $Pr=0.025$ and 0.71 . *International Journal of Heat and Fluid Flow*, 25(3):404–419, 2004.
- [2] Ansys Fluent Theory Guide. Release 15.0, 2013.
- [3] Apsley, D., Chen, W., Leschziner, M., and Lien, F. Non-linear eddy-viscosity modelling of separated flows. *Journal of Hydraulic Research*, 35(6):723–748, 1997.
- [4] Basara, B. and Younis, B.A. Assessment of the SSG pressure-strain model in two-dimensional turbulent separated flows. *Applied Scientific Research*, 55(1): 39–61, 1995.
- [5] Blocken, B., Stathopoulos, T., and Carmeliet, J. CFD simulation of the atmospheric boundary layer: wall function problems. *Atmospheric Environment*, 41(2):238–252, 2007.
- [6] Britannica Academic Edition. North Sea. Primary contributor: Alexander, L.M. <http://www.britannica.com/EBchecked/topic/419398/North-Sea> Last visited 07.06.2014.
- [7] CD-adapco. User Guide STAR-CCM+ Version 8.06, 2013.
- [8] Charnock, H. Wind stress on a water surface. *Quarterly Journal of the Royal Meteorological Society*, 81(350):639–640, 1955.
- [9] Chen, C.J. *Fundamentals of Turbulence Modelling*. Taylor & Francis, 1997.
- [10] Cooper, G.E., Harper, R.P., Aeronautics, United States. National, and Administration, Space. The use of pilot rating in the evaluation of aircraft handling qualities. 1969.
- [11] Daly, B.J. and Harlow, F.H. Transport equations in turbulence. *Physics of Fluids*, 13(11):2634–2649, 1970.
- [12] Davidson, L. Fluid mechanics, turbulent flow and turbulence modeling, 2014. Lecture notes in the course MTF270 Turbulence Modeling at Chalmers University of Technology. Obtained 20.02.2014.

-
- [13] Driver, D.M. and Seegmiller, H.L. Features of a reattaching turbulent shear layer in divergent channel flow. *AIAA Journal*, 23:163–171, February 1985.
- [14] Durbin, P.A. Near-wall turbulence closure modeling without “damping functions”. *Theoretical and Computational Fluid Dynamics*, 3(1):1–13, 1991.
- [15] Durbin, P.A. On the k-3 stagnation point anomaly. *International Journal of Heat and Fluid Flow*, 17(1):89–90, 1996.
- [16] Duynkerke, P.G. Application of the E-epsilon turbulence closure model to the neutral and stable atmospheric boundary layer. *Journal of the Atmospheric Sciences*, 45(5):865–880, 1988.
- [17] Eirik Raude rig data and pictures. <http://www.offshore.no/Prosjekter/rigg-informasjon.aspx?navn=Eirik+Raude>. Obtained 25.02.2014.
- [18] Ertesvåg, I.S. *Turbulent strøyming og forbrenning : frå turbulensteori til ingeniørverktøy*. Tapir akademisk forlag, 2000.
- [19] Garratt, J.R. Review of drag coefficients over oceans and continents. *Monthly Weather Review*, 105:915, 1977.
- [20] Garratt, J.R. *The Atmospheric Boundary Layer*. Cambridge University Press, 1994.
- [21] Gibson, M.M. and Launder, B.E. Ground effects on pressure fluctuations in the atmospheric boundary layer. *Journal of Fluid Mechanics*, 86:491–511, June 1978.
- [22] Hadzic, I. *Second-moment closure modelling of transitional and unsteady turbulent flows*. PhD thesis, 1999.
- [23] Hanjalić, K. and Jakirlić, S. Contribution towards the second-moment closure modelling of separating turbulent flows. *Computers & Fluids*, 27(2):137–156, 1998.
- [24] Held, J., Revstedt, J., and Lörstedt, D. Turbulence – Theory and Modelling. <http://www.fm.energy.lth.se/fileadmin/fm/Fold13.pdf>, 2007. Information folder in the course Turbulence – Theory and Modelling. Obtained 28.01.2014.
- [25] Huser, A., Nilsen, P.J., and Skåtun, H. Application of k-epsilon model to the stable ABL: Pollution in complex terrain. *Journal of Wind Engineering and Industrial Aerodynamics*, 67-68:425–436, 1997.
- [26] James, M. and Scriven, J. and Green, R. and UK Civil Aviation Authority. CAA Paper 97009 – A Questionnaire Survey of Workload and Safety Hazards Associated with North Sea and Irish Sea Helicopter Operations, 1997.

- [27] Jones, W.P. and Launder, B.E. The prediction of laminarization with a two-equation model of turbulence. *International Journal of Heat and Mass Transfer*, 15(2):301–314, 1972.
- [28] Juretić, F. and Kozmar, H. Computational modeling of the neutrally stratified atmospheric boundary layer flow using the standard k–epsilon turbulence model. *Journal of Wind Engineering and Industrial Aerodynamics*, 115(0): 112–120, 2013.
- [29] Klein, T.S. The development of novel turbulence modelling approaches for complex industrial flows, 2008. 1st year PhD Report. School of Mechanical, Aerospace and Civil Engineering – The University of Manchester.
- [30] Lasher, W.C. and Taulbee, D.B. On the computation of turbulent backstep flow. *International Journal of Heat and Fluid Flow*, 13(1):30 – 40, 1992.
- [31] Launder, B.E. and Sharma, B.I. Application of the energy-dissipation model of turbulence to the calculation of flow near a spinning disc. *Letters in Heat and Mass Transfer*, 1(2):131–137, 1974.
- [32] Launder, B.E. and Spalding, D.B. The numerical computation of turbulent flows. *Computer Methods in Applied Mechanics and Engineering*, 3(2):269–289, 1974.
- [33] LeVeque, R.J. *Finite Difference Methods for Ordinary and Partial Differential Equations: Steady-State and Time-Dependent Problems*. Society for Industrial and Applied Mathematics, 2007.
- [34] Lien, F.S. and Leschziner, M.A. Assessment of turbulence-transport models including non-linear RNG eddy-viscosity formulation and second-moment closure for flow over a backward-facing step. *Computers & Fluids*, 23(8):983–1004, 1994.
- [35] Lien, F.S., Chen, W.L., and Leschziner, M.A. Low-reynolds-number eddy-viscosity modelling based on non-linear stress-strain/vorticity relations. In Rodi, W. and Bergeles, G., editors, *Engineering Turbulence Modelling and Experiments*, volume 3 of *Elsevier Series in Thermal and Fluid Sciences*, pages 91–100. Elsevier, Oxford, 1996.
- [36] Lien, K., Monty, J.P., Chong, M.S., and Ooi, A. The entrance length for fully developed turbulent channel flow. *15th Australasian Fluid Mechanics Conference, The University of Sydney, Australia*, 2004.
- [37] Makridis, A. and Chick, J. Validation of a CFD model of wind turbine wakes with terrain effects. *Journal of Wind Engineering and Industrial Aerodynamics*, 123, Part A(0):12–29, 2013.
- [38] Martinuzzi, R. and Tropea, C. Flow around surface-mounted, prismatic obstacles placed in a fully developed channel flow. *Journal of Fluids Engineering, Transactions of the ASME*, 115(1):85–92, 1993.

- [39] Medic, G. and Durbin, P.A. Toward improved prediction of heat transfer on turbine blades. *Journal of Turbomachinery*, 124(2):187–192, 2002.
- [40] Menter, F.R. Two-equation eddy-viscosity turbulence models for engineering applications. *AIAA journal*, 32(8):1598–1605, 1994.
- [41] Mentzoni, F. Turbulensmodellering av CO₂-spredning. Department of Energy and Process Engineering, Norwegian University of Science and Technology, December 2013.
- [42] Merci, B., Dick, E., Vierendeels, J., and Langhe, C.D. Determination of ε at inlet boundaries. *International Journal of Numerical Methods for Heat and Fluid Flow*, 12(1):65–80, 2002.
- [43] NORSOK Standard C-004: Helicopter deck on offshore installations, September 2004. Standards Norway. 1st Edition.
- [44] NORSOK Standard C-004: Helicopter deck on offshore installations, May 2013. Standards Norway. 2nd Edition.
- [45] NPARC Alliance Validation Archive. Details on the backward-facing step case. http://turbmodels.larc.nasa.gov/backstep_val.html and www.grc.nasa.gov/WWW/wind/valid/backstep/backstep01/backstep01.html. Obtained 15.05.2014.
- [46] Panofsky, H.A. and Dutton, J.A. *Atmospheric turbulence: models and methods for engineering applications*. Wiley, 1984.
- [47] Parameswaran, S., Jayantha, S., and Chock, C.V. A performance comparison of the standard k- ε model and a differential reynolds stress model for a backward-facing step. *Numerical Heat Transfer, Part B: Fundamentals*, 33(3): 323–337, 1998.
- [48] Park, C.H. and Park, S.O. On the limiters of two-equation turbulence models. *International Journal of Computational Fluid Dynamics*, 19(1):79–86, 2005.
- [49] Piquet, J. *Turbulent Flows: Models and Physics*. Springer, 1999.
- [50] Pope, S.B. *Turbulent Flows*. Cambridge University Press, 2000.
- [51] Richards, P.J. and Hoxey, R.P. Appropriate boundary conditions for computational wind engineering models using the k- ε turbulence model. *Journal of Wind Engineering and Industrial Aerodynamics*, 46–47(0):145–153, 1993. Proceedings of the 1st International on Computational Wind Engineering.
- [52] Richards, P.J. and Norris, S.E. Appropriate boundary conditions for computational wind engineering models revisited. *Journal of Wind Engineering and Industrial Aerodynamics*, 99(4):257–266, 2011. The Fifth International Symposium on Computational Wind Engineering.

-
- [53] Roache, P.J. Quantification of uncertainty in computational fluid dynamics. *Annual Review of Fluid Mechanics*, 29(1):123–160, 1997.
- [54] Rodi, W. Comparison of LES and RANS calculations of the flow around bluff bodies. *Journal of Wind Engineering and Industrial Aerodynamics*, 69–71(0): 55–75, 1997. Proceedings of the 3rd International Colloquium on Bluff Body Aerodynamics and Applications.
- [55] Schlatter, P. and Örlü, R. Assessment of direct numerical simulation data of turbulent boundary layers. *Journal of Fluid Mechanics*, 659:116–126, 9 2010.
- [56] Sekundov, A.N. On the boundary conditions for differential turbulence models. *Fluid Dynamics*, 47(1):20–25, 2012.
- [57] Shih, T.H., Liou, W.W., Shabbir, A., Yang, Z., and Zhu, J. *A New K-epsilon Eddy Viscosity Model for High Reynolds Number Turbulent Flows: Model Development and Validation*. 1994.
- [58] Sikorsky S-92 Helicopter Attributes. <http://www.sikorsky.com/Products>. Obtained 20.02.2014.
- [59] Silva, D.F.D.C.E., Pagot, P.R., Nader, G., and Jabardo, P.J.S. CFD simulation and wind tunnel investigation of a FPSO offshore helideck turbulent flow. *Proceedings of the International Conference on Offshore Mechanics and Arctic Engineering - OMAE*, 6:771–781, 2010.
- [60] Spalart, P.R. and Rumsey, C.L. Effective Inflow Conditions for Turbulence Models in Aerodynamic Calculations. *AIAA Journal*, 45:2544–2553, October 2007.
- [61] Speziale, C.G., Sarkar, S., and Gatski, T.B. Modelling the pressure-strain correlation of turbulence – An invariant dynamical systems approach. *Journal of Fluid Mechanics*, 227:245–272, June 1991.
- [62] Stull, R.B. *An Introduction to Boundary Layer Meteorology*. Atmospheric and Oceanographic Sciences Library. Springer Netherlands, 1988.
- [63] Surface-mounted cube experimental data. Case 6.3 for the 6th ERCOFTAC/IAHR/COST Workshop on Refined Flow Modelling. http://www.ercoftac.org/fileadmin/user_upload/bigfiles/sig15/database/6.3/ Obtained 24.03.2014.
- [64] UK Air Accidents Investigation Branch. AAIB Bulletin No. 3/96: Heavy Landing on Claymore Accommodation Platform, 1996.
- [65] UK Civil Aviation Authority. CAA Paper 99004 – Research on Offshore Helideck Environmental Issues, 2000.
- [66] UK Civil Aviation Authority. CAA Paper 2004/03 – Helicopter Turbulence Criteria for Operations to Offshore Platforms, 2004.

-
- [67] UK Civil Aviation Authority. CAP 437 – Offshore Helicopter Landing Areas: Guidance on Standards, 2005. 5th Edition.
 - [68] UK Civil Aviation Authority. CAP 437 – Offshore Helicopter Landing Areas: Guidance on Standards, 2008. 6th Edition.
 - [69] UK Civil Aviation Authority. CAA Paper 2008/02 – Offshore Helideck Environmental Research, 2009.
 - [70] UK Civil Aviation Authority. CAP 437 – Standards for Offshore Helicopter Landing Areas, 2013. 7th Edition.
 - [71] Versteeg, H.K. and Malalasekera, W. *An Introduction to Computational Fluid Dynamics - The Finite Volume Method*. Pearson Education Limited, 2. edition, 2007.
 - [72] White, F.M. *Fluid Mechanics*. McGraw-Hill Higher Education, 6th edition, 2008.
 - [73] Wilcox, D.C. *Turbulence Modeling for CFD*. DCW Industries, Incorporated, 1994.

A Backward-facing step figures

Additional figures for the backward-facing step case are given in this appendix. The figures contain plots of the mean streamwise velocity component and the variance of the vertical velocity component evaluated at different lengths downstream of the step. The first two figures show the profiles close to reattachment, at $x = 4H$ in Fig. A.1 and at $x = 8H$ in Fig. A.2. The last two figures, Figs. A.3 and A.4, show how the profiles have developed further downstream of the step, at $x = 12H$ and $x = 16H$, respectively. Details on this case are given in Section 6.2.

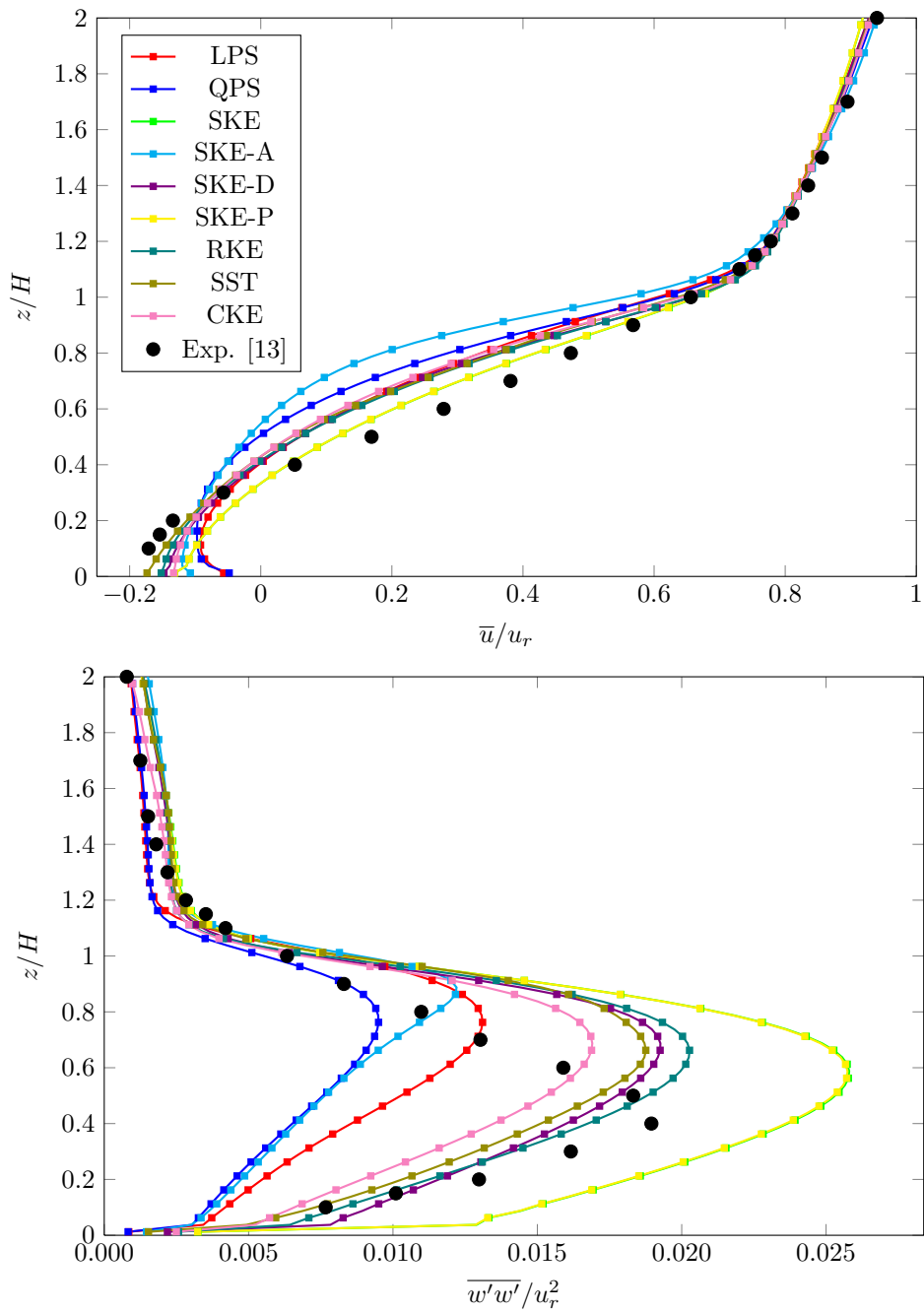


Figure A.1: Dimensionless mean streamwise velocity component and variance of vertical velocity component at $x = 4H$.

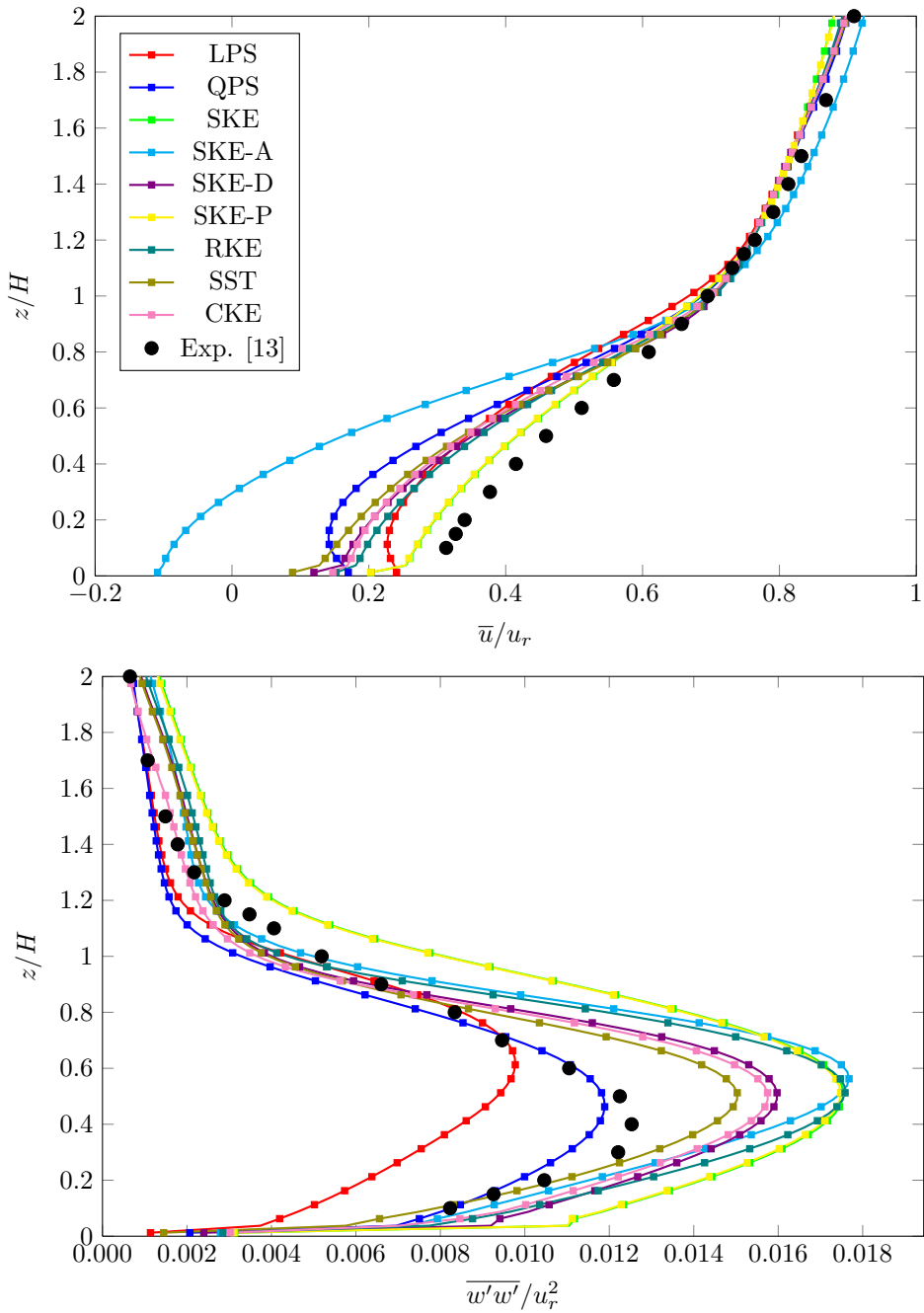


Figure A.2: Dimensionless mean streamwise velocity component and variance of vertical velocity component at $x = 8H$.

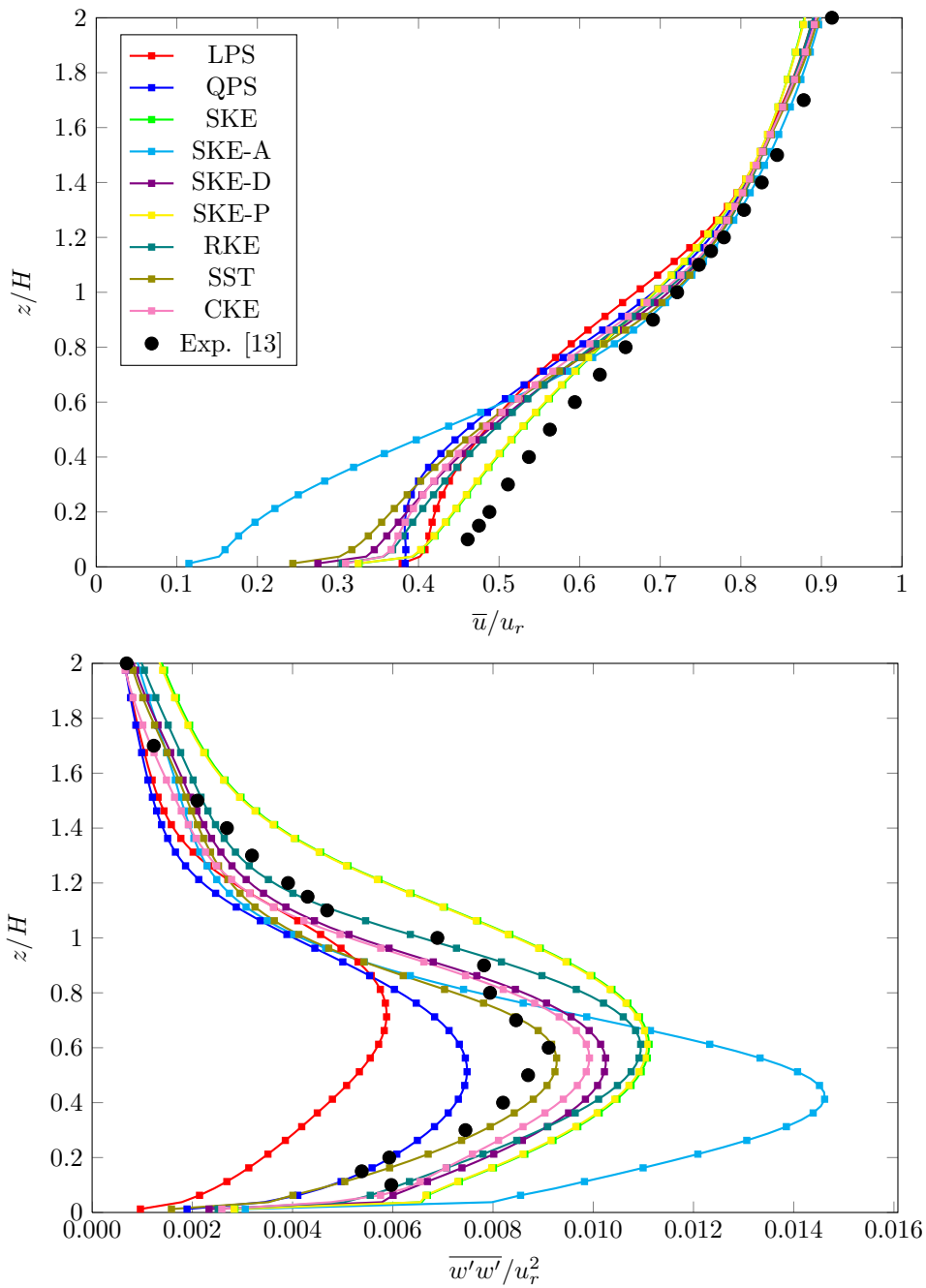


Figure A.3: Dimensionless mean streamwise velocity component and variance of vertical velocity component at $x = 12H$.

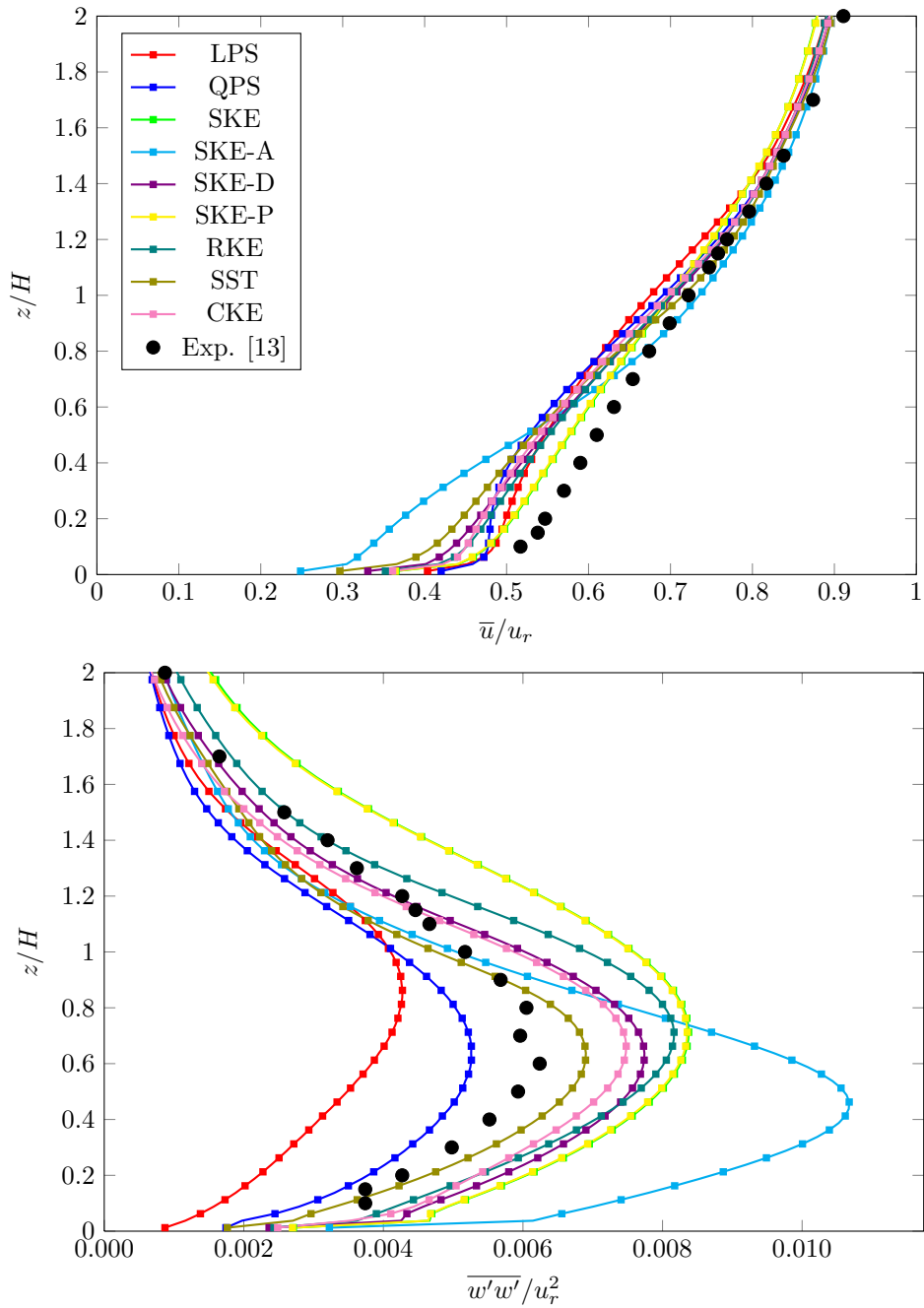


Figure A.4: Dimensionless mean streamwise velocity component and variance of vertical velocity component at $x = 16H$.

B Surface-mounted cube figures

Additional figures for the surface-mounted cube case are given in this appendix. The mean streamwise velocity component and variance of the vertical velocity component profiles one cube length downstream of the cube are presented in Fig. B.1, while the profiles three cube lengths downstream of the cube are given in Fig. B.2. Details on this case are given in Section 6.3.

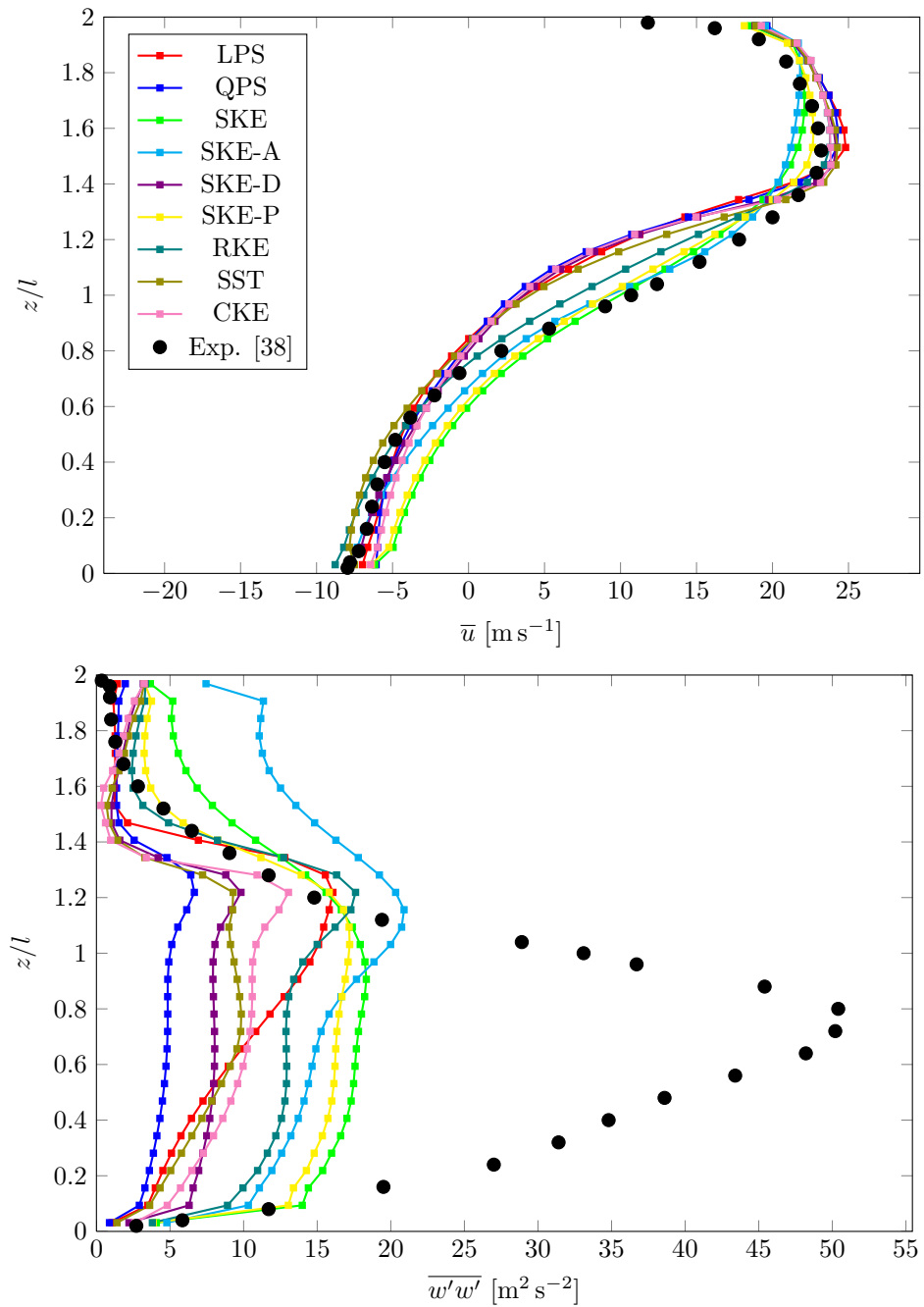


Figure B.1: Mean streamwise velocity component and variance of vertical velocity component at $x = 2l$.

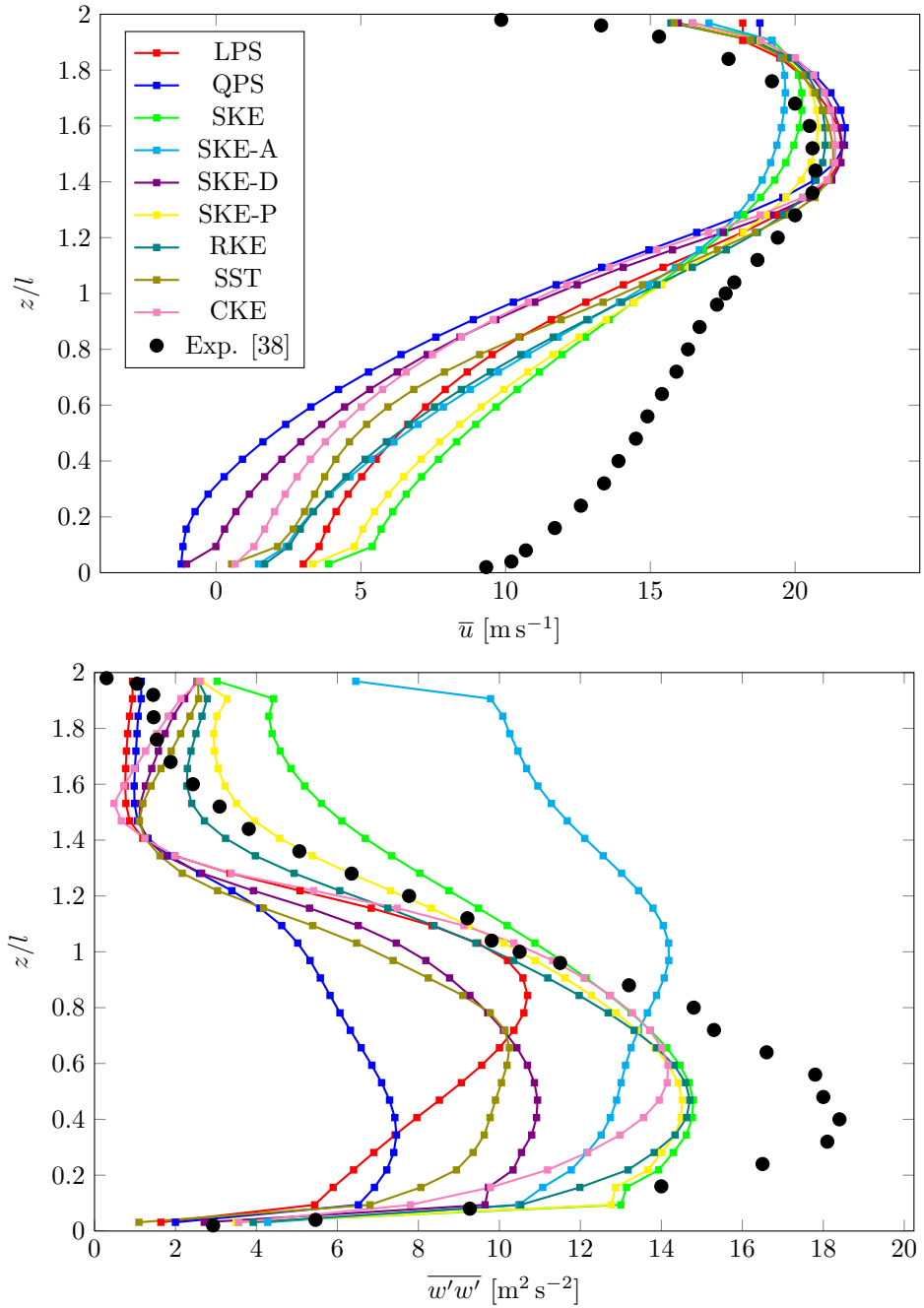


Figure B.2: Mean streamwise velocity component and variance of vertical velocity component at $x = 4l$.

